

**Construction of a Velocity Map Imaging Apparatus and its
Application to a Study of Photoionization Processes of C₆₀**

**Md. Serajul Islam Prodhan
Doctor of Philosophy**

**Department of Structural Molecular Science
School of Physical Science
The Graduate University for Advanced Studies
(SOKENDAI)
2008**

Acknowledgements

All of the studies of my Ph. D. course were carried out under the discerning supervision of Professor Koichiro Mitsuke. I would like to articulate my deepest and sincere gratitude to him for his keen sighted guidance and encouragement throughout the present study. I am too much grateful to him for giving me opportunity to being his group member and kindness in daily life supports.

I would like to thank Dr. Hideki. Katayanagi to teach me programs as well as our group research contents whenever with long duration I needed. He really understood me and grew my great interests to get a best appetite in C/C++ and Python script languages with correlating our group research works.

I would like to express my earnest thanks to all members of Mitsuke group, Prof. Koichi Nakajima, Dr. Hajime Yagi, Dr. Chaoqun Huang, Dr. Bhim Prasad Kafle for their useful discussion and recurrent helps in my needs.

I am very much grateful to all referee professors who corrected my thesis paper as well as put their best comments to modify it.

I would like to thank Professor Tsuneo Urisu to encourage me in study.

I am thankful to Mr. Toshifumi Asono of Urisu group for his extended helps in filling up scholarship and tuition fee applications on my studies and living in Okazaki, and also to other members in this group for their helps.

I thank Professor Hiroshi Kohguchi in Hiroshima University for providing the program code to perform the IAT and Prof. Toshinori Suzuki in Riken and Kyoto University for fruitful discussion on the VMI technique.

I also thank the members of the UVSOR for their help during the course of the experiments.

I am also thankful to Ms. Shimizu, secretary, Ms. Kyoko Kamo, secretary of the Foreign Affairs of IMS and all the staffs of Sokendai students' desk for their comprehensive helps.

Lastly, I thank my wife Nessa Ashrafun and son Aumio Fardun Islam for their silent contribution in my study.

“Table of Contents”

Title of the thesis.....	i
Acknowledgements.....	ii
Contents.....	iii
List of abbreviations.....	vi
Abstract.....	vii
Chapter 1	Preface
1.1 General Introduction	1
1.2 Study of process with VMI technique.....	6
References.....	10
Chapter 2	Experimental Method
2.0 Overview	13
2.1 Synchrotron Radiation and Monochromator.....	13
2.2 Experimental chamber and vacuum system.....	17
2.3 Velocity map imaging spectrometer and data acquisition system.....	17
References.....	19
Chapter 3	Experiments for VMI Images of Rare Gases
3.0 To test the fundamental performance of our VMI spectrometer	25
3.1 Introduction.....	25
3.2 Image data analysis.....	27
3.3 Simulated image of He ions.....	28
3.4 To check velocity focusing condition of VMI spectrometer using He sample.....	29
3.5 Defocusing parameters.....	30
3.6 Speed distribution of rare gases.....	33

3.7 Temperature table by using rare gas image.....	34
3.8 Conclusions.....	35
References.....	36

Chapter 4 Simulation for VMI images of C_{56}^+

4.0 Simulating the photoion images of C_{56}^+ fragment ions from C_{60}	49
4.1 Introduction.....	49
4.2 Assumptions in the scattering distribution program of C_{60}	50
4.3 Simulated image of C_{56}^+ from C_{60}	51
4.4 To verify $v_{CM}(C_{58}^+)$ and $v_{CM}(C_{56}^+)$ at different KER in C_{2-} and C_{4-} -loss processes.....	54
4.5 Wiener (Optimal) Filtering with FFT.....	56
4.6 Reconstructions of C_{56}^+ image by deconvolution methodology.....	59
4.7 Conclusions.....	61
References.....	62

Chapter 5 Summary and Future Prospects

Summary of the thesis.....	73
References.....	76
Future Prospect.....	77

Appendixes

Appendix-1	78
Metropolis-Hasting algorithm.....	78
Appendix-2	81
(a) Inverse Abel Transformation (IAT).....	81
References.....	85
(b) Basic concept of the IAT.....	86
Appendix-3	87
Maxwell-Boltzmann distribution function.....	87
Appendix-4	91

(i) Frequency domain filter in FFT calculations.....	91
(ii) Convolution Theorem.....	93
Appendix-5	94
(a) Developed program codes to simulate the images.....	94
(i) Rare gas image simulation.....	94
(ii) Photodissociation of fullerene, C ₆₀ with thermal parent beam.....	99
(b) Developed program tools to analyze experimental and simulated image...	106
List of Publications.....	113
List of Conference /Symposium /Workshop.....	115

List of abbreviation

Ultraviolet synchrotron orbital radiation, **UVSOR**

Synchrotron radiation, **SR**

Beamline **2B**, **BL2B**

Velocity map imaging, **VMI**

Time-of-flight, **TOF**

Microchannel plates, **MCPs**

Wiley-McLaren Time-of-flight, t_{WM}

Kinetic energy, **KE**

Kinetic energy release, **KER**

Point spread function, **PSF**

Standard deviations, σ_x , σ_y

Center-of-mass velocity, v_{CM}

Half widths at half maximum, **HWHM**

Full widths at half maximum, **FWHM**

Temperature in Kelvin, **K**

Photon energy, $h\nu$

Potential energy surface, **PES**

Position-sensitive detector, **PSD**

Two/three-dimensional, **2D/3D**

Inverse Abel transformation, **IAT**

The Fast Fourier Transformation, **FFT**

Electron volt, **eV**

Ultra-Violet, **UV**

Signal to noise ratio, **S/N**

Time to digital converter, **TDC**

Abstract of the Thesis

Two major topics of my thesis are (i) development of the velocity map imaging (VMI) spectrometer for investigation of the photoion images of fullerenes, and (ii) simulation studies of possible processes for C_{60} fragmentation. There are two plausible photofragmentation pathways of excited C_{60} cations, namely the stepwise C_2 -loss and direct fission processes. Several groups have tried to distinguish these two processes by measuring the total average kinetic energy release (KER) in the decomposition of C_{60}^+ into C_{56}^+ and smaller fragments. Such efforts, however, have met with failure. The portion of the KER partitioned to the ionic fragments was found to be a few tens of millielectronvolts, and is comparable to or smaller than the average thermal energies of neutral C_{60} molecules in an effusive beam. The above two processes therefore give C_{56}^+ and smaller fragments with similar average kinetic energies in the laboratory system. Obviously, we must measure a precise 3D velocity distribution, speed and angular distributions, to gain helpful clue to decide on which process is more dominant. For this purpose we have developed a VMI spectrometer that is very sensitive to thermal ions having small translational energies.

Our VMI spectrometer is based on a time-of-flight (TOF) technique for the fragment ions produced by irradiation of synchrotron radiation. Its basic performance has been experimentally tested by using rare gases at photon energy $h\nu = 35$ eV. The 3D velocity distributions were reconstructed by using the inverse Abel transformation (IAT) from the measured 2D images projected on a position-sensitive detector (PSD) to the cross-sectional images in the perpendicular plane of the spectrometer. Using the speed distributions extracted from these cross-sectional images, we have evaluated the temperatures by the

least-squares fit of the data points to the Maxwell-Boltzmann distribution. The best fitted curves of the lighter three rare gases are in reasonable agreements with the Maxwell-Boltzmann distributions at the temperature $T = 300$ K. The temperatures obtained by the fittings are 282, 272 and 295 K for He, Ne and Ar, respectively. Small deviations from the expected value of 300 K can be accounted for by systematic errors peculiar to the numerical image processing in the IAT. For Kr and Xe the agreement is much worse mainly due to smaller signal-to-background ratios. Furthermore, the best fitted curve of Xe appears to shift by 60 K in the direction of lower speed as compared to the expected distribution at 300 K. This shift can be explained as that the raw image of Xe includes not only Xe^+ but also Xe^{2+} signal counts.

We have simulated the images of five rare gases at 300 K to compare with the experimentally obtained images. From the simulated projections on the PSD we have obtained the cross-sectional images and speed distributions. The temperature of He is evaluated to be 287 K from the least-squares fit of the data points of the simulated speed distribution to the Maxwell-Boltzmann distribution. Similar simulations were executed for Ne and Ar. All the temperatures were found to be in good agreement with those from the experimental images. Moreover, a close inspection of the simulated images revealed that the defocusing effect due to a definite ionization volume can be well reproduced by introducing two Gaussian functions as (a) $2\sigma_x = 0.2$ and $2\sigma_y = 2.8$ mm when oven with thickness monitor was not installed inside the experimental vacuum chamber, (b) $2\sigma_x = 1.7$ and $2\sigma_y = 3.2$ mm when oven with thickness monitor was installed. Here, σ_x and σ_y corresponding to the standard deviations of two Gaussian functions which are called defocusing parameters.

A novel simulation method has been established for the image of the 3D velocity distributions of C_{56}^+ produced by dissociative photoionization of C_{60} .

We calculated the arrival positions of C_{56}^+ ions, the spatial density functions, and the projections on the PSD. The 2D cross-sectional images were derived from the projected images of C_{56}^+ ions produced through the stepwise C_2 - and C_4 -loss processes. At $T = 0$ K a marked difference in the image pattern could be seen between the two processes but it is almost smeared out under bulk conditions of C_{60} at $T = 273$ K owing to the convolution of the thermal velocity of nascent parent C_{60}^+ ions. In contrast, a remarkable difference at $T = 0$ K were found to remain even at $T = 785$ K for the C_{56}^+ formation in the C_{60} beam, because the transverse velocity of the beam is extremely low. The difference in the image pattern between the two processes permits us to provide conclusive evidence on which mechanism dominates photofragmentation of C_{60} in the extreme UV region. We therefore consider that the present VMI spectrometer will be available for future studies of the excited-state dynamics of fullerene ions. Experimentally the image of C_{56}^+ might be contaminated by the background dark counts due to impurities such as water, air, and organic compounds. We have tried to remove the background counts from the measured 2D image by means of deconvolution using the low-pass and Wiener filters.

Chapter 1

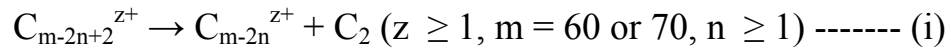
1.1 General Introduction

In 1985, Robert Curl and Richard Smally discovered fullerene, C_{60} , a third allotrope of carbon after diamond and graphite, in a high-pressure supersonic-nozzle beam produced with laser vaporization of graphite [1]. In C_{60} , 60 carbon atoms are arranged to form 20 hexagons and 12 pentagons. Later Krätschmer et al. [2] opened a new epoch in large-scale production of fullerenes in 1990 and various fullerenes have been synthesized and isolated thereafter. Fullerenes have spherical empty space inside the carbon cage. The hollow space is quite unique in that it is a nanometer-scale void and the volume can be varied with the size of fullerenes. It ranges, for example, from 0.4 to 1.0 nm in diameter on going from C_{60} to C_{240} [3]. Due to the sp^2 -hybridized bonding arrangement there are delocalized electrons around the fullerene sphere the number of which is equal to that of the carbon atoms. This draws great interests for their electrical and optical properties. Among various fullerenes C_{60} exhibits an exceptionally high stability against unimolecular decomposition, novel electronic properties, peculiar reactivity and useful catalytic behaviors. Many scientists in diverse fields have endeavored to elucidate the physical and chemical properties of fullerenes by means of traditional thermodynamic, diffraction, and spectroscopic methods [4,5]. There is a remarkable improvement in the performance of C_{60} thin-film field-effect transistors (TFTs) fabricated and characterized by molecular-beam deposition under a high vacuum [4,5]. Superconductivity has been discovered at high temperatures in the alkali-metal-doped fullerenes, K_3C_{60} (at critical temperature, $T_c = 19$ K [5-7]) and Rb_3C_{60} [8]. Furthermore, there has been speculation on the possible chemical and industrial uses of C_{60} [1] and on

its importance in interstellar dust as well as in geological formations on Earth [2,3]. Recently many authors have tried to make solar cells based on C₆₀ and its derivative [9-11].

As novel forms of fullerene-based material endohedral metallofullerenes (fullerenes with metal atom encapsulated) has already been synthesized successfully. These compounds are particularly interesting because the electron transfer from the encaged metal atom to the carbon cage is known to occur and this substantially alters electronic and magnetic properties of the fullerenes [3].

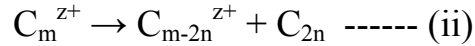
In the spectroscopic point of view, the fullerenes demonstrate unique photoabsorption and ionization properties. Moreover, a number of groups have obtained great insight into the single and multiple-photoionization processes and nature of dissociation of other clusters by observing the intrinsic behavior of photoionized fullerenes. Mass spectrometric studies of C₆₀ or C₇₀ show that appreciable fragmentation occurs when the system gains an internal energy more than ~ 50 eV in photoexcitation and photoionization processes [12-18]. The ion yield curves for fragments, C_{60-2n}^{z+} and C_{70-2n}^{z+} (n ≥ 1, z ≥ 1) produced from C₆₀ or C₇₀, respectively, have been reported in the extreme ultraviolet region [13-15]. Comparison between the experimental results and theoretical calculations revealed that the excess energy is statistically distributed among the internal degrees of freedom of the parent ions and sequential ejection of C₂ units (C₂ – loss process) as [19-23].



This conclusion was made on the basis of the findings that the experimentally observed ion yield curves and theoretically derived fractional abundance curves showed almost the same appearance energies for the formation of C_{m-2n}^{z+} (n = 1) [14,17]. The later curves were derived by employing the RRKM (Rice-Ramsperger-Kassel-Marcus) theory [24] to individual unimolecular reactions

steps. More reliable calculations of the rate constants of the consecutive reactions are sought before closer comparison between the two curves.

There are only a limited number of experimental studies of product analysis of the fragments. The translational energy distribution of C_{m-2n}^{z+} has been measured by several groups to understand the energetics and mechanisms of fragmentation. Hertel and co-workers [21] evaluated the kinetic energies of C_{m-2n}^{z+} ($1 \geq n \geq 14$) produced by photoionization of C_{60} , laser multiphoton ionization mass spectrometry of C_{60} . Later Märk and co-workers [22] performed electron-impact-ionization mass spectrometry of C_{60} in conjunction with the ion deflection method and reported a value of ca. 0.45 eV as the total average kinetic energy release (KER) in the decomposition of C_{60}^+ into C_{60-2n}^+ ($8 \geq n \geq 1$). These authors suggested that not only C_2 ejection of process (i) but also single-step two-fragment fission (C_{2n} -loss process) of the parent C_{60}^+ ions



could be a possible process for the formation of C_{60-2n}^{z+} . The mechanisms photofragmentation have been studied by measuring the average KER in the decomposition reaction of C_{60}^{z+} into C_{60-2n}^{z+} . The portion of the kinetic energy release partitioned to the fragments was found to be a few tens of meV, and is comparable to or smaller than the average thermal energies of neutral C_{60} molecules in an effusive beam. The above two processes therefore give C_{60-2n}^{z+} fragments with similar average kinetic energies in the laboratory frame. This situation should be also the case for other fullerenes, i.e. C_m^+ ($m = 70, 76, 78, 84$, and so forth). These unsolved problems inspired us to construct a velocity map imaging (VMI) spectrometer in order to study the ionic fragments produced from fullerenes. The conventional time-of-flight method contains KER information in the temporal structure at the arrival period of electrons or ions of a specific mass. On the contrary the ion imaging technique can extract a precise 3D velocity distribution, i.e. speed and angular distributions from the 2D

fragment image. These distributions provide us with a helpful clue to understand the decay processes of excited fullerene ions.

In order to exploit the imaging method to its full potential one needs to improve the quality of the 2D image. The mapping of 3D distributions of charged particles onto the 2D detector is particularly dependent on the configuration of the electrodes that extract ions by electrostatic field ion lenses. In 1987, Chandler and Houston developed the first VMI technique [25] for investigating the 3D velocity distributions of photoions and photoelectrons from small molecules. Later in 1997, Eppink and Parker drastically improved the resolution of the imaging spectrometer by replacing the conventional grid assembly with three-plate open-hole electrodes [26]. Their new ion lens system can lead the ions with the same velocity vector to the same spot on the surface of 2D position-sensitive detector (PSD), even if the ions are produced at different positions in the ionization volume. After this modification the VMI technique has marked a great advance and has become these days one of the most indispensable tools in the field of photochemistry and molecular reaction dynamics [27].

The imaging techniques have been used to measure the C_{60} fragments in different excitation schemes. Jensen et al. [28] studied the electron-transfer and collision-induced fragmentation processes of C_{60} in collision with slow highly-charged rare gas ions (i.e. 50 KeV Xe^{17+}). They measured the translational energy release distributions of the fragments ions from C_{60} by means of an imaging technique. In their experimental set-up a PSD was placed as a detector of a linear time-of-flight (TOF) mass spectrometer. In 2007 Climen et al. combined a time-resolved VMI technique with laser multiphoton ionization to estimate the KE release in fragmentation of C_{60} , though no image data was reported elucidating the 3D velocity distribution of fragment ions [29].

Katayanagi et al. [30] have constructed a VMI spectrometer based on a TOF technique to observe the momentum distributions of the scattered

fragments produced from dissociative photoionization of gaseous fullerenes using synchrotron radiation. The focusing condition can be satisfied by the three element lens system of Eppink-Parker type and high kinetic energy resolution can be achieved on the fragmentation images. We optimized the arrangement and dimensions of the three electrodes of the VMI lens system by ion trajectory simulations of C_{56}^+ , C_{58}^+ and C_{60}^+ produced from C_{60} to achieve high kinetic-energy resolution of ~ 10 meV [20].

The fundamental performance of this VMI spectrometer was experimentally investigated by using five rare gases (i.e. He, Ne, Ar, Kr, and Xe) in the photon energy of $h\nu = 35$ eV at 300 K. Eppink and Parker have optimized the voltages applied to their VMI lens system by adjusting the voltage to the extractor electrode with keeping the other voltages to the repeller and tube electrodes constant [26]. Following their way of adjusting we determined the optimum focusing conditions by examining the photoion images of rare gases.

In my Ph.D dissertation, I present the performance tests of our VMI spectrometer for achieving the high kinetic energy resolution of the photofragment images. Moreover, I describe a methodology and results on the simulation for the image of the 3D velocity distributions of C_{56}^+ to discuss the feasibility of the VMI experiments of C_{60} beams.

1.2 Study of process with VMI technique

Chemical reaction dynamics emerged as a separate branch of chemistry about 80 years ago with the derivation of the quantum mechanical expressions for the potential energy surface of chemical reactions. Since then, a huge number of experimental and theoretical works have been led to a better understanding of the quantitative nature of chemical reactions by using several modern spectroscopic techniques such as laser spectroscopy, photoabsorption spectroscopy, photoionization mass spectroscopy, and momentum imaging spectroscopy.

Potential energy curves for photodissociation of a hypothetical diatomic molecule AB into fragments A and B (internal state i , j , or k) shown in Figure 1.1 are excited via three different pathways a, b, and c. Such curves are constructed for each molecule using molecular quantum theory and models such as the Wigner-Witmer rules [31]. Due to spin-orbit coupling and other effects, curve crossing can take place leading to other dissociation products than those predicted by molecule – separated atom correlation diagrams. Using this diagram as a guide, we can make a ‘wish list’ of most important photodissociation properties we wish to quantify, as a function of excitation energy (wavelength):

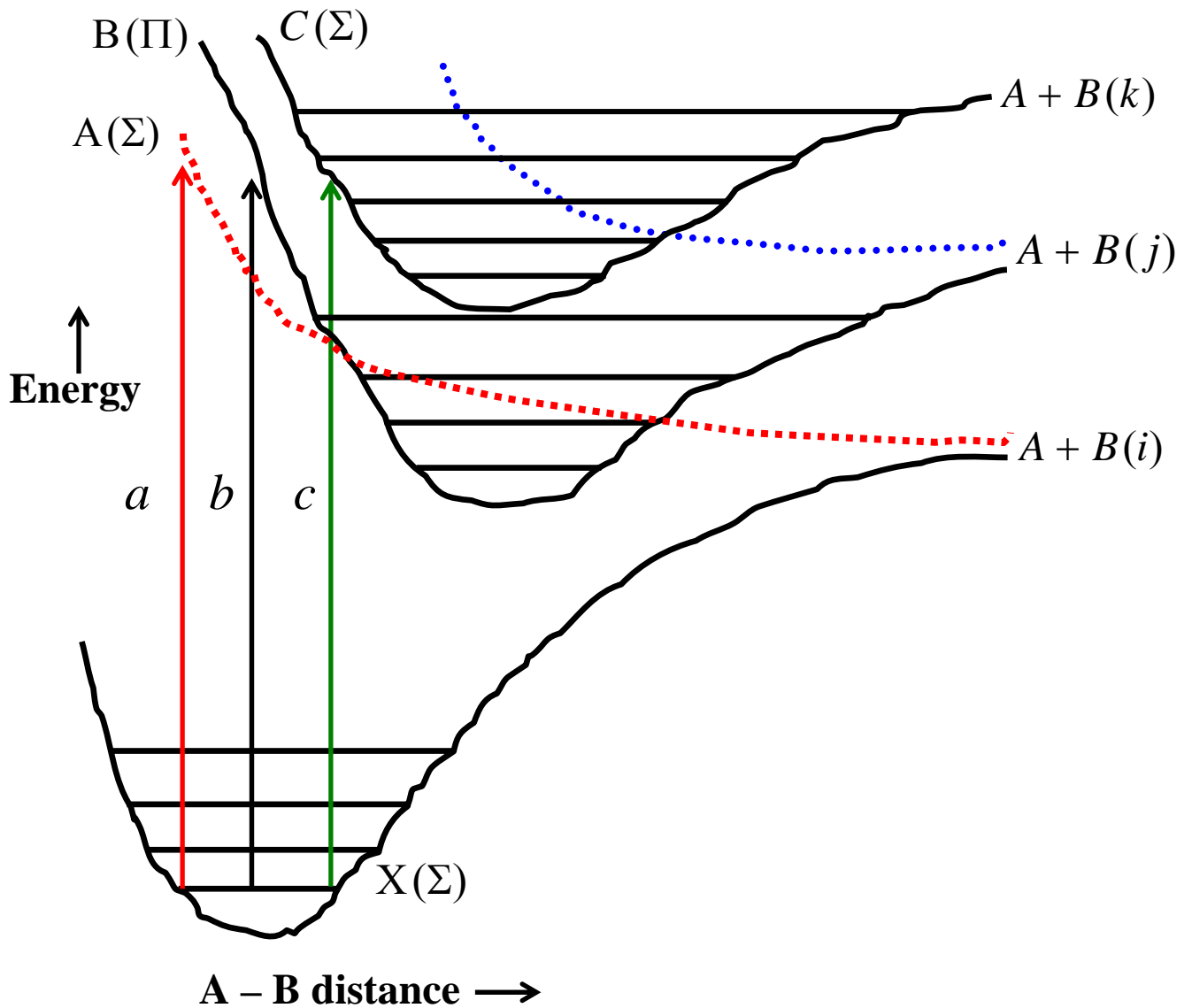


Figure 1.1 Hypothetical potential energy curves for different types of photodissociation pathways. (a) Direct excitation from a $X(\Sigma)$ ground state to the repulsive state $A(\Sigma)$ correlating to the first dissociation limit $A + B(i)$. (b) Excitation to the repulsive wall of state $B(\Pi)$, a bound state correlating with the second dissociation limit $A + B(j)$. Curve crossing to the first dissociation limit via the repulsive state excited in pathway (a) is possible. Excitation at an energy

exceeding the first and second dissociation limits to a bound state $C(\Sigma)$, correlating to $A + B(k)$. Pre-dissociation can take place by curve crossing via another repulsive state to the second limit as drawn in the figure.

- (i) D_0 , the A-B bond energy of X state, and of the B and C bound excited states such as those reached by pathways b and c.
- (ii) The symmetry ($\Sigma, \Pi, \Delta, \dots$) of ground and excited states.
- (iii) The absorption cross sections $\sigma_a, \sigma_b, \sigma_c$ for each transition.
- (iv) Time-scales for (pre-) dissociation of each quantum level of excited states.
- (v) Product yields to the first, second, and third dissociation channels.
- (vi) Angular distributions (beta parameter, β , and higher parameters) and possible vector correlations for each dissociation channel.
- (vii) Characterization of the importance of curve crossing over the photoexcited curve to curves leading to other dissociation products.
- (viii) Characterization of the importance of coherent (a + b + c) versus incoherent (a, b, or c) excitation of the different pathways.

Each of the above-listed properties is a research field in its own right. All provide important tests of molecular quantum mechanical theory, and many have practical applications, for example, in atmospheric chemistry.

All of the above information is extracted from product photofragment images in the form of radial, angular, and three-vector information. From the product KER and from energy balance the internal state distribution of both fragments can be determined. The surface pattern of the Newton sphere of photodissociation fragments is characterized via the beta (β) parameter and higher order alignment parameters as needed. From these two main quantities, KER and β , and from knowledge of the spectroscopy, quantum mechanics of

the parent molecule, and fragments we begin to fill in as much as possible of the above ‘wish list’.

Ion imaging is a rapidly advancing experimental technique full of possibilities in molecular dynamic research with presenting the full picture in living color. Studies of molecular reactions, energy transfer processes, and photodissociation events can be understood completely, only if the internal energies and velocities of all products can be determined. Thus far, the velocity map imaging research has had a great impact on the field of photodissociation dynamics of diatomic and small polyatomic molecules. Small molecules dissociate into multiple fragments with a limited number of internal energy states, leading to widely spaced and thus more resolvable Newton spheres.

Indeed, the photodissociation experiments in polyatomic molecules provide very detailed information on molecular interaction and bond-breaking dynamics [32]. After the invention of ion imaging technique in photo-dynamics the subsequent rapid expansion in the field has demonstrated the power of the VMI technique in studying the angular and kinetic energy distributions of photofragments [25,33]. Most often these ion imaging dissociation experiments have been done with nanosecond pulsed laser systems in which the total angular recoil distribution of a single rotational quantum state in a molecular fragment can be imaged rapidly by integration of only a few laser shots. Recently, we have succeeded to measure the speed and angular distributions of C_{60}^{z+} ($z = 1,2$) [31] produced from C_{60} molecular beams by utilizing our newly constructed VMI spectrometer with synchrotron radiation photoionization at 70 eV. Obviously, this was the first result of the velocity distributions of high symmetry fullerene cations.

References

- [1] H. W. Kroto, J. R. Heath, S. C. O'Brien, R. F. Curl, and R. E. Smalley, *Nature (London)* 318 (1985) 162
- [2] W. Krätschmer, Lowell D. Lamb, K. Fostiropoulos, and D. R. Huffman, *Nature* 347 (1990) 354.
- [3] H. Shinohara, *Rep. Prog. Phys.* 63 (2000) 843.
- [4] J. E. Fischer and P. A. Heiney, *J. Phys. Chem. Solids* 54 (1993) 1725.
- [5] R. C. Haddon et al., *Nature* 350 (1991) 320.
- [6] A. F. Hebrad, M. J. Rosseinsky, R. C. Haddon, D. W. Murphy, S. H. Glarum, T. T. M. Palstra, A. P. Ramirez, and A. R. Kortan, *Nature (London)* 350 (1991) 600.
- [7] K. Tanigaki, T. W. Ebbesen, S. Saito, J. Mizuki, J. S. Tsai, Y. Kubo, and S. Kuroshima, *Nature (London)* 352 (1991) 222.
- [8] K. Holczer, O. Klein, S-M. Huang, R. B. Kaner, K-J. Fu, R. L. Whetten, and F. Diederich, *Science* 252 (1991) 1154.
- [9] E. A. Katz, D. Faiman, S. M. Tuladhar, J. M. Kroon, M. M. Wienk, T. Fromherz, F. Padinger, C. J. Brabec, and N. S. Sariciftci, *J. Appl. Phys.* 90 (2001) 5344.
- [10] N. S. Sariciftci, L. Smilowitz, A. J. Heeger, and F. Wudl, *Science* 258 (1992) 1474.
- [11] C. J. Brabec, N. S. Sariciftci, and J. C. Humelen, *Adv. Funct. mater* 11 (2001) 15.
- [12] R. Wörgötter, B. Dünser, P. Scheier, T. D. Märk, M. Foltin, C.E. Klots, J. Laskin and C. Lifshitz, *J. Chem. Phys.* 104 (1996) 1225.
- [13] A. Reinköster, S. Korica, G. Prümper, J. Viefhaus, K. Godehusen, O. Schwarzkopf, M. Mast and U. Becker, *J. Phys. B At. Mol. Opt. Phys.* 37 (2004) 2135-2144.

- [14] K. Mitsuke, H. Katayanagi, J. Kou, T. Mori, and Y. Kubozono, in *Ionization, Correlation, and Polarization in Atomic Collisions*, CP811, edited by A. Lahman-Bennani and B. Lohmann, American Institute of Physics, New York (2006) 161-166.
- [15] J. Laskin, B. Hadas, T. D. Märk, and C. Lifshitz, *Int. J. Mass spectrom.* 177 (1998) L9-L13.
- [16] J. Kou, T. Mori, and Y. Kubozono and K. Mitsuke, *J. Electron. Spectrosc. Relat. Phenom.* 144 (2005) 247-250.
- [17] J. Kou, T. Mori, and Y. Kubozono and K. Mitsuke, *Phys. Chem. Chem. Phys.* 7 (2005) 119-123.
- [18] P. N. Juranic, D. Lukic, K. Barger and R. Wehlitz, *Phys. Rev. A* 73 (2006).
- [19] J. Kou, T. Mori, S. V. K. Kumar, Y. Haruyama, Y. Kubozono and K. Mitsuke, *J. Chem. Phys.* 120 (2004) 6005.
- [20] B. P. Kafle, H. Katayanagi, and K. Mitsuke, in *Synchrotron Radiation Instrumentation*, CP879, edited by J. Y. Choi and S. Rah, American Institute of Physics, New York, 2007, 1809-1812.
- [21] H. Gaber. R. Hiss, H. G. Busmann, and I. V. Hertel, *Z. Phys. D – Atoms, Molecules and Clusters* 24 (1992) 307-309.
- [22] D. Muigg, G. Denifl, P. Scheier, K. Becker, and T. D. Märk, *J. Chem. Phys.* 108 (1998) 963-970.
- [23] K. Gluch, S. Matt-Leubner, O. Echt, B. Concina, P. Scheier, and T.D Märk, *J. Chem. Phys.* 121 (2004) 2137.
- [24] R. A. Marcus and O. K. Rice, *J. Phys. Colloid Chem.* 55 (1951) 894
- [25] D. W. Chandler and P. L. Houston, *J. Chem. Phys.* 87 (1987) 1445-1447.
- [26] A. T. J. B. Eppink and D. H. Parker, *Rev. Sci. Instrum.* 68 (1997) 3477-3448.
- [27] T. Suzuki and B. Whitaker, in B. Whitaker (Ed.), *Imaging in Molecular Dynamics: Technology and Applications*. Cambridge University Press, Cambridge, 2003, p.165-186.

- [28] J. Jensen, H. Zettergren, A. Fardi, H. T. Schmidt, and H. Cederquist, Nucl. Instrum. Methods Phys. Res., Sect. B 205, 643 (2003).
- [29] B. Climen, B. Concina, M.A. Lebeault, F. Lepine, B. Baguenard, C. Bordas, Chem. Phys. Lett. 437 (2007) 17.
- [30] Hideki Katayanagi, Chaoqun Huang, Hajime Yagi, Bhim. P. Kafle, Md. Serajul I. Prodhan, Koichi Nakajima and Koichiro Mitsuke, Rev. Sci. Instrum. (2008) submitted.
- [31] G. Herzberg, Molecular Spectra and Molecular Structure I: Spectra of Diatomic molecules, (Krieger Publishing Company, Florida, 1989).
- [32] R. Schinke, Photodissociation Dynamics, Cambridge University Press, Cambridge, 1995.
- [33] D. W. Chandler and D. H. Parker Adv. Photochem. 25 (1999), 56

Chapter 2

Experimental Method

2.0 Overview

The description on the experimental arrangements used for the construction of a velocity map imaging apparatus and its application to a study of photoionization processes of C_{60} has been explained in this chapter.

All the experiments have been performed at the end station of beamline BL2B constructed in the UVSOR synchrotron radiation facility of the Institute for Molecular Science in Okazaki. The optical system consists of two pre-focusing mirrors, an entrance slit, an aperture, three spherical gratings (G1 – G3), two folding mirrors, a movable exit slit and a refocusing mirror was described in the literature [1, 2] and simply its schematic diagram is shown in Figure 2.1. All the data in the present study were measured using the grating G3 with groove density of $2400 \text{ lines mm}^{-1}$ which covers the $h\nu$ range 24 – 55 eV. A set of plane mirrors are inserted across the photon beam between the grating and exit slit. Thereby the second and higher order lights of the grating are significantly reduced and their contamination can be disregarded.

The details of our velocity map imaging spectrometer (VMI) were described elsewhere [3, 4], and we will briefly explain its design and experimental methods by using the schematic diagram in Figures 2.3a and 2.3b which are related to rare gas as well as C_{60} experiments, respectively.

2.1 Synchrotron Radiation and Monochromator

UVSOR (Ultraviolet Synchrotron Orbital Radiation) facility in IMS consists of a 15 MeV linear accelerator (liniac) as an electron beam pre-injector, a booster electron synchrotron (about 8.5 m diameter) for the accelerating the electron beams up to 750 MeV, and a 750 MeV electron storage ring for

producing synchrotron radiation [5]. The storage ring has a quasi-octagonal shape with combination of 8 bending magnets and 8 straight sections. In straight sections, four undulators are installed for producing higher brightness synchrotron radiation. Furthermore, a radio-frequency RF cavity is used to compensate the energy of the electron beam lost by emitting synchrotron radiation. When UVSOR is operated in its multi bunch mode, the electrons are stored with into 16 bunches. The main parameters of the UVSOR accelerator complex and beamline specifications are summarized in Tables 1 and 2.

Table 1
General parameters of the storage ring

Circumference	53.2 m
Energy	750 MeV
Injection energy	750 MeV
Number of bunches	Multi bunch Mode: 16 Single bunch Mode: 1
Maximum stored current	500 mA (multi bunch) 100 mA (single bunch)

Beam lifetime	Multi bunch Mode: 8h (at 200 mA) Single bunch Mode: 1h (50 mA)
Beam sizes	0.39 mm (horizontal) 0.27 mm (vertical)
Pulsed light period	Multi bunch Mode: 11 ns Single bunch Mode: 176 ns
Pulsed light width	~ 1 ns (min. 20 ps) with a harmonic cavity system
Vacuum pressure	~ 1×10^{-10} Torr

Table 2
Beamline (BL2B) specifications

Monochromator	18-m spherical grating Dragon-type
Wavelength range	6 – 55 nm; 24 – 205 eV
Resolution	2000 – 8000 depending on the gratings
Experiments	Mass spectrom.; Photoelectron spectrosc.; Momentum imaging spectrosc.; e ⁻ -Ion coincidence spectrosc.; Fullerene beam source

The Beamline BL2B in UVSOR has been utilized for the study of photoionization and reaction dynamics of various fullerenes in gas phase [6]. As shown in the schematic diagram of this beamline (side view) in Figure 2.1, synchrotron radiation emitted from the storage ring is focused onto the entrance slit by two pre-focusing mirrors. The incident SR (Synchrotron Radiation) was monochromatized by the Dragon type monochromator which covers the $h\nu$ range of 23 – 205 eV with three gratings: G1 (2400 lines mm^{-1} , $R = 18$ m) at 80 – 205 eV; G2 (1200 lines mm^{-1} , $R = 18$ m) at 40 – 100 eV; G3 (2400 lines mm^{-1} , $R = 9.25$ m) at 24 – 55 eV [1]. After passing through the movable exit slit, the monochromatized light is refocused into the ionization region by the post-focusing mirror (toroidal type). When the entrance and exit slit widths were set to 300 μm , the resolution (the full width at half maximum) which was determined by the measurement of the photon energy was estimated to be 8.5 meV of the members of the $3s^{-1} np$ Rydberg series of argon which lie at $h\nu = 25 - 30$ eV [2]. The details of the monochromator have been published elsewhere [1, 2].

The first-order light monochromatized by the grating G2 was subject to contamination of the second-order light. The $h\nu$ dependence of the percentage of the second-order light was estimated by measuring the ion yield spectrum of He at $h\nu = 40 - 100$ eV [6] (contamination of the third and fourth order lights were considered to be negligible and were not evaluated). The percentage was determined as an adjustable parameter to reduce the observed spectrum from the absorption cross section data of He [7]. For instance, the percentage of $h\nu = 40$ eV was found to be 22 %. Alternatively, the percentage of the second-order light could be calculated based on the Kr^+ yield spectra of Kr in the vicinity of the $3d_{5/2}5p^1$ resonance peaks appearing at 45.6 and 91.2 eV, with the aid of the reported partial photoionization cross section [8] of Kr at around 45 and nearly 90 eV. The resultant percentage was 23% at ~ 45 eV, which accords well with the value obtained using the ion yield spectrum of He.

2.2 Experimental chamber and vacuum system

The experimental chamber is evacuated by turbomolecular pump with its pumping speed of 1000 l/s. The typical background pressure is 5.0×10^{-8} Torr without a sample gas. Moreover, a differential pumping chamber has been set between the experimental chamber and the post-focusing mirror which is pumped by an ion pump and supported by two turbo molecular pumps of pumping speed of 340 l/s installed near the both ends of this chamber. When the sample gas is introduced, the background pressure of up to $\sim 1 \times 10^{-5}$ Torr is allowed in the experimental chamber with keeping the pressure in the post-focusing mirror chamber $\sim 1 \times 10^{-9}$ Torr. Typically, during the experiments the pressure of the chamber was kept to be 1×10^{-6} to $\sim 1 \times 10^{-7}$ Torr. To shield the photoionization region from the external magnetic field, the μ -metal shield is equipped inside the experimental chamber.

2.3 Velocity map imaging spectrometer and data acquisition system

The constructed velocity map imaging apparatus is shown in Figure 2.2. Figures 2.3a and 2.3b show the schematic illustrations of the VMI spectrometer based on a time-of-flight (TOF) technique for rare gas as well as C_{60} experiments, respectively. In these diagrams: a, repeller; b, extractor; c, drift tube entrance; d, ion drift tube; e, position-sensitive detector (PSD); f, fullerene sample cell; g, nozzle and orifices; h, crystal-oscillator surface thickness monitor. Rare gases of room temperature were introduced into the vacuum chamber through a tube with an inner diameter of 4.4 mm by controlling a middle valve. An ambient gas pressure was approximately 2.0×10^{-6} Torr. The ionization volume lies between the repeller and extractor electrodes and its center is located on the symmetry axis of the VMI lens. The monochromatized

synchrotron radiation with having the spot size of ~ 3 mm horizontal and ~ 1 mm vertical was continuously focused at the center of the intersection region to photoionize the rare gas atoms. The produced photoions of the ionization volume are then extracted by the VMI electrode assembly traveled through a drift tube. Their 3D scattering distributions were projected onto the surface of the PSD (Quantar Technology, 3390A) with a 256×256 spatial resolution composed of chevron-type dual microchannel plates (MCPs) of 25 mm in diameter. This PSD was placed at 375 mm away from the center of ionization volume. The position data were processed by a position computer (Quantar Technology, 2401B). The signal from PSD is also fed into a TDC (time to digital converter) to measure the TOF.

Moreover in photoionization experiments of gaseous C_{60} , the powder of pure C_{60} is loaded in a cylindrical quartz tube (Figure 2.3b) and further purified by eliminating the organic solvent such as benzene or toluene through heating the sample for one day (12 h) in a vacuum at nearly 200°C . In order to produce a molecular beam of C_{60} , sample holder is to be heated up at $700 - 800$ K with a resistive heater. The produced molecular beam was passed from a conical nozzle with a throat diameter of 1 to 2.5 mm and a divergence angle of 7.2° . The distance between the exit of the quartz tube and intersection region is about 43 mm. The water cooled thickness monitor, h (effective area, 53.5 mm^2 ; Inficon, XTM/2) placed about 35 mm away from the central point of the ionization region for the purpose of measuring the flux of the fullerene beam correctly. Photon monitor and picoammeter were used for counting the photoions per second and to measure the photon flux of the synchrotron radiation, respectively.

Eppink and Parker have optimized the voltages applied to their VMI lens system by adjusting the voltage V_E applied to the extractor electrode with keeping the other constant [9]. Following their way of adjusting we determined the optimum focusing conditions by examining the photoion images of rare gases. The voltages applied to the repeller, extractor and tube electrodes were

$V_R = 640$ V, $V_E = 353$ V and $V_T = -350$ V, respectively. The data acquisition time was set 60 s and the average ion count was $\sim 3.5 \times 10^4$ cps. More generally, optimum conditions were obtained when $(V_E - V_T) / (V_R - V_T) = 0.71$. There was no influence of the recoil velocity generated by photoelectron ejection on the speed distribution, because the photon energy used is relatively small ($h\nu = 25 - 50$ eV).

References

- [1] M. Ono, H. Yoshida, H. Hattori and K. Mitsuke, Nucl. Instrum. and Methods in Phys. Res. Sect.A 467, (2001) 577.
- [2] H. Yoshida and K. Mitsuke, J. Synchrotron Rad. 5, (1998) 774.
- [3] Bhim P. Kafle, Hideki Katayanagi, and Koichiro Mitsuke, in Synchrotron Radiation Instrumentation, CP879, edited by J. Y. Choi and S. Rah, American Institute of Physics, New York, 2007, 1809-1812.
- [4] Hideki Katayanagi, Chaoqun Huang, Hajime Yagi, Bhim P. Kafle, Md. Serajul I. Prodhan, Koichi Nakajima and Koichiro Mitsuke, Rev. Sci. Instrum. (2008) (Submitted)
- [5] UVSOR ACTIVITY REPORT (2007), Pg. 14 - 24
- [6] K. Mitsuke, H. Katayanagi, Bhim P. Kafle, C. Huang, H. Yagi, Md. Serajul I. Prodhan, and Y. Kubozono, J. Phys. Chem. A 111 (34), (2007) 8336.
- [7] J. M. Bijau and F. J. Wuilleumier, J. Electron Spectrosc. Relat. Phenom. 71 (1995) 205.
- [8] N. Saito and H. I. Suzuki, Int. J. Mass Spec. Ion Proc. 115 (1992) 157.
- [9] A. T. J. B. Eppink and D. H. Parker, Rev. Sci. Instrum. 68 (9), 3477 (1997).

Figures of Chapter Two

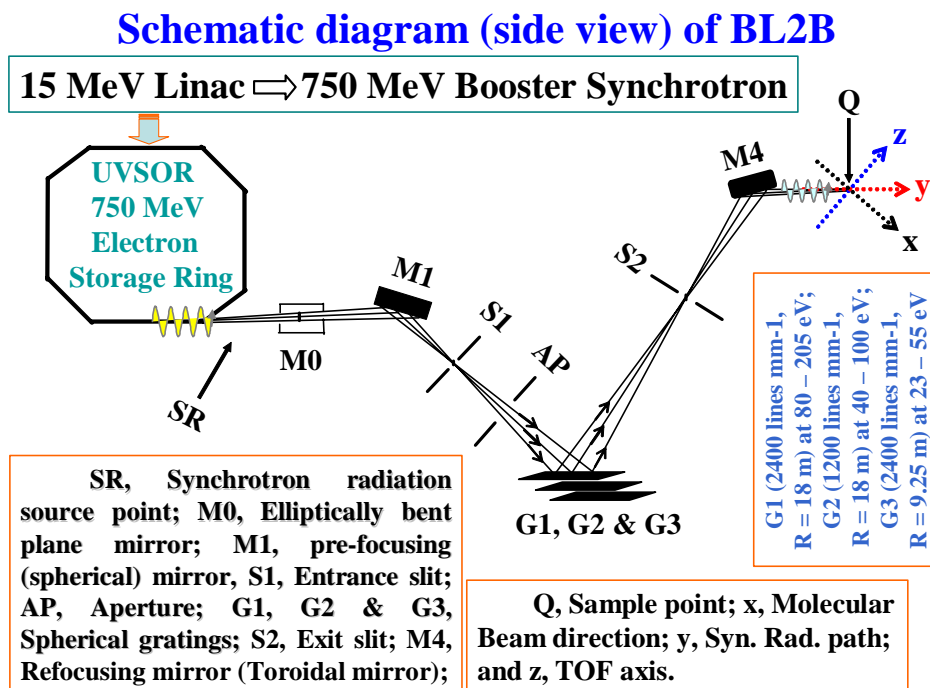


Figure 2.1

Schematic diagram (side view) of BL2B equipped with an 18 m spherical grating monochromator (SGM).

Constructed velocity map imaging (VMI) Apparatus

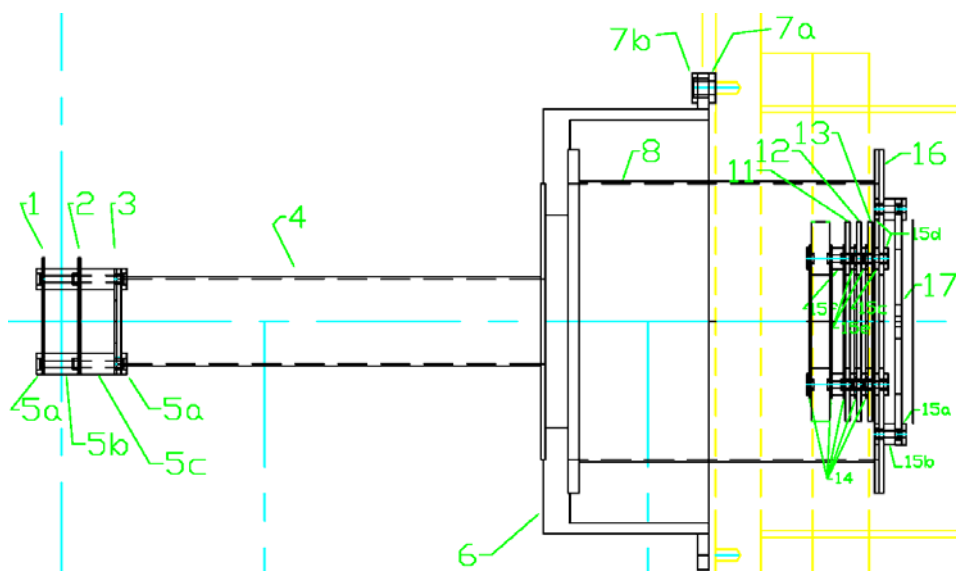


Figure 2.2

Main components: 1. Repeller electrode, 2. Extractor electrode, 3. Tube electrode, 4. Time-of-flight (TOF) tube, 15. Potential switch, 11 & 13. Grounded electrodes, 12. Retarding electrode and 17. PSD holder

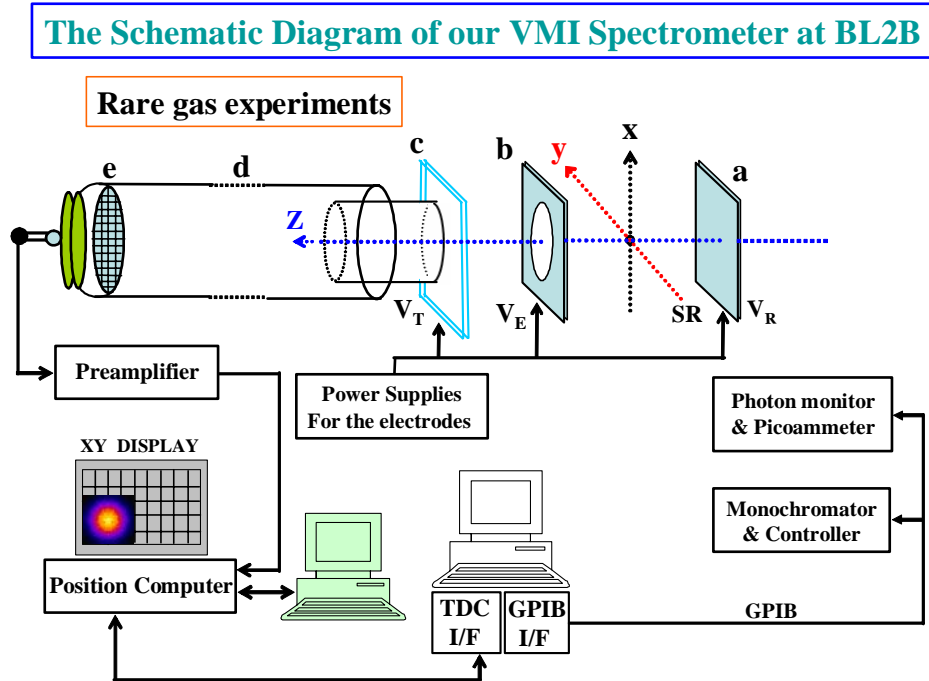


Figure 2.3a

Velocity map imaging setup for rare gas experiments.

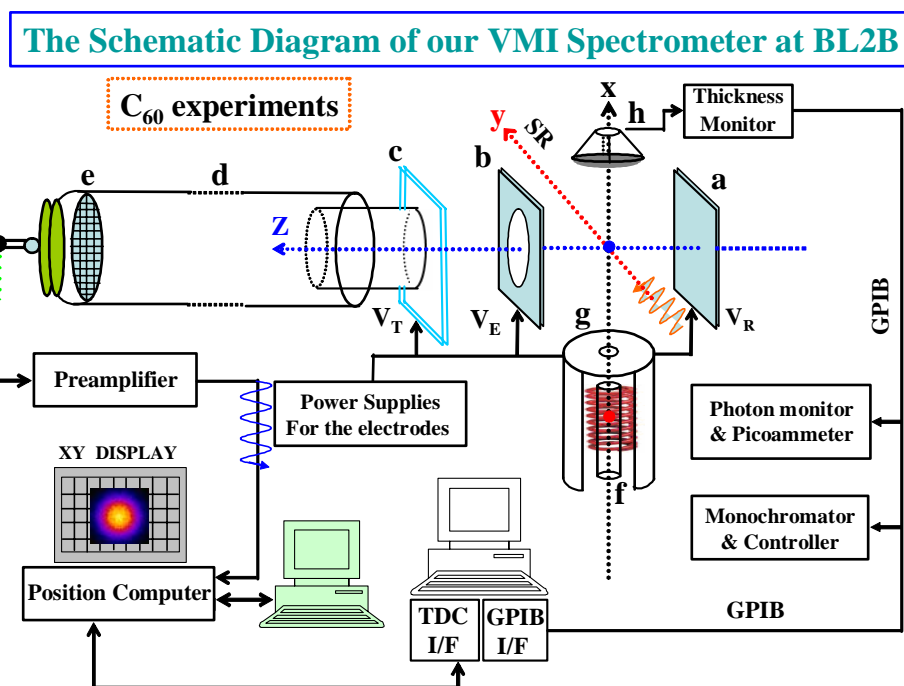


Figure 2.3b

Schematic illustration of the VMI spectrometer. (a), repeller; (b), extractor; (c), ion drift tube entrance; (d), ion drift tube; (e), position-sensitive detector (PSD); (f), fullerene sample cell; (g), nozzle and orifices; (h), crystal-oscillator surface thickness monitor.

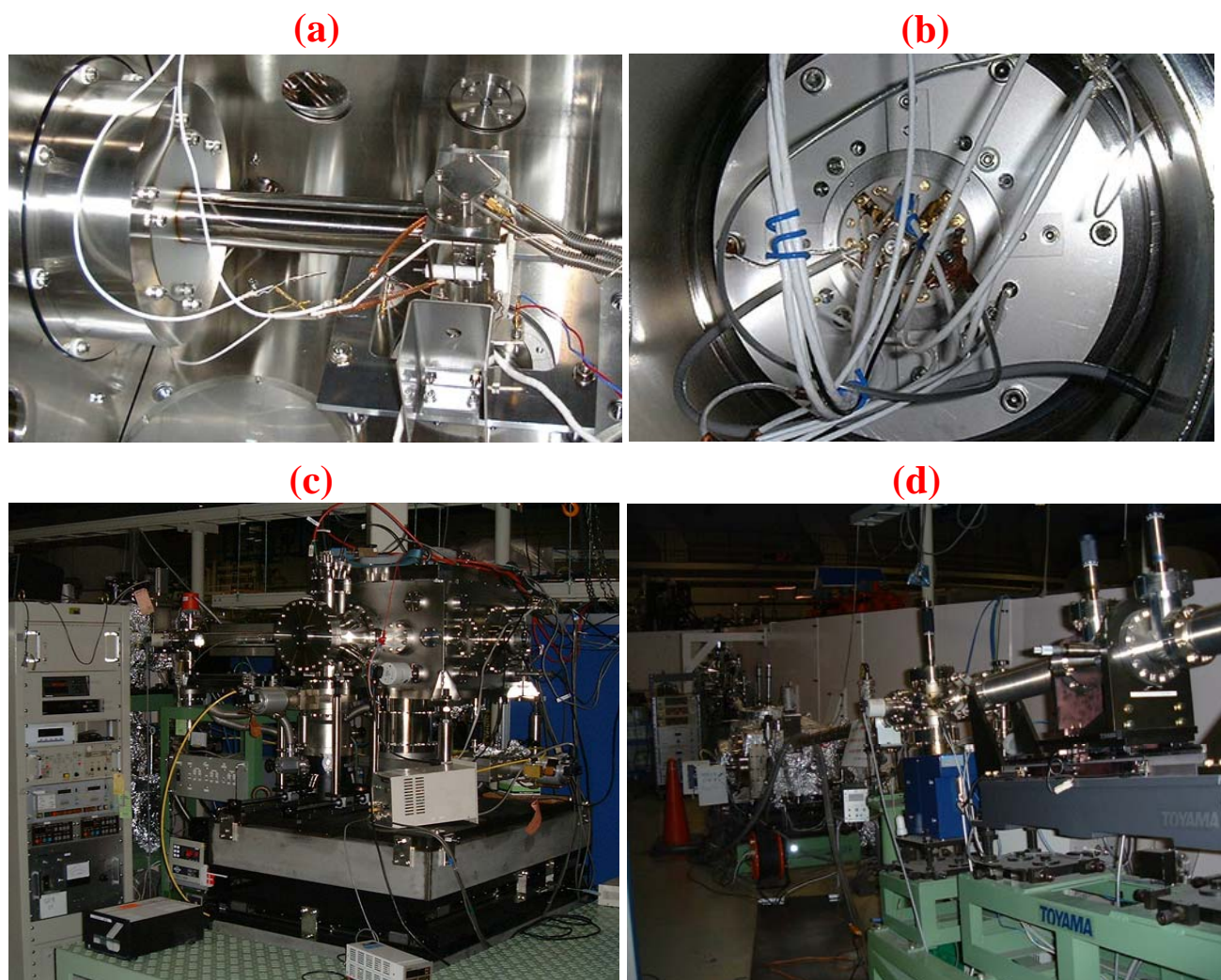


Figure 2.4

Photographs of our VMI spectrometer (TOF based), end station of BL2B and monochromator. (a) Inside view of the electrodes, ion drift tube, thickness monitor, and oven with other components, (b) Position of the PSD installed inside the experimental vacuum chamber. (c) Outside view of the end station of BL2B and (d) 18-m spherical grating monochromator.

Chapter 3

“Published in Chem. Phys. Letters, CPL 469 (2009) 19-25”

3.0 To test the fundamental performance of our VMI spectrometer

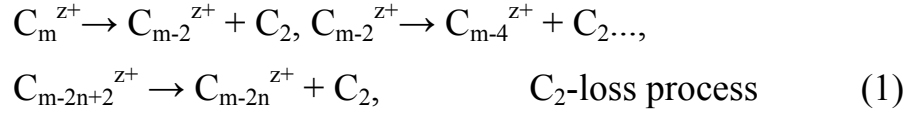
3.1 Introduction

The velocity map imaging (VMI) technique was first developed by Chandler and Houston [1] for investigating the three-dimensional (3D) velocity distributions of photoions and photoelectrons from small molecules. Eppink and Parker [2] have replaced the conventional electrostatic lenses having a meshed hole by a new lens system composed of three electrodes with an open hole to dramatically improve the resolution of images. Their lens system can guide the ions with the same velocity vector to the same spot on the surface of a 2D position-sensitive detector (PSD), even if the ions are produced at different positions in the ionization volume. After this modification the VMI technique has marked a great advance and has become these days one of the most indispensable tools in the field of photochemistry and molecular reaction dynamics [3].

We have recently constructed a VMI spectrometer based on a time-of-flight (TOF) technique to observe the momentum distributions of the scattered fragments produced from dissociative photoionization of gaseous fullerenes using synchrotron radiation [4,5]. It is well known from previous photon and electron impact experiments that appreciable fragmentation occurs when C_{60} or C_{70} gains an internal energy more than ~ 50 eV in excitation and ionization processes [6-12]. In 2007 Climen et al. combined a time-resolved VMI technique with laser multiphoton ionization to estimate the kinetic energy

release (KER) in fragmentation of C_{60} , though no image data was reported elucidating the 3D velocity distribution of fragment ions [13].

Decomposition of C_{60}^{z+} or C_{70}^{z+} ($z \geq 1$) primarily formed leads to fragment ions with even numbered carbon atoms, C_{60-2n}^{z+} and C_{70-2n}^{z+} . More generally various fullerenes C_m undergo similar fragmentation by way of C_m^{z+} [14]. Here, n designates the number of C_2 units lost. The size m of the fullerenes and higher fullerenes takes 60, 70, 76, 78, 84, and so forth. For the fragmentation with $n \geq 2$ two possible processes have been proposed [4,15,16]. One process is sequential ejection of C_2 units as



and the other is fission-like ejection of C_{2n} as



For instance, the formation of C_{56}^+ may proceed under either C_2 - or C_4 -loss process from C_{60}^+ ($z \geq 1$, $m = 60$ or 70 , $n \geq 2$). Several groups have tried to distinguish the two processes by measuring the average KER in the decomposition of C_{60} into C_{56}^+ and smaller fragments [14-16]. Such efforts, however, have met with failure. The portion of the KER partitioned to C_{60-2n}^{z+} fragments was found to be a few tens of meV, and is comparable to or smaller than the average thermal energies of neutral C_{60} molecules in an effusive beam. The two mechanisms therefore give C_{60-2n}^{z+} fragments with similar average kinetic energies in the laboratory frame. This situation should be also the case for other fullerenes i.e. C_m^{z+} ($m = 70, 76, 78, 84$, and so forth). It is needed to measure a precise 3D velocity distribution, i.e. speed and angular distributions, from which we can gain helpful clue to understand the decay mechanisms of excited fullerene ions. Thus there is an obvious need for a VMI spectrometer which is sensitive to thermal ions with small translational energies. In this chapter we will report the performance tests of our VMI spectrometer aimed to high kinetic-energy resolution on the photofragment images of fullerenes. To

check this performance we have selected five rare gases (i.e. He, Ne, Ar, Kr, and Xe) at room temperature because of their known velocity distributions.

3.2 Image data analysis

We defined a Cartesian coordinate system whose origin is located at the center of the ionization volume. Here, the synchrotron radiation path is assigned to the y axis, and the symmetry axis of the VMI lens and drift tube to the z axis. The x axis intersecting with the y and z axes at right angles accords with the molecular beam path when C_{60} is used as a sample. We can convert the image on the PSD to the cross-sectional image of the initial 3D velocity distribution in the x-y plane by using the inverse Abel transformation (IAT) [1,17,18]. In the case of rare gases proper conversion by IAT is guaranteed because their 3D velocity distribution is isotropic which must be cylindrical symmetric along all the axes. On the other hand the application of IAT for C_{60} fragment ions is also fulfilled as the 3D velocity distribution of the C_{60} molecular beam is cylindrical symmetric with respect to the x axis which is parallel to the plane of PSD [2]. This constraint is satisfied for the detection of parent ions, such as C_{60}^+ and C_{60}^{2+} , because the 3D velocity distribution of the C_{60} molecular beam is cylindrical symmetric with respect to the x axis (Figure 2.3b). Furthermore, IAT is applicable even for dissociated ions, such as C_{58}^+ and C_{56}^+ , if the polarization vector of synchrotron radiation is directed to the x axis.

Using the cross-sectional image in the x-y plane, we have then calculated the radial distance r between the origin and each pixel and obtained a histogram of pixel intensities as a function of r , which will be hereafter called the radial distribution. Finally, the radial distribution was converted to the speed distribution by using the change of variable,

$$r = v t_{WM} \quad (3.2)$$

where v represents the speed (i.e. velocity magnitude), and t_{WM} the TOF value calculated from the Wiley-McLaren formula [19].

3.3 Simulated image of He ions

We have simulated the projection of the 3D velocity distribution of He at 300 K and compared them with the experimentally obtained images. The number of He atoms used in the simulation was set to $N = 10^5$. It is assumed that the ionization takes place at the origin and that each He^+ ion flies from the origin with keeping its original thermal velocity v of a parent He. The speed $v = |\mathbf{v}|$ was simulated by generating random numbers utilizing Metropolis-method from Maxwell-Boltzmann distribution

$$\frac{1}{N} \frac{dN}{dv} = 4\pi \left(\frac{m}{2\pi kT} \right)^{\frac{3}{2}} v^2 \exp\left(-\frac{mv^2}{2kT}\right) \quad (3.3a)$$

where $\frac{1}{N} \frac{dN(v)}{dv}$ is the probability density function of the speed of He atoms at the temperature T . In the right hand, m , k stand for the mass of He, and Boltzmann constant, respectively. The 3D velocity components of He^+ can be expressed as

$$(v_x, v_y, v_z) = (v \sin \theta \cos \phi, v \sin \theta \sin \phi, v \cos \theta) \quad (3.3b)$$

with the polar angle θ with respect to z axis and the azimuth angle ϕ on the x - y plane (see Figure-3 of Appendix-3). We generated uniformly distributed random numbers for $\cos \theta$ and ϕ . The arrival position of the He^+ ion after the flight time t_{WM} should be $(x, y, z) = (v_x t_{WM}, v_y t_{WM}, v_z t_{WM})$. Repeating the above procedure for every He^+ and adding up the number of ions at each volume element $dx dy dz$, we can evaluate the spatial density function.

$$I(x, y, z) = \frac{1}{N} \frac{dN(x, y, z)}{dx dy dz} \quad (3.3c)$$

The 2D image projected on an x-y plane is then calculated by the sum of $I(x, y, z)$ over z as

$$I(x, y) = \sum_z I(x, y, z) \quad (3.3d)$$

The calculated $I(x, y)$ is equivalent to the experimental image on the PSD, if the size of the ionization is sufficiently small and the magnification factor of the VMI lens system is unity. The spatial resolution is set to $dx = dy = 0.1$ mm corresponding to that of the PSD.

3.4 To check velocity focusing conditions of VMI spectrometer using He sample

Eppink and Parker have optimized the voltages applied to their VMI lens system by adjusting the voltage V_E applied to the extractor electrode with keeping the other voltages constant [2]. Following their way of adjusting we determined the optimum focusing conditions by examining the photoion images of rare gases. In the insets of Figure 1, Panels (a – d) show 2D raw images of He^+ at 300 K, i.e. the projections of the 3D velocity distributions on the PSD. The voltages applied to the MCP, repeller, and tube electrodes were $V_{\text{MCP}} = -2200$ V, $V_R = 640$ V and $V_T = -350$ V, respectively. The panels (a – d) correspond to the extractor voltages, $V_E = 338, 343, 348$ and 353 V, respectively. The data acquisition time was 60 s and the average ion count was $\sim 3.5 \times 10^4$ cps. We projected the images onto the horizontal axis of the PSD by summing up pixel intensities in the vertical direction from -128 to +128. This procedure was carried out for the 2D images measured with different V_E values from 338 to 353 V at interval of 5 V. The resultant 4 curves are summarized in Figure 1(e). The curve at $V_E = 353$ V is the sharpest among all the curves. Obviously, the focusing condition depends strongly on the extractor voltages. More generally, optimum conditions were obtained when $(V_E - V_T) / (V_R - V_T) = 0.71$.

3.5 Defocusing parameters

The Panel (a) of Figure 2 shows the ideal 2D projection of He^+ at 300 K which was obtained by simulation as explained in § 3.3 and it is specified as simulation I. By applying the IAT to this image we have obtained the cross-sectional image of Panel (b) and speed distribution in Figure 2(c). A narrow dotted stripe in Panel (b) running along the vertical symmetric axis (i.e. x axis) appears from the noise due to numerical image processing in the IAT and has no physical meaning. The temperature was estimated in Figure 2(c) to be 287 K from the least-squares fit of the calculated data points (filled circles) to the Maxwell-Boltzmann distribution (solid curve). The curve accords well with the experimental curve with $T = 282$ K (Figure 5 k). Similar simulations were executed for Ne and Ar. Their temperatures determined from the simulated speed distributions were found to be in good agreements with those from Figures 5(l) and (m), respectively.

The Panel (a) of Figure 3 shows the experimental 2D projections on the PSD of the 3D velocity distribution of He^+ produced by photoionization of He at $h\nu = 35$ eV in absence of oven with thickness monitor (see Figure 2.3a of chapter 2) installation. The elliptical image of Panel 3(a) whose major axis lies on the y axis suggests that the velocity focusing conditions are not realized all over the ionization volume and that the deformation from the ideal circular image of Figure 2(a) arises from the elongation of the ionization volume along the photon beam path. We performed a different simulation for a quantitative treatment dealing with a finite ionization volume which is referred to simulation II. The spatial distribution of ionization points is represented by the “point spread function”:

$$PSF(x, y) = \frac{1}{2\pi} \cdot \frac{1}{\sigma_x} \exp\left(-\frac{x^2}{2\sigma_x^2}\right) \cdot \frac{1}{\sigma_y} \exp\left(-\frac{y^2}{2\sigma_y^2}\right) \quad (3.5a)$$

where the standard deviations σ_x and σ_y of the two Gaussian functions are called defocusing parameters. Individually, σ_x and σ_y can be correlated to the above deformation in the x and y directions, respectively, because the electric field in the VMI spectrometer has a cylindrical symmetry with respect to the z axis [4]. In simulation II the arrival position of a He^+ ion is given by

$$(x, y, z) = (v_x t_{WM} + \Delta x, v_y t_{WM} + \Delta y, v_z t_{WM} + \Delta z) \quad (3.5b)$$

and the random numbers are generated for Δx and Δy from the distribution of $PSF(x, y)$. Consequently $I(x, y)$ simulated for the defocused ionization volume should differ from that for the single ionization point. Usually, $2\sigma_x$, $2\sigma_y$ are smaller than the full widths at the half maximum (FWHM) of the ionization volume with respect to the x and y coordinates, respectively.

The values of $2\sigma_x$ and $2\sigma_y$ can be obtained from the comparison between experimental and ideal 2D projections, i.e. in Figures 3(a) and 2(a), respectively. In Figure 3(c) the radial distributions of the two images are extracted from their upper ($\phi = 45 - 135^\circ$) and lower ($\phi = 225 - 315^\circ$) triangular areas: the filled circles from Figure 3(a) and filled stars from Figure 2(a). Then $2\sigma_x$ is optimized by simulation II, so that a recalculated radial distribution can get closer to the filled circles. Next, a similar optimization is carried out for $2\sigma_y$ alone starting from the filled circles and filled stars in Figure 3(d). Here, each radial distribution was extracted from the left ($\phi = 135 - 225^\circ$) and right ($\phi = 315 - 45^\circ$) triangular areas of the image. Subsequently the best combination of $2\sigma_x$ and $2\sigma_y$ can be determined after iterative optimization by simulation II. Panel (b) of Figure 3 shows the

optimized image with $2\sigma_x = 0.2$ mm and $2\sigma_y = 2.8$ mm. This image is in a good agreement with that experimentally obtained in Figure 3(a), indicating that the influence of the elongated ionization volume on the VMI experiments has been well reproduced by introducing $2\sigma_x$ and $2\sigma_y$.

We evaluated $2\sigma_x$ and $2\sigma_y$ from the experimental 2D projections measured at different V_E values from 338 to 353 V at intervals of 5 V with keeping the other electrode voltage constant. The best focusing condition was attainable at $V_E = 353$ V (see §3.4) and the focusing gets worse with decreasing V_E . Indeed $2\sigma_y$ is found to monotonically increase from 2.4 – 2.8 to 4.6 with the decrease of V_E from 353 V to 338 V. This observation clearly shows that σ_y can be used as a appropriate index of the degree of defocusing.

As the fullerene beam source and oven with thickness monitor made distortion of the electric field inside the VMI lens system so we also optimized the defocusing parameters with following the similar processes as mentioned above. The details of this observation are depicted in Figure 4. Here, in the insets, Panel (a) is experimental best focused 2D raw image of He^+ measure at 300 K with oven and thickness monitor installation, Panel (b) is simulated 2D projection of He at 300 K after optimization of σ_x and σ_y . In both of Figures 4(c) and (d) filled circles, filled stars as well as solid curves are corresponding to the experimental data points, simulated data points with $2\sigma_x = 2\sigma_y = 0$ mm as well as simulated data points with $2\sigma_x = 1.7$ and $2\sigma_y = 3.2$ mm, respectively.

3.6 Speed distribution of rare gases

In the insets of Figure 5, Panels (a – e) show the 2D projections of the 3D velocity distributions on the PSD of five rare gases after photoionization at $h\nu = 35$ eV. Applying the IAT to the images provided us with the cross-sectional images in the x-y plane are shown in Panels (f – j) from which we extracted the speed distributions and plotted them in Figures (k – o). As the horizontal part of the image is affected by the ionization volume elongating along the photon beam path (i.e. y axis) so the speed distributions of Figures (k - o) were extracted from the upper ($\phi = 45 - 135^\circ$) and lower ($\phi = 225 - 315^\circ$) triangular areas of Panels (f - j). Each Figure includes the experimental data points (filled circles) for the speed distribution computed from the image (see §3.2), the best fitted curve (solid curve) to which the least-squares fit of the experimental data points were made, and the Maxwell-Boltzmann distribution at 300 K (dash curves). In the fitting procedure, we have assumed the Maxwell-Boltzmann distribution with an adjustable parameter of the temperature. The temperatures obtained by the fittings of Panels (a – e) are 282, 272, 295, 412, and 243 K, respectively. The best fitted curves of the lighter three rare gases (He, Ne, and Ar) are in reasonable agreements with the distribution at 300 K. Small deviation from 300 K can be accounted for by systematic errors peculiar to the numerical image processing in the IAT. For Kr and Xe the agreement is much worse mainly due to smaller signal-to-background ratios. Furthermore, the best fitted curve of Xe in Panel (o) appears to shift by 60 K in the direction of lower speed as compared to the expected distribution at 300 K. This shift can be explained as that the raw image of Xe includes not only Xe^+ but also Xe^{2+} signal counts. As a result, the size of the image shrinks a little and the radial distribution of the image shifts to smaller r , because t_{WM} of Xe^{2+} is smaller by a factor of $1/\sqrt{2}$ than the Xe^+ [5]. Then the

speed distribution should also shift to lower v , as long as t_{WM} of Xe^+ is used, on the whole, for the conversion from r to v in equation (3.2).

3.7 Temperature table by using rare gas image

In the VMI technique, when the velocity focusing conditions are not realized all over the ionization volume then the experimental images are deformed from their circular shape. The projected (raw) rare gas images onto the PSD have elliptical shaped which suggest that the image is influenced by the ionization volume elongating along the photon beam path. Before applying the inverse Abel transformation (IAT) we need centering and symmetrizing the raw image because without doing it IAT amplify the noise and errors on the image excessively [5,20-24]. In our image data, we have used a 2D image frame with 256×256 pixels. Obviously, the coordinates of the center of image frame (i.e. the origin of image frame) is (128, 128) and for simplicity it is symbolized by (C_x, C_y) . As the projected image onto the PSD is usually displaced from the origin of the image frame so we need to shift the raw image towards the origin of image frame. For this purpose we need to know the center of projected image (raw image) as well as x_{sft} and y_{sft} values. Here, x_{sft} and y_{sft} values are the distances between the center of image frame (C_x, C_y) and the center of raw image with regarded to x (i.e. cylindrical symmetric axis), and y (synchrotron radiation direction) axes, respectively which is shown in the Figure 6 (a). Using program codes in “Python” [25] language we have changed x_{sft} and y_{sft} values for shifting the raw image towards the origin of the image frame. To change every pixel of x_{sft} and y_{sft} , we have evaluated the temperature from the corresponding speed distributions by the least-squares fit of the data points to the Maxwell-Boltzmann distribution. We have found dissimilar temperatures for each pixel of x_{sft} and y_{sft} changing around the position at the origin of the image frame because the shifted image has different intensity at each pixel. By plotting the x -values regarding as the center vs. the y -values regarding as the center, we

have made the temperature table which is shown in Figure 6(b). From this temperature table, we have found a clear minimum in temperature at (119, 131) for He image. This minimum agrees with the center of gravity in x- and y-projections. The change of the center plus / minus 2 gives the change of the temperature of at most 5 K. The difference of plus / minus 2 can be easily discriminated in the x- and y-projections.

3.8 Conclusions

Using our VMI spectrometer, we have experimentally reconstructed the 3D velocity distributions of rare gases from the 2D projected image at PSD by using the IAT. Concurrently, we have performed the simulations to extract the speed distributions of rare gas samples at 300 K. From the above two distributions, we have evaluated the temperatures by assuming the Maxwell-Boltzmann distribution. Moreover, a close inspection of the simulated images revealed that the defocusing effect due to a definite ionization volume can be well reproduced by introducing two Gaussian functions as (a) $2\sigma_x = 0.2$ and $2\sigma_y = 2.8$ mm in absence of oven with thickness monitor inside the experimental vacuum chamber, (b) $2\sigma_x = 1.7$ and $2\sigma_y = 3.2$ mm when oven with thickness monitor was installed.

We have shifted the raw image by changing each pixel values around the origin of image frame (center of image frame) and evaluated temperatures of rare gas images. By plotting the x-values regarding as the center vs. the y-values regarding as the center, we have made the temperature table which can provide us to find a clear minimum in temperature for rare gas image. This minimum agrees with the center of gravity in x- and y-projections. The change of the center plus / minus 2 gives the change of the temperature of at most 5 K. The difference of plus / minus 2 can be easily discriminated in the x- and y-projections.

References

- [1] D. W. Chandler and P. L. Houston, *J. Chem. Phys.* 87 (1987) 1445-1447.
- [2] A. T. J. B. Eppink and D. H. Parker, *Rev. Sci. Instrum.* 68 (1997) 3477-3484.
- [3] T. Suzuki and B. Whitaker, in B. Whitaker (Ed.), *Imaging in Molecular Dynamics: Technology and Applications*. Cambridge University Press, Cambridge, 2003, p.165-186.
- [4] Bhim P. Kafle, Hideki Katayanagi, and Koichiro Mitsuke, in *Synchrotron Radiation Instrumentation, CP879*, edited by J. Y. Choi and S. Rah, American Institute of Physics, New York, 2007, 1809-1812.
- [5] H. Katayanagi, C. Q. Huang, H. Yagi, B. P. Kafle, M. S. I. Prodhan, K. Nakajima and K. Mitsuke, *Rev. Sci. Instrum.* (2008) submitted.
- [6] R. Wörgötter, B. Dünser, P. Scheier, T. D. Märk, M. Foltin, C.E. Klots, J. Laskin and C. Lifshitz, *J. Chem. Phys.* 104 (1996) 1225-1231.
- [7] A. Reinköster, S. Korica, G. Prümper, J. Viefhaus, K. Godehusen, O. Schwarzkopf, M. Mast and U Becker, *J. Phys. B: At. Mol. Opt. Phys.* 37 (2004) 2135-2144.
- [8] K. Mitsuke, H. Katayanagi, J. Kou, T. Mori, and Y. Kubozono, in *Ionization, Correlation, and Polarization in Atomic Collisions, CP811*, edited by A. Lahman-Bennani and B. Lohmann, American Institute of Physics, New York (2006) 161-166.
- [9] J. Laskin, B. Hadas, T. D. Märk, and C. Lifshitz, *Int. J. Mass spectrom.* 177 (1998) L9-L13.
- [10] J. Kou, T. Mori, and Y. Kubozono and K. Mitsuke, *J. Electron. Spectrosc. Relat. Phenom.* 144 (2005) 247-250.
- [11] J. Kou, T. Mori, Y. Kubozono and K. Mitsuke, *Phys. Chem. Chem. Phys.* 7 (2005) 119-123.

- [12] P. N. Juranic, D. Lukic, K. Barger and R. Wehlitz, *Phys. Rev. A* 73 (2006) 042701.
- [13] B. Climen, B. Concina, M.A. Lebeault, F. Lepine, B. Baguenard, C. Bordas, *Chem. Phys. Lett.* 437 (2007) 17-22.
- [14] K. Gluch, S. Matt-Leubner, O. Echt, B. Concina, P. Scheier, and T.D Märk, *J. Chem. Phys.* 121 (2004) 2137.
- [15] H. Gabor, R. Hiss, H. G. Busmann, and I. V. Hertel, *Z. Phys. D Atoms, Molecules and clusters* 24 (1992) 307-309.
- [16] D. Muigg, G. Denifl, P. Scheier, K. Becker, and T. D. Märk, *J. Chem. Phys.* 108 (1998) 963-970.
- [17] S. M. Candel, *Comput. Phys. Commun.* 23 (1981) 343-353.
- [18] LM. Smith and D. R. Keefer, *J. Quant. Spectrosc. Radiat. Transfer* 39 (1988) 367-373.
- [19] W. C Wiley and I. H. McLaren, *Rev. Sci. Instrum.* 26, (1955) 1150.
- [20] V. Dribinski, A. Ossadtchi, V. A. Mandelshtam, and H. Reisler, *Rev. Sci. Instrum.* 73 (7), (2002) 2634.
- [21] G. A. Garcia, L. Nahon, and I. Powis, *Rev. Sci. Instrum.* 75 (11), (2004) 4989.
- [22] R. N. Strickland and D. W. Chandler, *Appl. Opt.* 30 (14), (1991) 1811.
- [23] M. J. J. Vrakking, *Rev. Sci. Instrum.* 72 (11), (2001) 4084.
- [24] A. J. R Heck and D. W. Chandler, *Annu. Rev. Phys. Chem.* 46, (1995) 335.
- [25] G. van Rossum and F. L. Drake, *Python Reference Manual*. (PythonLabs, Virginia, 2001)

Figures of chapter 3

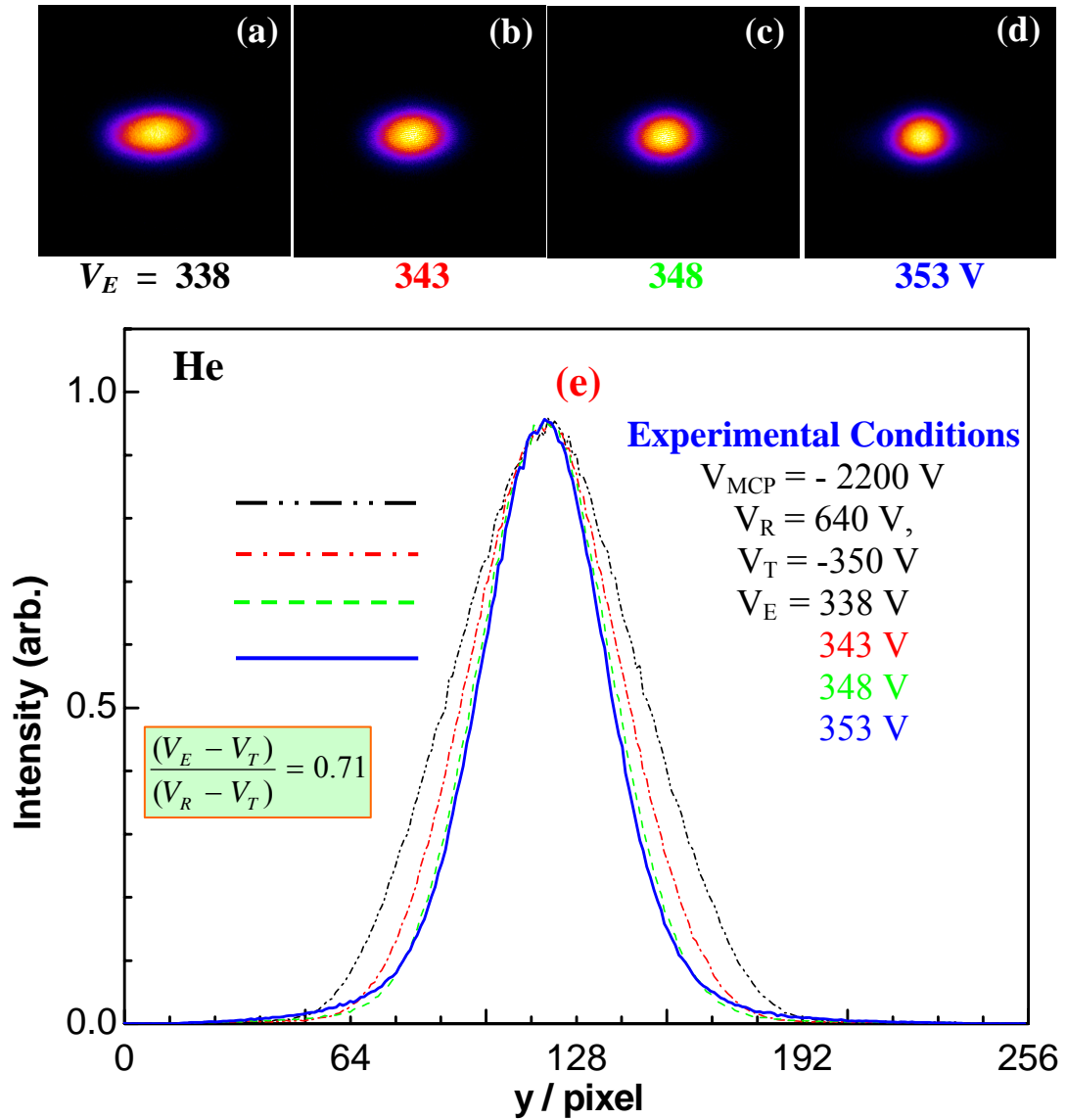


Figure 1

(a) and (b) are raw 2D images of He⁺ on the PSD. The voltages applied to the MCP, repeller, and tube electrodes were $V_{MCP} = -2200$ V, $V_R = 640$ V and $V_T = -350$ V, respectively. The panels (a) – (d) correspond to the extractor voltages, $V_E = 338$, 343 , 348 and 353 V, respectively. The data acquisition time

was 60 s and the average ion count was $\sim 3.5 \times 10^4$ cps. (e) Projection of the 2D images at four different V_E values onto their horizontal axes by integrating intensities in the vertical direction from -128 to +128 pixels.

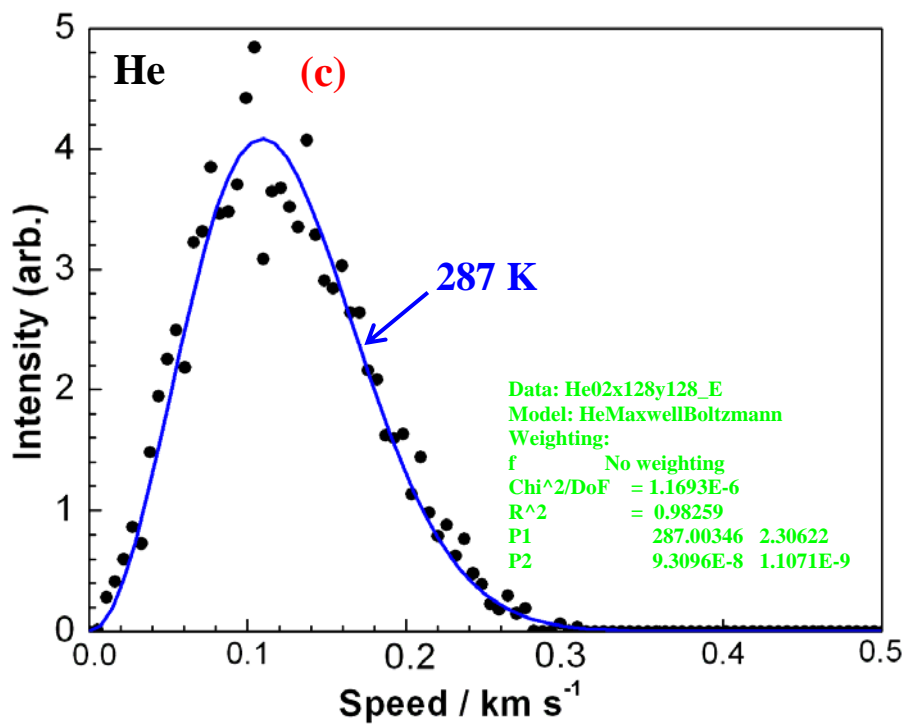
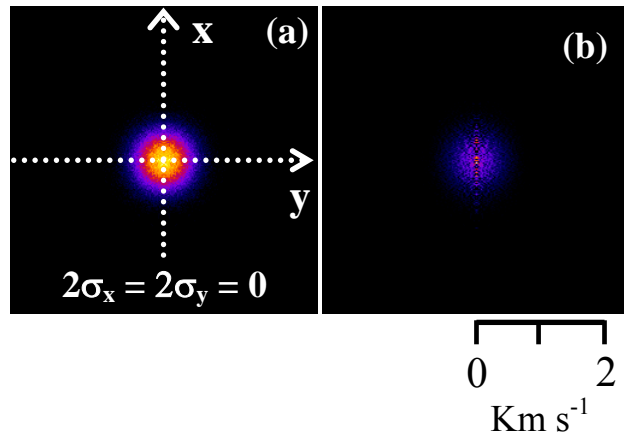
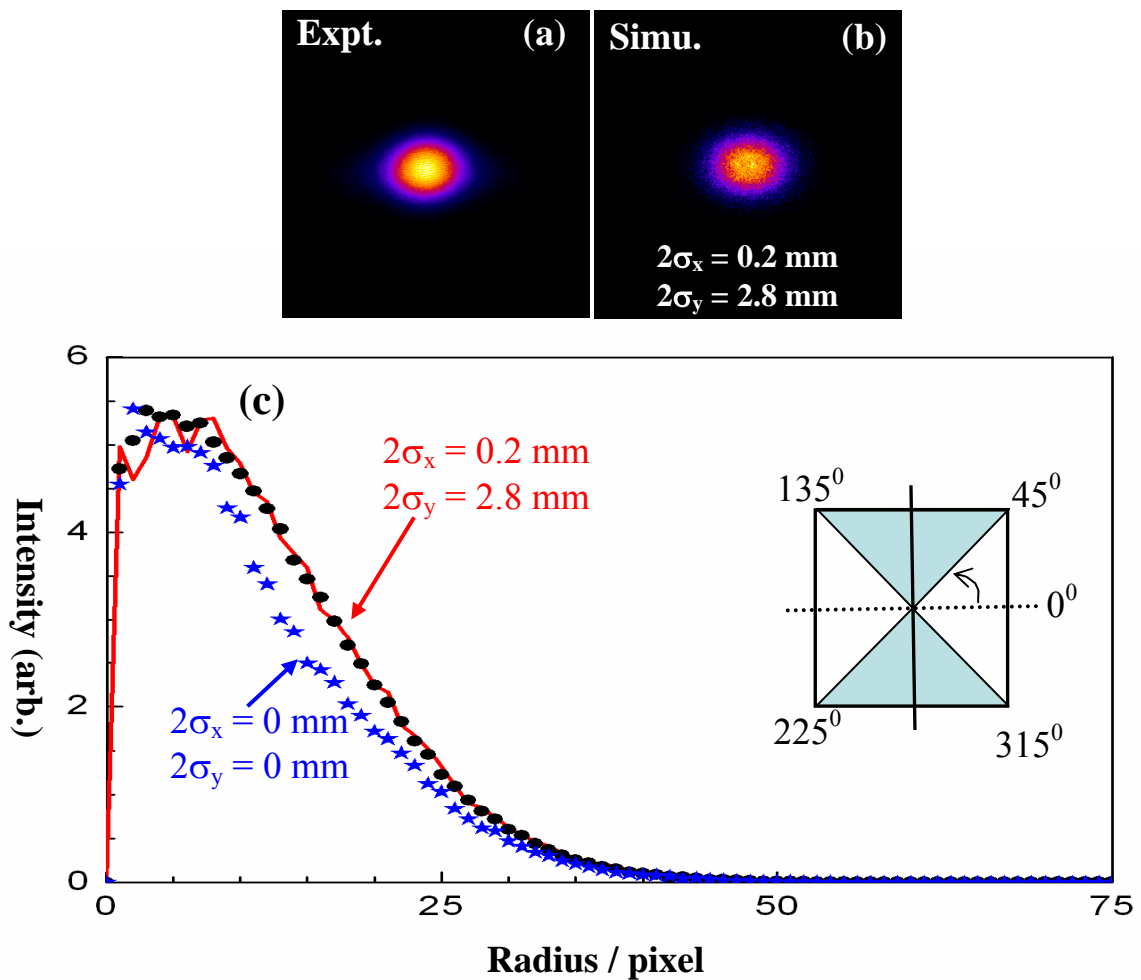


Figure 2

(a) is simulated 2D image of He at 300 K projected on the PSD, (b) the cross-sectional image of the 3D velocity distribution in the x-y plane which was calculated from Panel (a) by using IAT, and (c) the speed distribution extracted from Panel (b). The solid curve indicates the best fitted Maxwell-Boltzmann distribution to which the least-squares fit of the calculated data points \bullet was made.



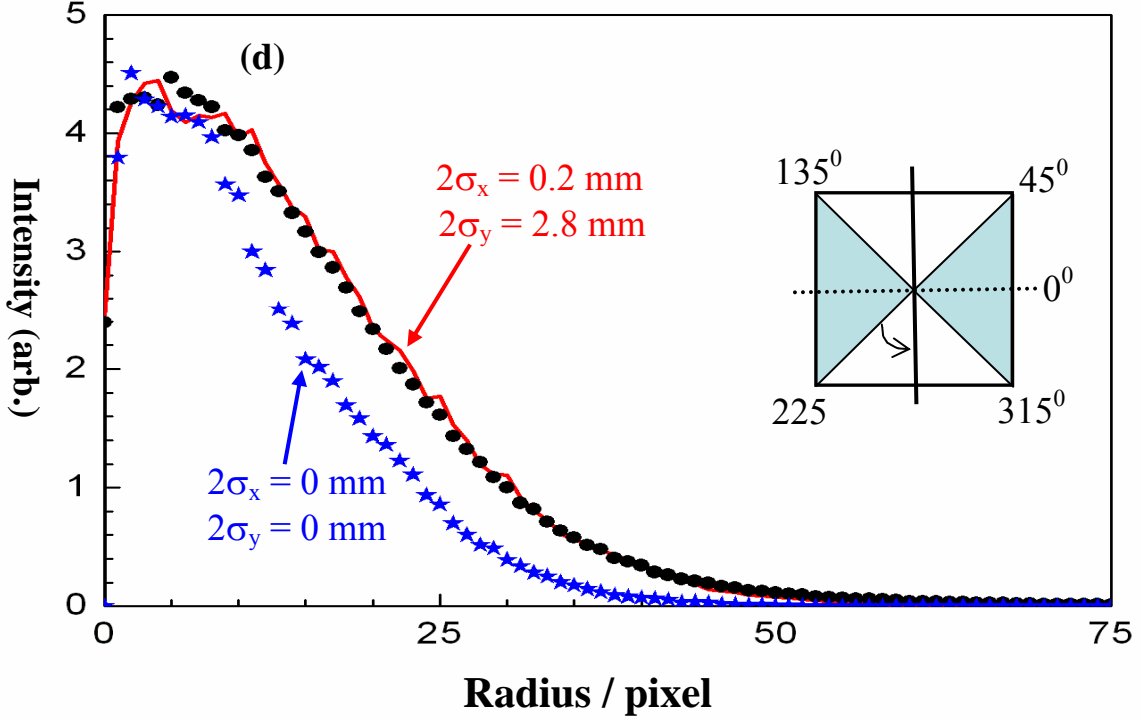
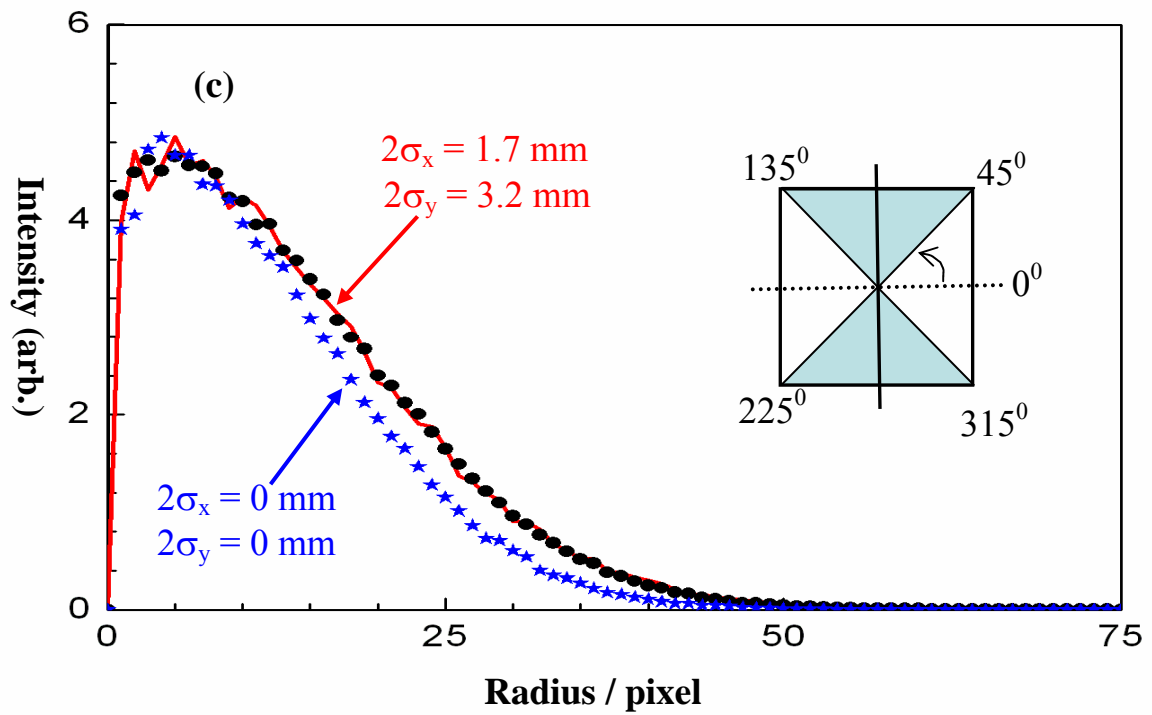
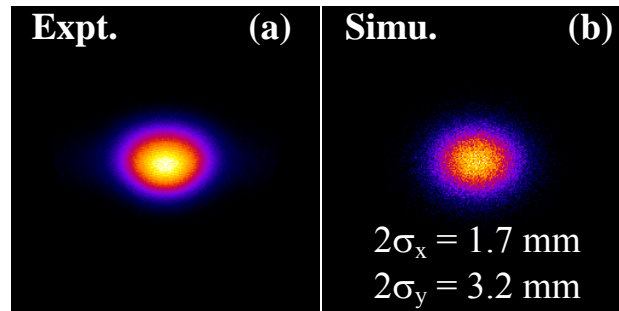


Figure 3

In the insets, Panel (a) is experimental best focused 2D raw image of He^+ measured at 300 K without oven and thickness monitor installation. The applied voltages at the MCP and electrodes are $V_{\text{MCP}} = -2200$ V, $V_{\text{R}} = 640$ V, $V_{\text{T}} = -350$ V and $V_{\text{E}} = 353$ V. Panels (b) is simulated 2D projections of He at 300 K after optimization of σ_x and σ_y , respectively. The radial distributions in Panels (a, b) were extracted from the upper ($\phi = 45-135^\circ$) and lower ($\phi = 225-315^\circ$) triangular areas and plotted in Figure (c). Again, the radial distributions in Panels (a, b) are extracted from the left ($\phi = 135-225^\circ$) and right ($\phi = 315-45^\circ$) triangular areas and plotted in Figure (d). In both of Figures (c) and (d) filled circles, filled stars as well as solid curves are corresponding to

the experimental data points, simulated data points with $2\sigma_x = 2\sigma_y = 0$ mm as well as simulated data points with $2\sigma_x = 0.2$ and $2\sigma_y = 2.8$ mm, respectively.



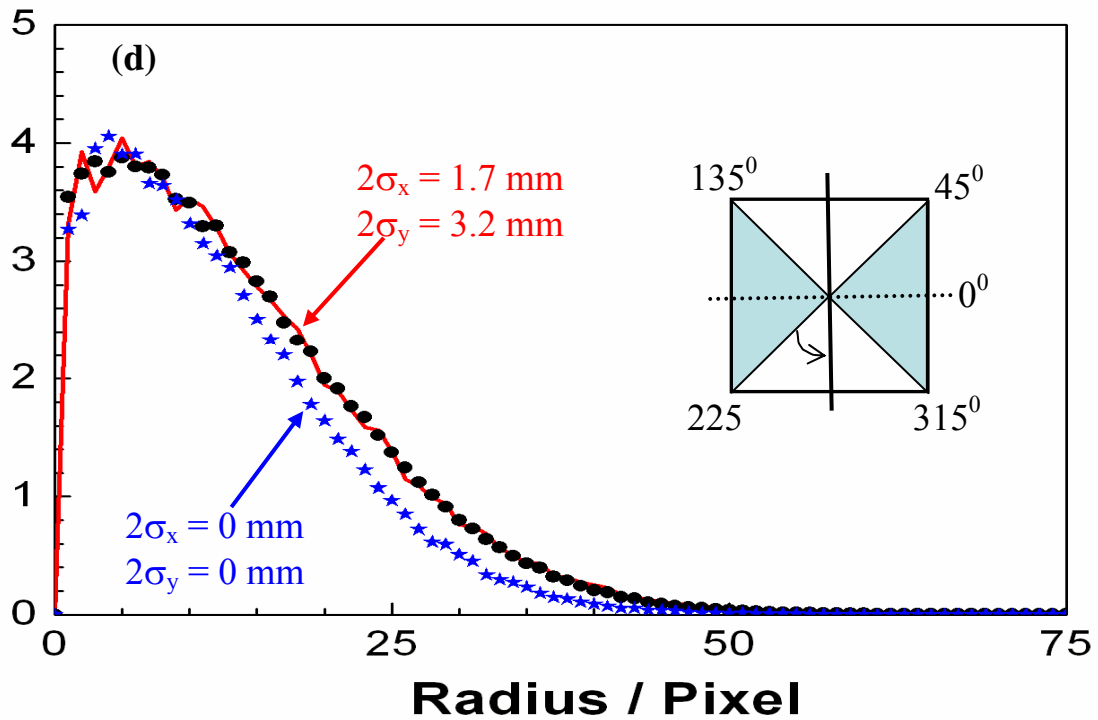
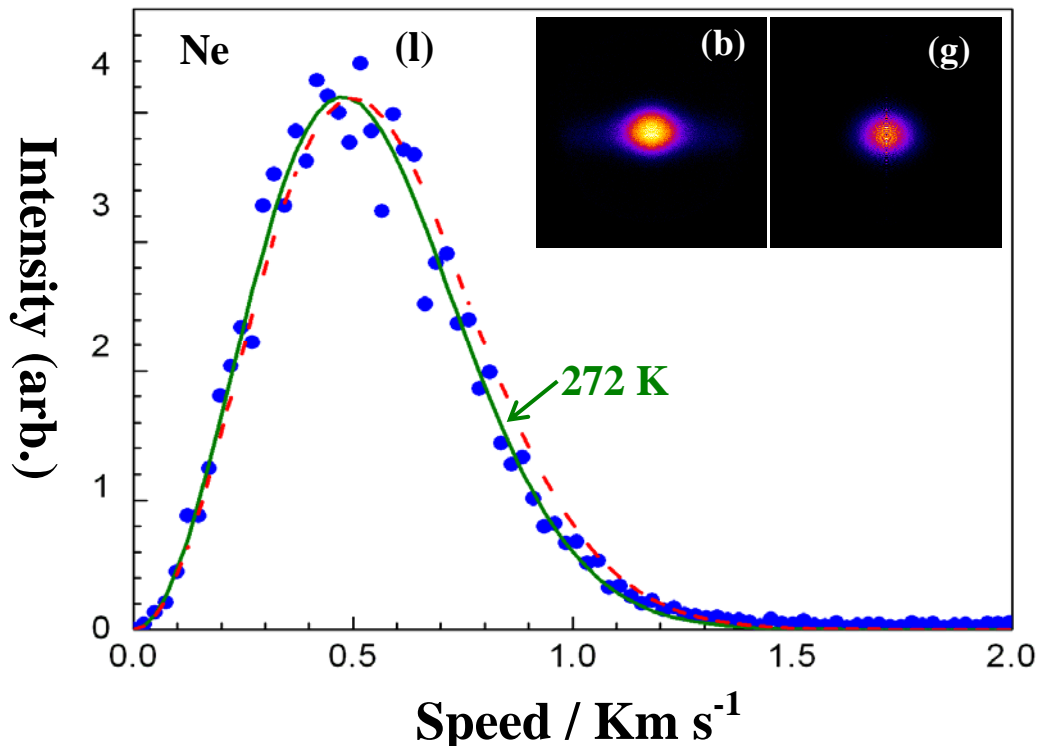
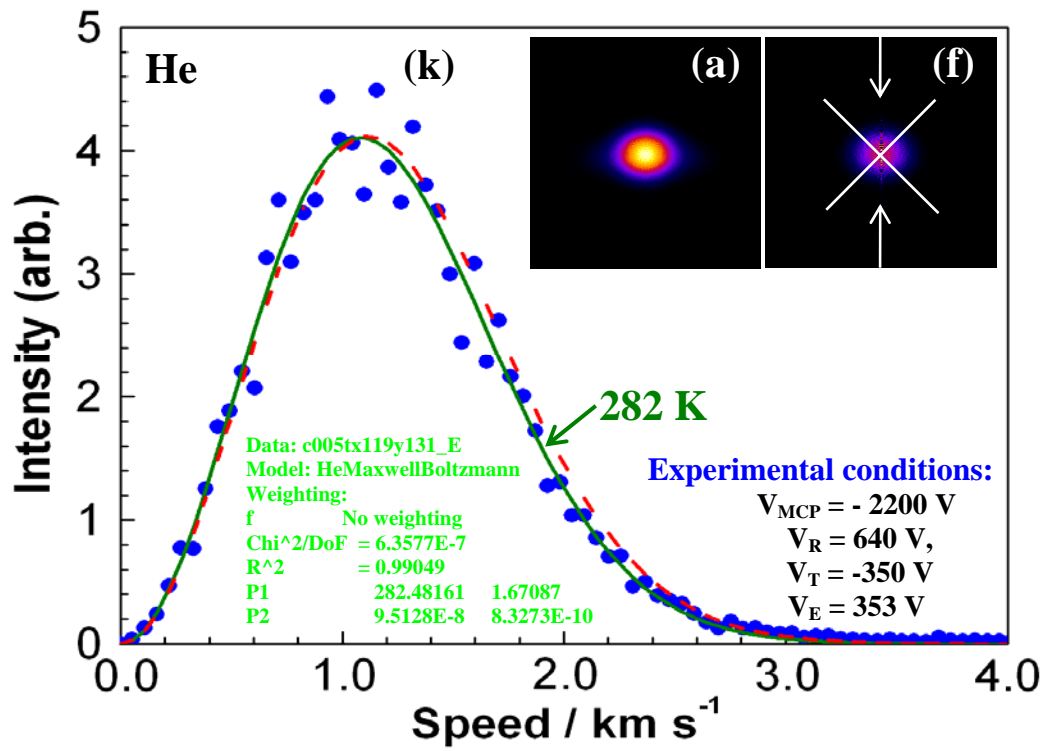
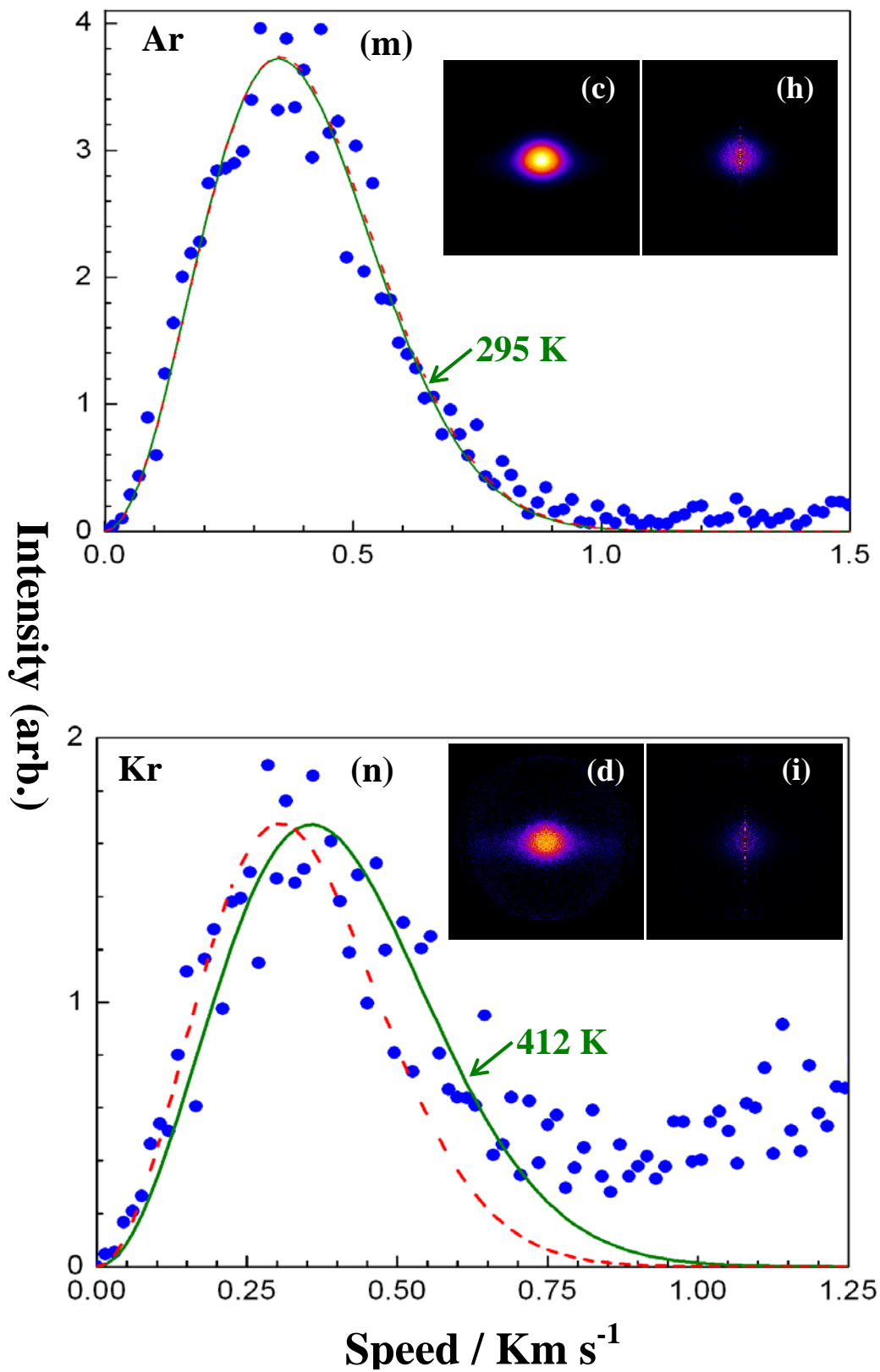


Figure 4

In the insets, Panel (a) is experimental best focused 2D raw image of He^+ measured at 300 K with oven and thickness monitor installation, Panel (b) is simulated 2D projections of He at 300 K after optimization of σ_x and σ_y . The radial distributions in Panels (a, b) were extracted from the upper ($\phi = 45-135^\circ$) and lower ($\phi = 225-315^\circ$) triangular areas and plotted in Figure (c). Again, the radial distributions in Panels (a, b) were extracted from the left ($\phi = 135-225^\circ$) and right ($\phi = 315-45^\circ$) triangular areas and plotted in Figure (d). In both of Figures (c) and (d) filled circles, filled stars as well as solid curves are corresponding to the experimental data points, simulated data points with $2\sigma_x = 2\sigma_y = 0 \text{ mm}$ as well as simulated data points with $2\sigma_x = 1.7$ and $2\sigma_y = 3.2 \text{ mm}$, respectively.





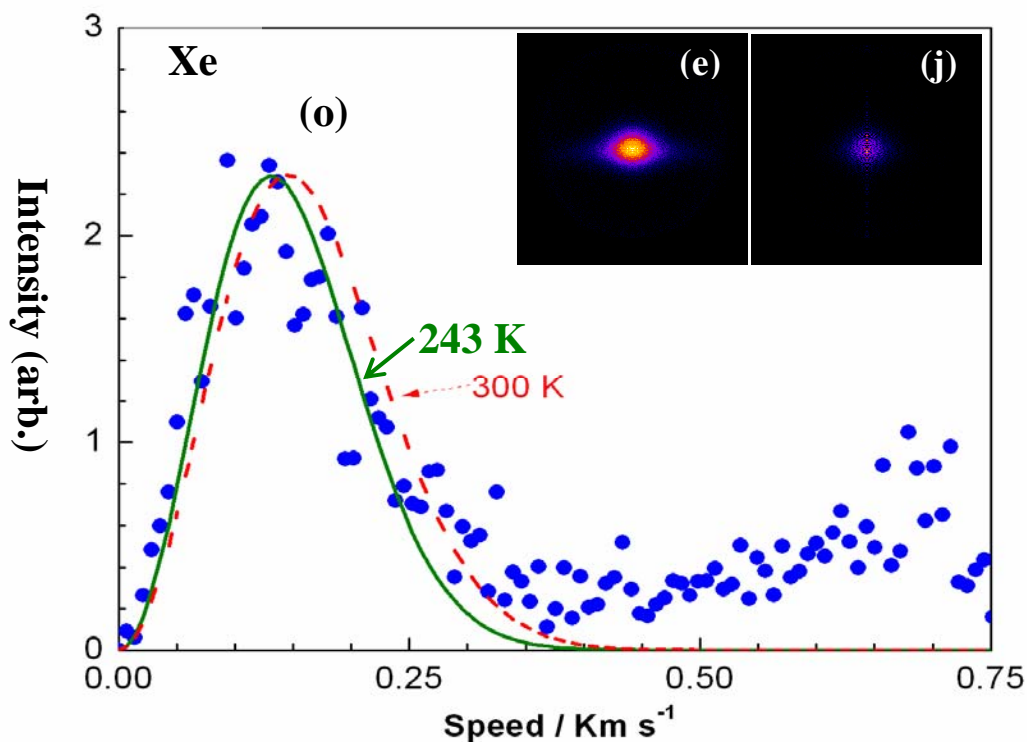


Figure 5

In the insets, Panels (a – e) show experimental 2D raw images of He, Ne, Ar, Kr, and Xe, respectively measured at 300 K. Panels (f – j) the cross-sectional images which were obtained from Panels (a – e), respectively by using the IAT. The speed distributions were extracted from the cross-sectional images in Panels (f – j) and plotted in Figures (k – o), respectively. The solid curves denote the best fitted Maxwell-Boltzmann distributions to which the least-squares fit of the experimental data points • were made, and the dash curves denote the Maxwell-Boltzmann distribution at 300 K.

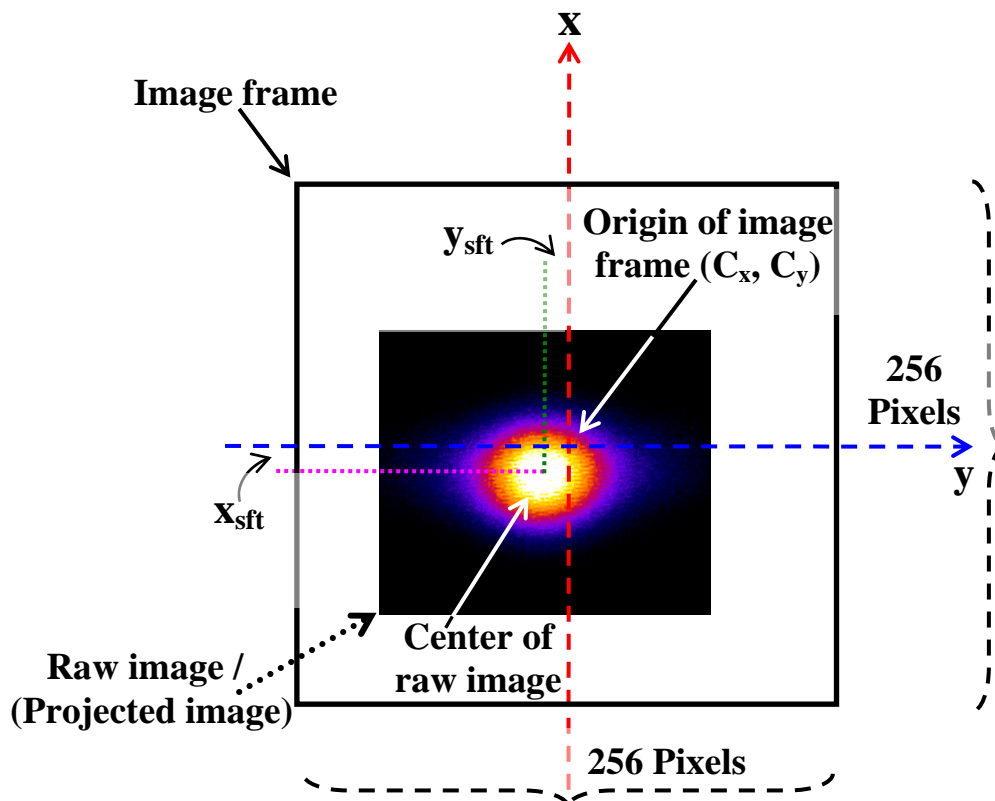


Figure 6(a)

A 2D image frame with 256×256 spatial resolution. C_x and C_y are the coordinates of the origin of image frame (center of image frame). x_{sft} and y_{sft} are the distances between the origin of image frame and the center of raw image with regarded to the x and y axes, respectively.

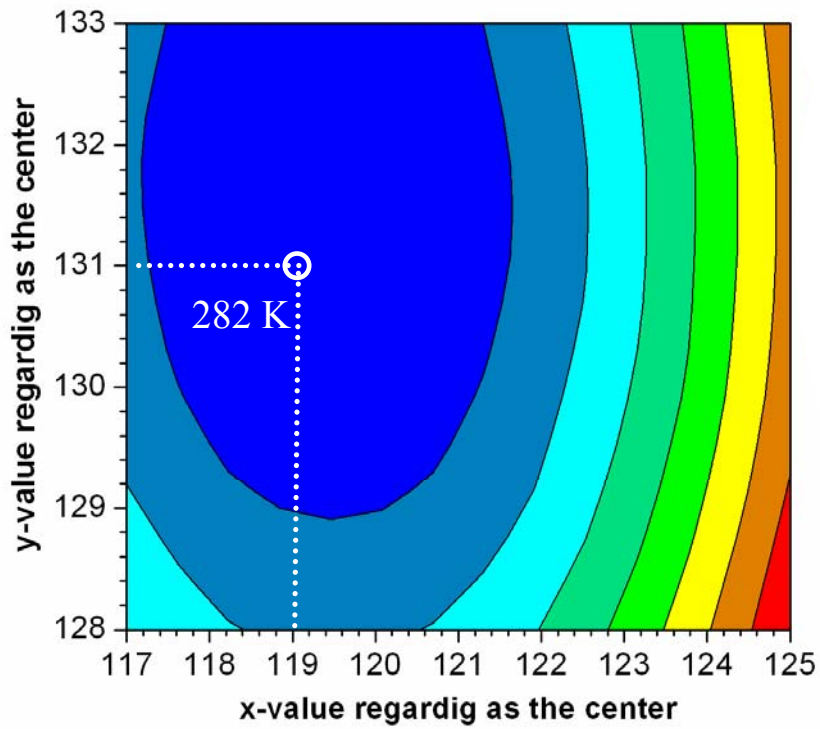


Figure 6(b)

Temperature table extracted from the experimental image of He. Minimum temperature was found at (119, 131) of the image frame. The change of the center plus / minus 2 gives the change of temperature of at most 5 K.

Chapter 4

“Int. J. Mass Spectrometry (to be submitted)”

4.0 Simulating the photoion images of C_{56}^+ fragment ions from C_{60}

4.1 Introduction

In this chapter, the simulation studies of possible processes for C_{60} fragmentations have been established. There are two plausible photofragmentation pathways of excited C_{60} cations, namely the stepwise C_2 -loss and direct fission processes (discussed in sec §3.1). There are only a limited number of experimental works of product analysis of the fragments. Several groups have tried to distinguish these two processes by measuring the total average kinetic energy release (KER) in the decomposition of C_{60}^{z+} into C_{60-2n}^{z+} . Hertel and co-workers [1] evaluated the kinetic energies of C_{60-2n}^{z+} ($1 \leq n \leq 14$) produced by photoionization of C_{60} . Later Märk and co-workers [2] fulfilled electron impact ionization of C_{60} and reported a value of ca. 0.45 eV as the total KER in the decomposition of C_{60} into C_{60-2n}^+ ($1 \leq n \leq 8$). These authors suggested that not only C_2 ejection (C_2 -loss) but also single-step two-fragment fission (C_4 -loss) of parent C_{60}^+ ions could also be a possible process for the formation of C_{60-2n}^{z+} .

However, the results on KER parameter studied by several groups met with failure. The portion of the kinetic energy release partitioned to the fragments was found to be a few tens of meV, and is comparable to or smaller than the average thermal energies of neutral C_{60} molecules in an effusive beam [3]. The two processes therefore give C_{60-2n}^{z+} fragments with similar average kinetic energies in the laboratory frame. This situation should be also the case

for other fullerenes i.e. C_m^{z+} ($m = 70, 76, 78, 84$, and so forth). Obviously, we must observe a precise 3D velocity distribution, speed and angular distribution, to gain helpful clue to decide on which process is more dominant. We have demonstrated a methodology and results on the simulation for the image of the 3D velocity distributions of C_{56}^+ to discuss the feasibility of the VMI experiments of C_{60} beams.

Moreover, in an experimental view, the image of C_{56}^+ might be contaminated by the background dark counts due to impurities such as water, air, and organic compounds. So, we have also tried to remove the background counts from the measured 2D image by means of deconvolution using the low-pass and Wiener filters [4].

4.2 Assumptions in the scattering distribution program of C_{60}

The fundamental notion of the velocity map imaging (photofragment imaging) is followed in several steps as (i) creation of the ion clouds or spheres by photodissociation; (ii) conversion of the photofragments to ions by laser or synchrotron radiation (SR) photoionization; (iii) projection of the ionic clouds or spheres onto a two-dimensional position-sensitive detector (PSD); and (iv) recovery of the three-dimensional information from the 2D image by using some sophisticated mathematical transformations.

In this simulation program we assumed that the parent ion C_{60}^+ is in the rest and it starts to dissociate into its smaller fragments. In the case of C_2 -loss process, C_{60}^+ ion (red colour) dissociates in radial direction into C_{58}^+ ion (violet colour). Then C_{58}^+ ion again dissociates in radial directions into C_{56}^+ ion (blue colour). As a result the “clouds” of charged particles (a set of expanding nested spheres) [5] creates as depicted in Figure 1(a). But in the case of C_4 -loss process, C_{60}^+ ions dissociate in radial directions directly into C_{56}^+ ions and create a 3D expanding ion clouds which is shown in Figure 1(b). For both of two processes these 3D ion spheres are projected onto the 2D PSD. From the projected 2D

image we can extract the 3D velocity distribution, speed and angular distributions.

4.3 Simulated image of C_{56}^+ from C_{60}

In the course of discussion in §3.5 and §3.6 important features of the present VMI spectrometer having come to the front are its high sensitivity to internal ions with relatively small translational energies and high velocity resolution realized by the PSD. These features were helpful in our achieving the 3D velocity distribution of the photoions from rare gas atoms at room temperature. It should also be noted that we have succeeded in determining the speed and angular distributions of C_{60}^{z+} ($z = 1, 2$) produced from C_{60} molecular beams by using the same experimental setup [3]. In this chapter, we will discuss the feasibility of the VMI studies of the fragment ions from C_{60} , by taking an example of the simulation for the image of scattering distributions of C_{56}^+ produced through the C_2 - and C_4 -loss processes [6,7].

4.3.1 Bulk C_{60} at $T = 0$ K

Panels (a) and (c) in Figure 2 show the simulated 2D projections given by VMI of C_{56}^+ fragment ions produced from C_{60} molecules at rest (i.e. $v(C_{60}) = 0$ or $T = 0$) through the C_2 - and C_4 -loss processes, respectively. By reference to the literature [1,8] the total average KER was set to 0.4 eV, whether C_2 or C_4 is dissociated from a fullerene ion. Applying the IAT [9-11] to Panels 2(a) and (c) leads to the cross-sectional images in Panels 2(b) and (d), respectively, from which we extracted the speed distributions of C_{56}^+ in Figure 2(e). The speed distribution based on the C_4 -loss process exhibits a sharp peak at ~ 86 m s⁻¹ corresponding to the value of $v'_{CM}(C_{56}^+) = 87$ m s⁻¹ derived from the momentum and energy conservation law in equation 4.4(e). This peak is ascribable to the intense ring patterns observed in Panels 2(c) and (d). In contrast, the speed distribution based on the C_2 -loss process is much broader (filled

circles in Figure 2e) than the C_4 -loss process (stick-like curves in Figure 2e) because the vector sum of $v_{CM}(C_{58}^+)$ and $v_{CM}(C_{56}^+)$ can populate randomly over a wide range of the velocity space.

4.3.2 Bulk C_{60} at $T = 273$ K

Panels (a) and (c) in Figure 3 show the simulated 2D projections given by VMI of C_{56}^+ produced by, respectively, the C_2 - and C_4 -loss of C_{60} at $T = 273$ K. Panels 3(b) and (d), showing the corresponding cross-sectional images converted from the Panels 3(a) and (c), respectively, are further processed to the speed distributions of C_{56}^+ in Figure 3(e). The two curves for different processes have similar shape, so that it is difficult to distinguish them even on the level of simulation I. We estimated the temperature of C_{56}^+ to be 474 K and 492 K for the C_2 - and C_4 -loss processes, respectively, by the least-squares fit of the data points to the Maxwell-Boltzmann distribution. A difference of 18 K might be correlated with the difference in fragmentation processes, but such a small deviation is fully smeared out by scattered data points in the experiments.

4.3.3 Bulk C_{60} at $T = 785$ K

In photoionization experiments of gaseous C_{60} the powder of C_{60} is heated up at 700 – 800 K in sample cell and vaporized into vacuum [12-15]. The C_{60} beam thus generated is expected to obey the condition of an effusive flow [3]. Hence the beam is considered to have the same temperature as the sample cell. Moreover, the beam divergence is confined by a nozzle and orifices situated between the sample cell and VMI lens system. As a result the transverse velocity of the C_{60} beam was found to be less than 20 m s^{-1} . In our experimental setup the maximum divergence angle is estimated to be 10 – 20 degrees [3].

With this conditions in mind we have simulated the images of 3D velocity distributions of C_{56}^+ produced in the C_{60} beam at $T = 785$ K whose speed distribution is illustrated in Figure 4(a). The symmetry axis of the C_{60} beam path agrees with the x axis. The divergence angle was set to 14 degree. Panels (b) and

(d) in Figure 4 show the images of C_{56}^+ produced by the C_{2-} and C_{4-} loss processes, respectively. We then performed conversion from Panels (b) and (d) to the cross-sectional images, Panels (c) and (e), respectively. There is a clear difference between the intensity distributions of the two images. In particular, the high intensity concentrated on the x axis in Panel (c) contrasts in a striking manner with the distribution of Panel (e) which has two intense stripes near the right and left sides of the image (Note that the cross-sectional image of the 3D velocity distribution has a mirror symmetry with respect to the x axis in Panel 4(e). The widths of the stripes appear to increase with increasing x, reflecting the divergence of the C_{60} beam. We can expect that the above marked difference in the image pattern between the two processes permits us to obtain convincing evidence on which process dominates photofragmentation of C_{60} in the extreme UV region. The intense stripes of Panel (e) of Figure 4 originate from the ring pattern in the simulated image of C_{56}^+ produced by the C_{4-} loss process from C_{60} at rest (see Panels (c, d) of Figure 2). Under bulk conditions the ring pattern becomes less clear with increasing temperature and is almost smeared out due to the convolution of the thermal velocity of parent ions at $T = 273$ K (see Panels (c, d) of Figure 3). On contrary, the nominal temperature associated with the transverse velocity of the C_{60} beam is extremely low even at $T = 785$ K. Thus, the intense regions still remain near each side of the image of the C_{56}^+ produced by the C_{4-} loss process.

The defocusing effect due to the elongated ionization region is not taken into account in our simulation for the image of Figure 4. This effect on the C_{56}^+ images was hence investigated by simulation II with $2\sigma_x = 0.2$ mm and $2\sigma_y = 2.8$ mm. From the simulation we found that the C_{4-} loss process can be readily distinguished from the C_{2-} loss process by the broader $I(x, y)$ distribution with respect to the y axis, though the intense stripes in Figure 4(e) become blurred due to defocusing.

4.4 To verify $v_{CM}(C_{58}^+)$ and $v_{CM}(C_{56}^+)$ at different KER in C_2 -loss and C_4 -loss processes

It is known that there are two possible photofragmentation processes of C_{60} , namely the step-wise C_2 -loss and direct fission with C_4 -loss [1,2,7]. In the case of C_2 -loss process, the conservation laws of momentum and energy lead to the 3D velocity $v_{C_{56}^+}$ of C_{56}^+ produced from C_{60} having a form of

$$v_{C_{56}^+} = v_{C_{60}} + v_{CM}(C_{58}^+) + v_{CM}(C_{56}^+) \text{ -----(4.4a)}$$

For C_2 -loss process, from momentum and energy conservation we can write

$$\left. \begin{aligned} m_{C_2} \times v_{C_2} &= m_{C_{58}} \times v_{C_{58}} \\ \frac{1}{2}(m_{C_2} \times v_{C_2}^2 + m_{C_{58}} \times v_{C_{58}}^2) &= E_K \end{aligned} \right\} \text{-----(4.4b)}$$

Using equation (4.4b) we can derive,

$$v_{CM}(C_{58}^+) = \left[\frac{2 L e E_K}{720 \times 10^{-3}} \cdot \frac{2}{58} \right]^{\frac{1}{2}} \text{ -----(4.4c)}$$

$$v_{CM}(C_{56}^+) = \left[\frac{2 L e E_K}{696 \times 10^{-3}} \cdot \frac{2}{56} \right]^{\frac{1}{2}} \text{ -----(4.4d)}$$

Here, $v_{CM}(C_{58}^+)$ and $v_{CM}(C_{56}^+)$ denote the center-of-mass velocities of C_{58}^+ and C_{56}^+ fragment ions produced in the first and second steps, respectively, of the C_2 -loss process. In equations (4.4b ~ 4.4d), e is the elementary charge in coulomb, L is Avogadro's constant, and E_K is the total KER in the C_2 ejection which takes a constant value of 0.4 eV, as reported by other workers [1,2,8]. In

the case of C_4 -loss mechanism, the 3D velocity $v'(C_{56}^+)$ of C_{56}^+ produced from C_{60} can be given as

$$v'_{C_{56}^+} = v_{C_{60}} + v'_{CM}(C_{56}^+) \text{ -----(4.4e)}$$

$$v'_{CM}(C_{56}^+) = \left[\frac{2 L e E_K}{720 \times 10^{-3}} \cdot \frac{4}{56} \right]^{\frac{1}{2}} \text{ -----(4.4f)}$$

Here, $v'_{CM}(C_{56}^+)$ denotes the center-of-mass velocity of C_{56}^+ produced under the C_4 -loss process. The total KER in the C_4 ejection is assumed to be equal to 0.4 eV.

From Equations (4.4c), (4.4d) and (4.4f) it is clear that the center-of-mass velocity $v_{CM}(C_{58}^+)$ or $v_{CM}(C_{56}^+)$ directly depends on the total KER. We have developed program codes to manipulate and analyze the images with utilizing “Python”[16] and “C” [17] programming languages. Before using the program codes we needed to check their performance in producing the center-of-mass velocities with accord to KER. To determine the center-of-mass velocities (fragment velocities), $v_{CM}(C_{58}^+)$ for the first step reaction in the C_2 -loss process we have considered the initial beam temperature (thermal) and the kinetic energy released in the second step reaction are 0 K, and 0 eV, respectively. Then we have calculated $v_{CM}(C_{58}^+)$ using kinetic energy range from 0.1 eV to 0.8 eV keeping at interval of 0.1 eV. The calculated center-of-mass velocities were 30.38, 42.97, 52.62, 60.76, 67.93, 74.42, 80.38, and 85.93 $m s^{-1}$ corresponding to the kinetic energies for 0.1, 0.2, 0.3, 0.4, 0.5, 0.6, 0.7, and 0.8 eV, respectively. On utilizing photoion imaging programs we have generated the C_{58}^+ ion images in the first step reaction in C_2 -loss process by using kinetic energy range from 0.1 eV to 0.8 eV with keeping at interval of 0.1 eV. After analyzing these image data, we have found $v_{CM}(C_{58}^+) = 28.08, 40.56, 49.92,$

59.28, 65.52, 71.76, 78.0, and 84.24 m s⁻¹ for energy range from 0.1eV to 0.8 eV, respectively.

Finally, it is concluded that the theoretical center-of-mass velocities of C₅₈⁺ ions and the simulated center-of-mass velocities of C₅₈⁺ ion images with using different KE release are well matching except a variation of maximum 2 to 8%. The velocities $v_{CM}(C_{58}^+)$ and $v'_{CM}(C_{56}^+)$ of C₅₆⁺ produced from C₆₀ in the C₂- and C₄-loss processes, respectively, are also expected to give the same results as of $v_{CM}(C_{58}^+)$. Obviously our photoion imaging programs are nicely fitted to image generation of C₆₀ fragments with proper magnitude of velocities.

4.5 Wiener (Optimal) Filtering with the FFT

There are a number of other tasks in numerical processing that are routinely handled with Fourier techniques. One of these is filtering for the removal of noise from a “corrupted” signal. The particular situation we consider is this: there is some underlying, uncorrupted signal $u(t)$ that we want to measure. The measurement process is imperfect, however, and what comes out of our measurement device is a corrupted signal $c(t)$. The signal $c(t)$ may be less than perfect in either or both of two respects. First, the apparatus may not have a perfect “delta-function” response, so that the true signal $u(t)$ is convolved with (smeared out by) some known response function $r(t)$ to give a smeared signal $s(t)$,

$$s(t) = \int_{-\infty}^{\infty} r(t-\tau) u(\tau) d\tau \text{ or } S(f) = R(f) U(f) \text{ ----- (4.5a)}$$

where S , R , U are the Fourier transforms of s , r , u , respectively. Moreover, t and f are used for time and frequency respectively. Second, the measured signal $c(t)$ may contain an additional component of noise, $n(t)$

$$c(t) = s(t) + n(t) \text{ ----- (4.5b)}$$

We already know how to deconvolve the effects of the response function r in the absence of any noise; we just divide $C(f)$ by $R(f)$ to get a deconvolved signal. We now want to treat the analogous problem when noise is present. Our task is to find the optimal filter, $\phi(t)$ or $\Phi(f)$, which, when applied to the measured signal $c(t)$ or $C(f)$, and then deconvolved by $r(t)$ or $R(f)$, produces a signal $\tilde{u}(t)$ or $\tilde{U}(f)$ that is as close as possible to the uncorrupted signal $u(t)$ or $U(f)$. In other words we will estimate the true signal U by

$$\tilde{U}(f) = \frac{C(f) \Phi(f)}{R(f)} \text{ ----- (4.5c)}$$

In what sense is \tilde{U} to be close to U ? We ask that they be close in the least-square sense

$$\int_{-\infty}^{\infty} |\tilde{u}(t) - u(t)|^2 dt = \int_{-\infty}^{\infty} |\tilde{U}(f) - U(f)|^2 df \text{ ----- (4.5d)}$$

is minimized.

Substituting equations (4.5b) and (4.5c), the right-hand side of (4.5d) becomes

$$\begin{aligned} & \int_{-\infty}^{\infty} \left| \frac{[S(f) + N(f)] \Phi(f)}{R(f)} - \frac{S(f)}{R(f)} \right|^2 df \text{ ----- (4.5e)} \\ & = \int_{-\infty}^{\infty} |R(f)|^{-2} \left\{ |S(f)|^2 |1 - \Phi(f)|^2 + |N(f)|^2 |\Phi(f)|^2 \right\} df \end{aligned}$$

The signal S and the noise N are uncorrelated, so their cross product, when integrated over frequency f , gave zero. (This is practically the definition of what we mean by noise!) Obviously equation (4.5e) will be a minimum if and only if the integrand is minimized with respect to $\Phi(f)$ at every value of f . Let us search for such a solution where $\Phi(f)$ is a real function. Differentiating with respect to Φ , and setting the result equals to zero gives

$$\Phi(f) = \frac{|S(f)|^2}{|S(f)|^2 + |N(f)|^2} \text{ ----- (4.5f)}$$

This is the formula for the optimal filter $\Phi(f)$.

Notice that equation (4.5f) involves S , the smeared signal, and N , the noise. The two of these add up to be C , the measured signal. Equation (4.5f) does not contain U , the “true” signal. This makes for an important simplification: The optimal filter can be determined independently of the determination of the deconvolution function that relates S and U .

To determine the optimum filter from equation (4.5f) we need some way of separately estimating $|S|^2$ and $|N|^2$. There is no way to do this from the measured signal C alone without some other information, or some assumption or guess. Luckily, the extra information is often easy to obtain. For example, we can sample a long stretch of data $c(t)$ and plot its power spectral density. This quantity is proportional to the sum $|S|^2 + |N|^2$, so we have

$$|S(f)|^2 + |N(f)|^2 \approx P_c(f) = |C(f)|^2 \quad 0 \leq f < f_c \text{ ----- (4.5g)}$$

The resulting plot (Figure 5) will often immediately show the spectral signature of a signal sticking up above a continuous noise spectrum. The noise spectrum may be flat, or tilted, or smoothly varying; it doesn't matter, as long as we can guess a reasonable hypothesis as to what it is. Draw a smooth curve through the noise spectrum, extrapolating it into the region dominated by the signal as well. Now draw a smooth curve through the signal plus noise power. The difference between these two curves is our smooth “model” of the signal power. The quotient of our model of signal power to our model of signal plus noise power is the optimal filter $\Phi(f)$. [Extend it to negative values of f by the formula $\Phi(-f) = \Phi(f)$.] Notice that $\Phi(f)$ will be close to unity where the noise is negligible, and close to zero where the noise is dominant. That is how it does its job! The intermediate dependence given by equation (4.5f) just turns out to be the optimal way of going in between the two extremes.

Because the optimal filter results from a minimization problem, the quality of the results obtained by optimal filtering differs from the true optimum by an amount that is second order in the precision to which the optimal filter is

determined. In other words, even a fairly crudely determined optimal filter (sloppy, say, at the 10 percent level) can give excellent results when it is applied to data. That is why the separation of the measured signal C into signal and noise components S and N can usefully be done “by eye” from a crude plot of power spectral density. All of this may give us thoughts about iterating the procedure we have just described. For example, after designing a filter with response $\Phi(f)$ and using it to make a respectable guess at the signal $\tilde{U}(f) = \Phi(f) C(f) / R(f)$, we might turn about and regard $\tilde{U}(f)$ as a fresh new signal which we could improve even further with the same literature technique.

4.6 Reconstructions of C_{56}^+ image by deconvolution methodology.

4.6a Deconvolution methodology with applying the Wiener filter on the noise-mixed convolved image

Deconvolution is a process which is used to reverse the effect of convolution for obtaining the image data. We performed the deconvolution procedures of images by using the 2D Fast Fourier Transform (FFT) and Inverse Fast Fourier Transform (IFFT). In the real experimental observation usually some noise is added to the convolved image. We need to check the trends of noise during deconvolution procedure because, deconvolution is very much noise-sensitive in the image data transformation. So, we have generated the 2D sample image in Figure 6(c) which is a convolution of two circles with their radii of 31 (Figure 6a) and 15 pixels (Figure 6b), respectively, in 128×128 data array. Then randomly scattered dots are added to simulate the noise. The ratio of the noise is 1.55% of the total intensity of the sample image. The noise mixed convoluted image is shown in Figure 6(d).

We performed the deconvolution methodology of Figure 6(d) by Figure 6(b) without any filter and recovered image is shown in Figure 6(e) which is

badly noise blurred. The recovered image using the Wiener filter [4] is shown in Figure 6(f) which is almost noise free. In Figures 6(e) and (f), the circles have the same diameter and line width as Figure 6(a) can be seen. It is obvious that the deconvolution methodology with applying the Wiener filter can satisfactory recover the original image.

4.6b Recovering the scattering distributions of C_{56}^+ image by using the deconvolution procedure with low pass filter

To reconstruct the scattering distributions of C_{56}^+ image, at first, we have simulated the 2D ion image of C_{56}^+ (convolved) and C_{60}^+ (the momentum distribution of the neutral C_{60} beam). To generate the C_{56}^+ image (Figure 7a) we have used the Maxwell-Boltzmann distribution function as well as both the first and the second step reactions with using constant KER equals 0.4 eV in the C_2 -loss process [2-8]. But in the case of C_{60}^+ image (Figure 7b), we considered the Maxwell-Boltzmann distribution function with zero KER in the first and second step reactions. We have also generated the expected image with considering only first and second step reaction part images which are shown in Figure 7(c). The image simulation conditions: TOF, 50×10^{-6} s; number of ions hitting at the surface of PSD, 8×10^5 ; temperature of the C_{60} molecular beam, 10K. Angular distribution is assumed to be isotropic and angles of ejection are selected randomly. We have performed the deconvolution methodology of Figure 7(a) by Figure 7(b) with using the low-pass filter. The recovered image (scattering distribution of C_{56}^+ image) is shown in Figure 7(d). The y-projections of Figures 7(a), (c), and (d) have been calculated and plotted in Figure 7(e). The filled circles (black) from Figure 7(a) have the highest intensity and the scattered curves (red) from Figure 7(d) have the lowest intensity. The filled stars (green) from Figure 7(c) have a less intensity than the filled circles. Here, it is concluded that the recovered image intensity (red curves) is very low rather than expected

image intensity (filled stars). So, we need to improve the technique before fitting the procedures in our actual experimental image data.

4.7 Conclusion

We have performed simulation for the image of the 3D velocity distributions of C_{56}^+ produced by dissociative photoionization of C_{60} . The arrival positions of C_{56}^+ ions, the spatial density functions, and the projections on the PSD have been calculated. The 2D cross-sectional images were derived from the projected images of C_{56}^+ ions produced through the stepwise C_2 - and C_4 -loss processes. At $T = 0$ K a marked difference in the image pattern could be seen between the two processes but it is almost smeared out under bulk conditions of C_{60} at 273 K due to the convolution of the thermal velocity of nascent parent C_{60}^+ ions. In contrast, a remarkable difference at $T = 0$ K were found to remain even at $T = 785$ K for the C_{56}^+ formation in the C_{60} beam, because the transverse velocity of the beam is extremely low. The difference in the image pattern between the two processes permits us to provide conclusive evidence on which process dominates photofragmentation of C_{60} in the extreme UV region. We therefore consider that the present VMI spectrometer will be available for future studies of the excited-state dynamics of fullerene ions. Experimentally the image of C_{56}^+ might be contaminated by the background dark counts due to impurities such as water, air, and organic compounds. We have tried to remove the background counts from the measured 2D image by means of deconvolution using the low-pass and Wiener filters.

References

- [1] H. Gabor, R. Hiss, H. G. Busmann, I. V. Hertel, *Z. Phys. D Atoms, Molecules and Clusters* 24, 307 (1992).
- [2] D. Muigg, G. Denifl, P. Scheier, K. Becker, and T. D. Märk, *J. Chem. Phys.* 108 (3), 963 (1998).
- [3] H. Katayanagi, C. Q. Huang, H. Yagi, B. P. Kafle, M. S. I. Prodhon, K. Nakajima and K. Mitsuke, *Rev. Sci. Instrum.* (2008) submitted.
- [4] A. J. R. Heck and D. W. Chandler, *Annu. Rev. Phys. Chem.*, 46 (1995) 335
- [5] A. T. J. B. Eppink and D. H. Parker, *Rev. Sci. Instrum.* 68 (9), 3477 (1997)
- [6] K. Mitsuke, H. Katayanagi, J. Kou, T. Mori, and Y. Kubozono, in *Ionization, Correlation, and Polarization in Atomic Collisions*, CP811, edited by A. Lahman-Bennani and B. Lohmann, American Institute of Physics, New York (2006)161-166.
- [7] B. P. Kafle, H. Katayanagi, and K. Mitsuke, in *Synchrotron Radiation Instrumentation*, CP879, edited by J. Y. Choi and S. Rah, American Institute of Physics, New York, 2007, 1809-1812.
- [8] K. Gluch, S. Matt-Leubner, O. Echt, B. Concina, P. Scheier, and T.D Märk, *J. Chem. Phys.* 121 (2004) 2137.
- [9] D. W. Chandler and P. L. Houston, *J. Chem. Phys.* 87 (1987) 1445-1447.
- [10] S. M. Candel et al. *Comput. Phys. Commun.* 23 (4) 343 (1981).
- [11] Smith LM. and Keefer D. R., Sudharsanan S. I., *J. Quant. Spectrosc. Radiat. Transfer* 39 (5), 367 (1988).
- [12] B. P. Kafle, H. Katayanagi, Md. Serajul. I. Prodhon, H. Yagi, C. Q. Huang and K. Mitsuke, *J. Phys. Soc. Jpn.* 77 (2008) 014302.
- [13] J. Kou, T. Mori, M. Ono, Y. Haruyama, Y. Kubozono and K. Mitsuke, *Chem. Phys. Lett.* 374 (2003) 1-6.

- [14] K. Mitsuke, H. Katayanagi, B. P. Kafle, C. Huang, H. Yagi, M. S. I. Proadhan and Y. Kubozono, J. Phys. Chem. A 111 (2007) 8336-8343.
- [15] T. Mori, J. Kou, M. Ono, Y. Haruyama, Y. Kubozono and K. Mitsuke, Rev. Sci. Instrum. 74 (2003) 3769-3773.
- [16] G. van Rossum and F. L. Drake, Python Reference Manual. (PythonLabs, Virginia, 2001)
- [17] Teach Yourself, C, 3rd Edition, Herbert Schild.

CITED REFERENCES for Wiener (Optimal) Filtering:

- Rabiner, L.R., and Gold, B. 1975, Theory and Application of Digital Signal Processing (Englewood Cliffs, NJ: Prentice-Hall).
- Nussbaumer, H.J. 1982, Fast Fourier Transform and Convolution Algorithms (New York: Springer-Verlag).
- Elliott, D.F., and Rao, K.R. 1982, Fast Transforms: Algorithms, Analyses, Applications (New York: Academic Press).

Figures of chapter 4

Assumptions in the scattering distributions program

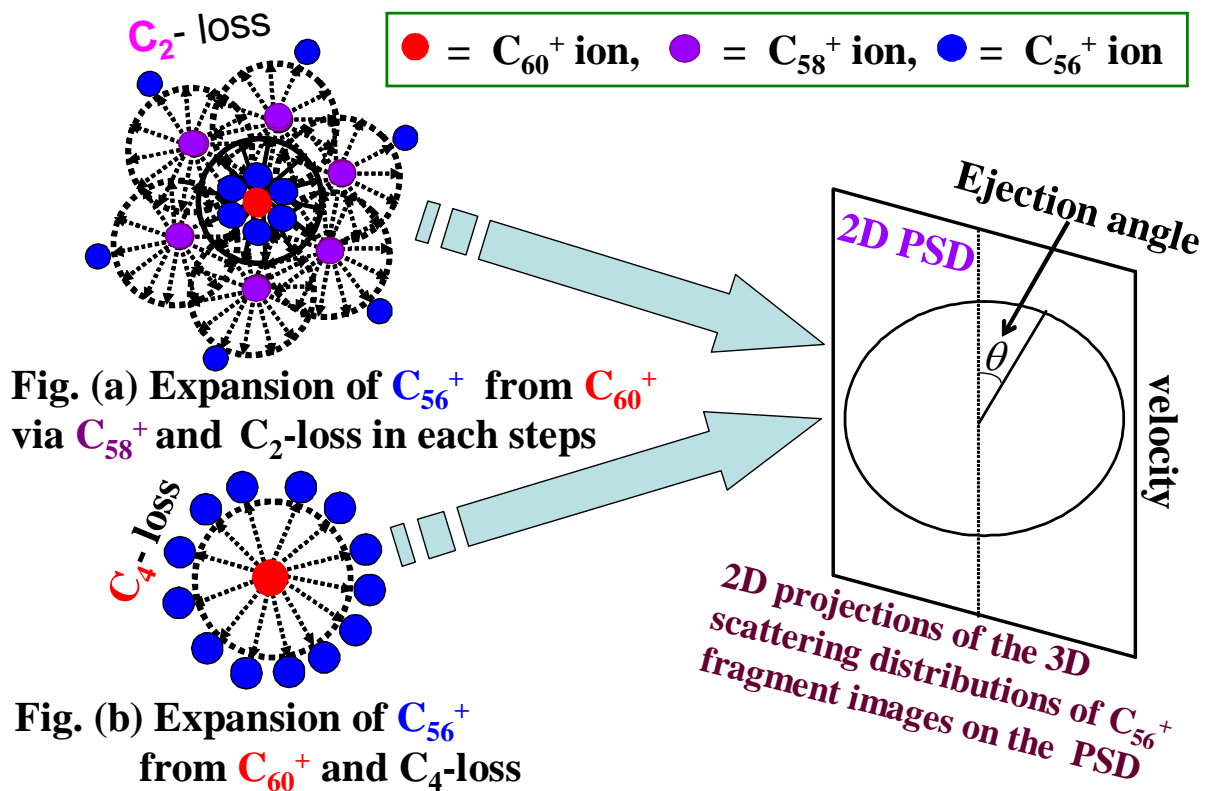


Figure 1

Figures (a) and (b) are the expansion of C_{56}^+ from parent C_{60}^+ ions in the C_2^- - and C_4^- loss processes, respectively.

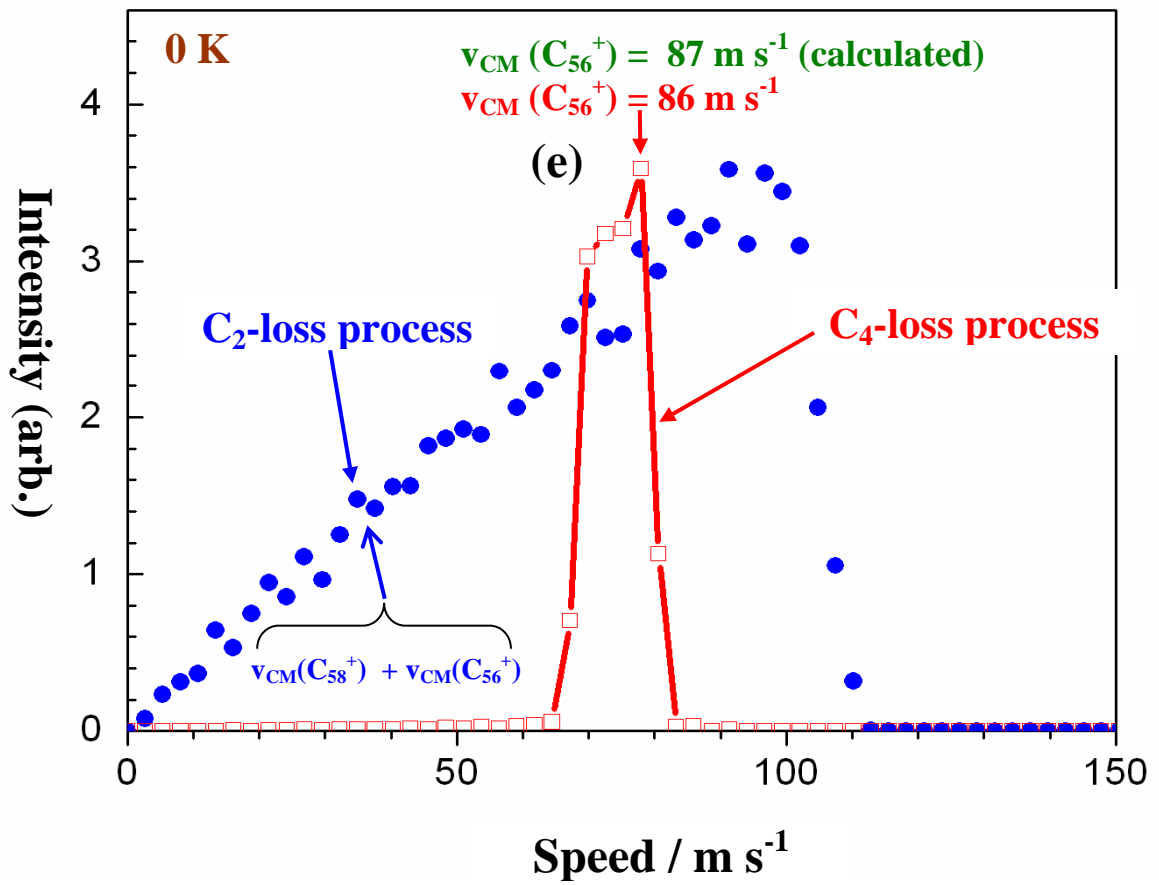
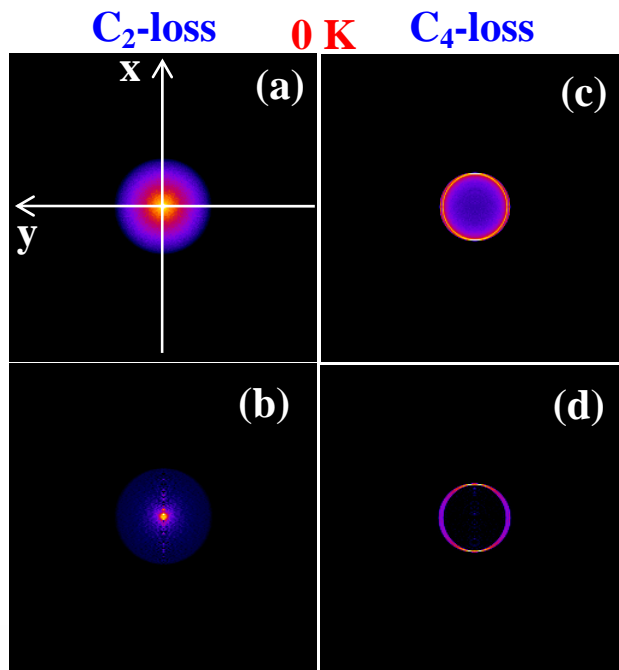
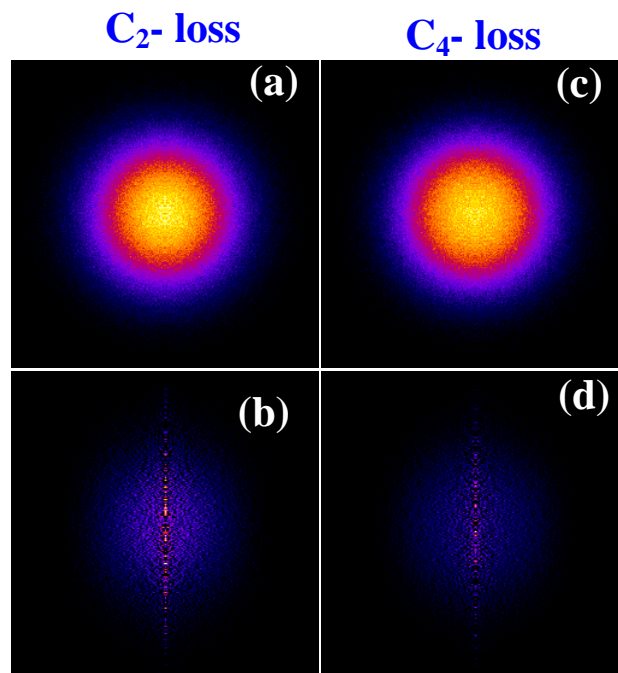


Figure 2

Panels (a) and (c) simulated 2D images of C_{56}^+ fragments projected on the PSD in the C_2 - and C_4 -loss processes at $T = 0$ K. Panels (b) and (d) the cross-sectional images of the 3D velocity distributions in the perpendicular plane of the spectrometer obtained by IAT from Panels (a) and (c), respectively. (e) Speed distributions extracted from the Panels (b) and (d). The filled circles are based on C_2 -loss process which is much broader than the solid curves in the C_4 -loss process.



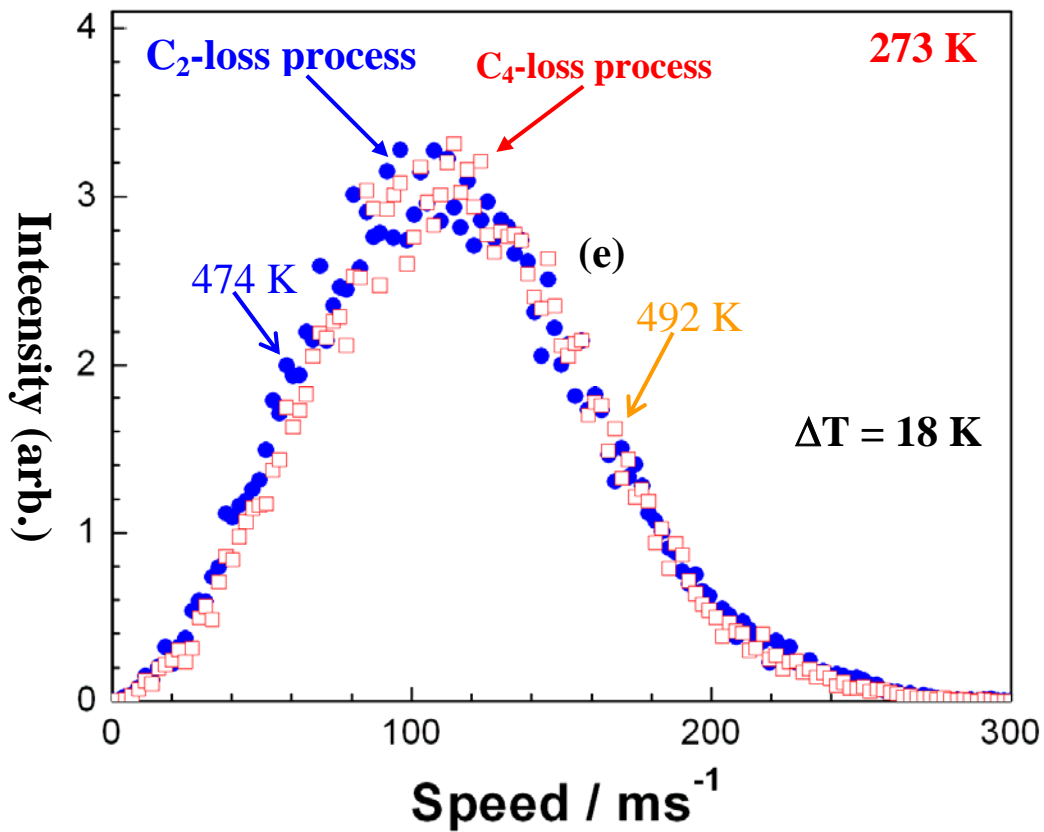


Figure 3

In the insets, Panels (a) and (c) simulated 2D images of C_{56}^+ fragments from C_{60} in the C_2 - and C_4 -loss processes at $T = 273$ K. Panels (b) and (d) the cross-sectional images obtained from Panels (a) and (c), respectively. (e) Speed distributions extracted from Panels (b) and (d), respectively. The filled circles and the solid curves are related to the C_2 - and for C_4 -loss processes, respectively have almost the same shape.

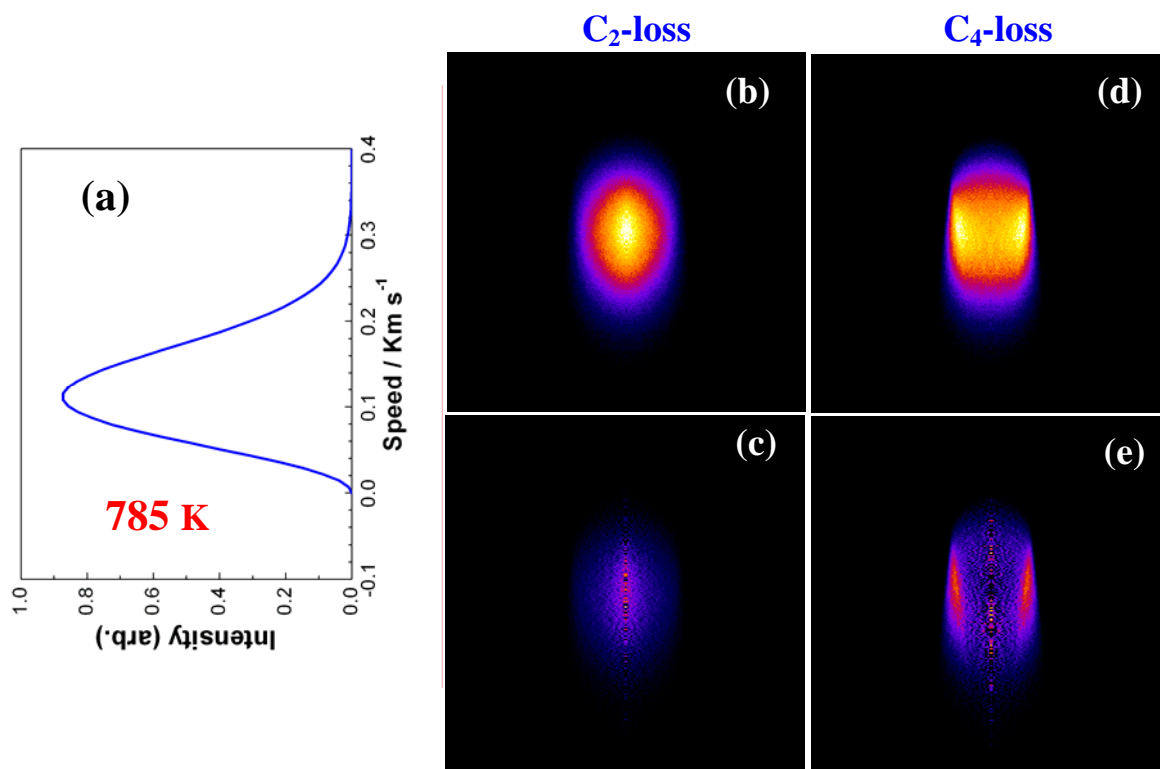


Figure 4

(a) Maxwell-Boltzmann speed distribution at $T = 785$ K used in the simulations for the effusive beam of parent C_{60} molecules. Panels (b) and (d) are simulated 2D images of C_{56}^+ fragments projected on the PSD in two processes and Panels (c) and (e) are cross-sectional images of the 3D velocity distributions in the x-y plane. A remarkable difference is observed between the intensity distributions of the two images.

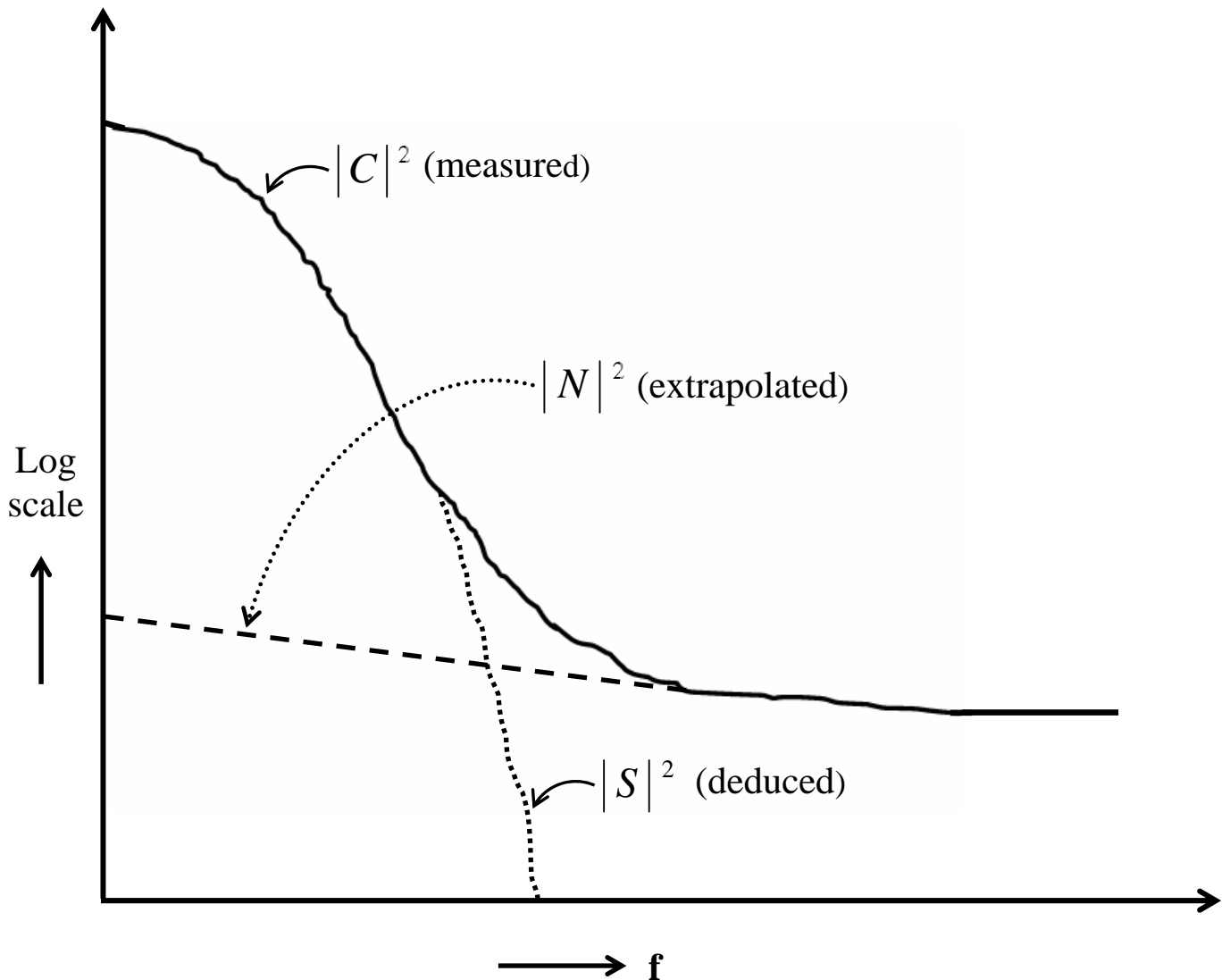


Figure 5

Optimal (Wiener) filtering. The power spectrum of signal plus noise shows a signal peak added to a noise tail. The tail is extrapolated back into the signal region as a “noise model.” Subtracting gives the “signal model.” The models need not be accurate for the method to be useful. A simple algebraic combination of the models gives the optimal filter.

Generating the 2D noised-mixed sample image in 128×128 data array and recovered image without and with using the Wiener filter

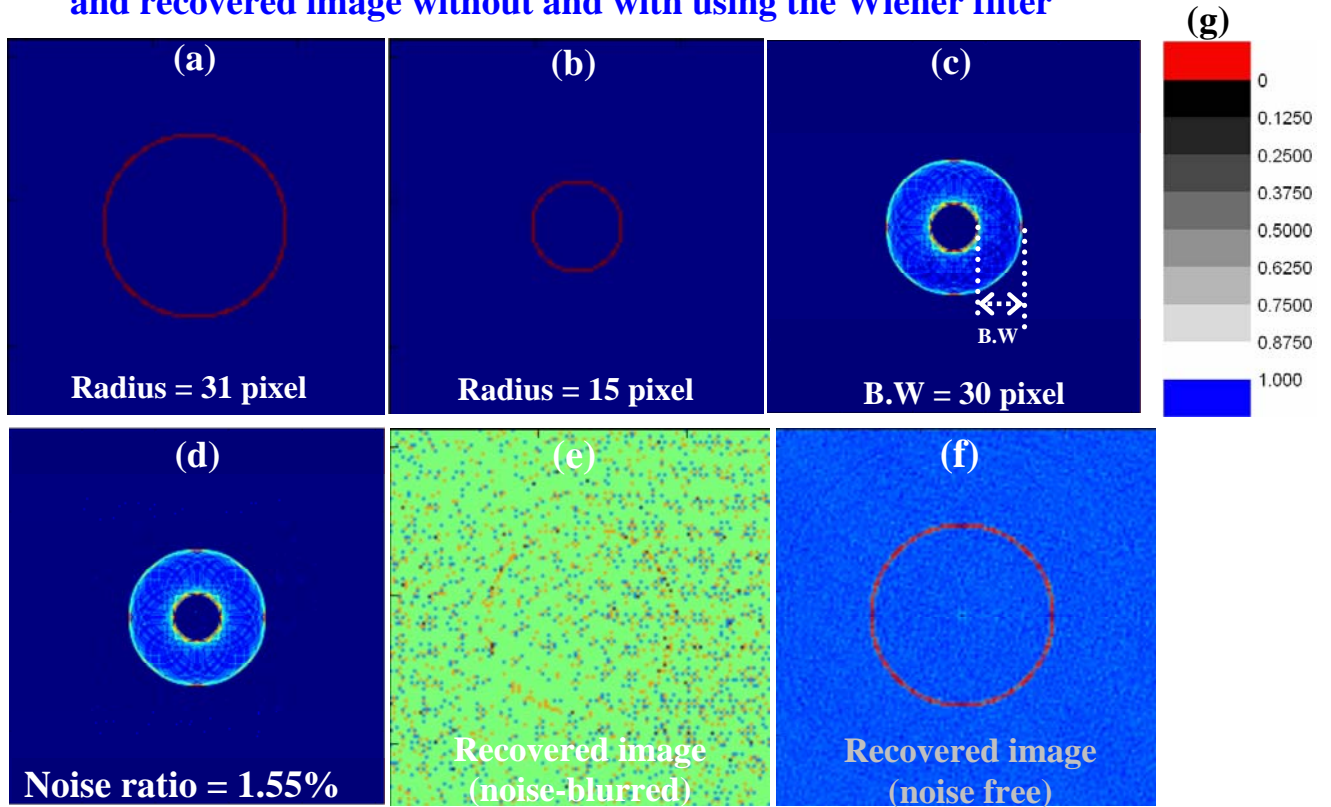


Figure 6

Panels (a) and (b) 2D original images (circles with radii 31 and 15 pixels, respectively); Panel (c) Convolved image with blurred width of 30 pixels; Panel (d) Noise-mixed convolved image (noise ratio, 1.55%); Panel (e) Recovered image without any filter (noise-blurred); Panel (f) Recovered image with Wiener filter (noise-free); (g) Image scale; Array and image size (both): 128×128 pixels.

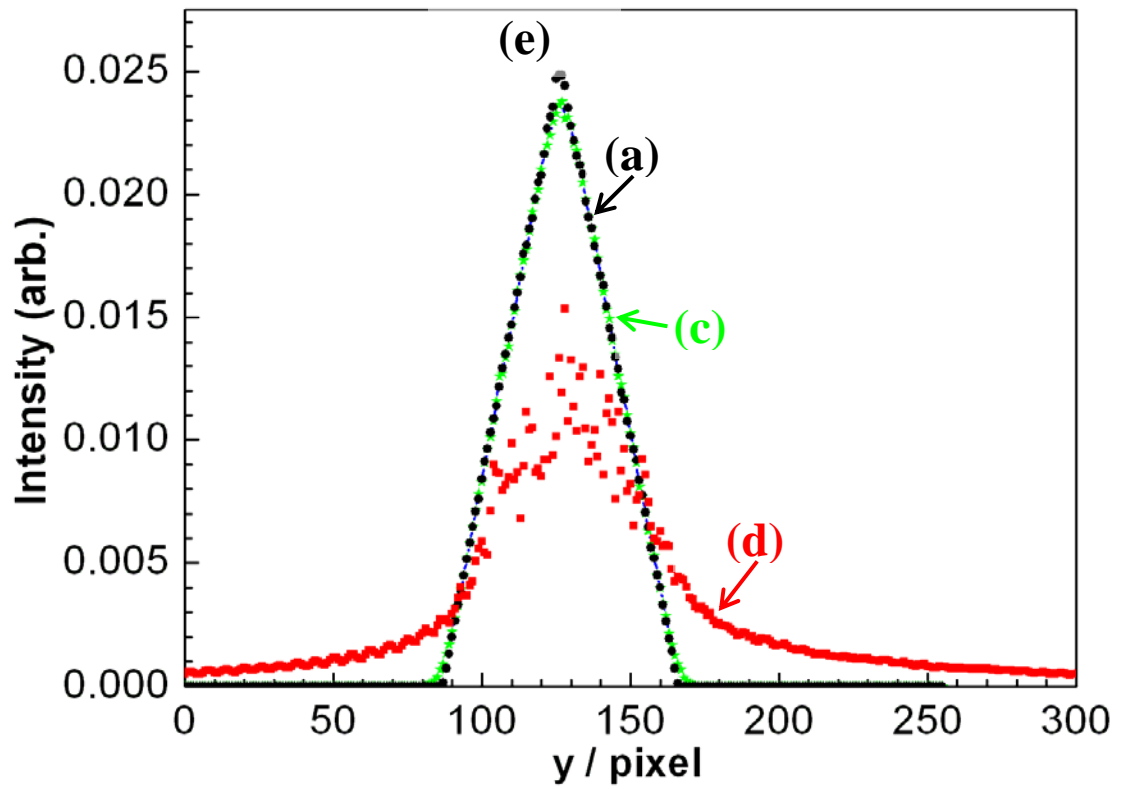
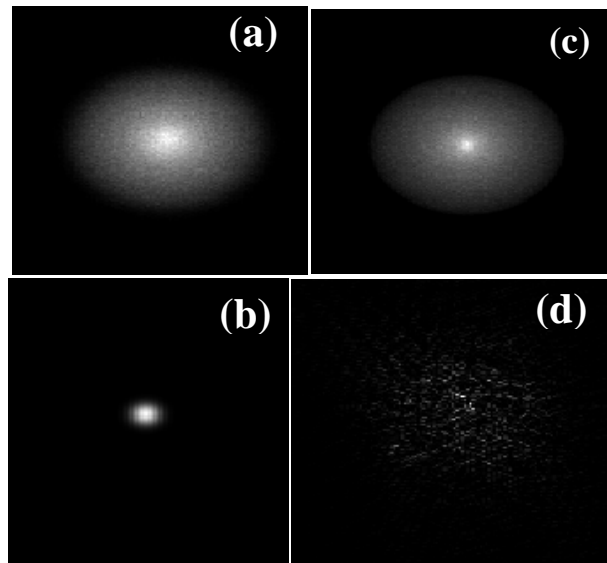


Figure 7

In the insets, Panel (a) shows a convolved image of C_{56}^+ , Panel (b) C_{60}^+ image (the momentum distribution of the neutral C_{60} beam), Panel (c) expected image, Panel (d) deconvolved image (recovered image), and Figure (e) compared curves extracted from the Panels (a), (c), and (d).

Chapter 5

Summary of the Thesis

In my Ph. D dissertation, two major topics have been bestowed specifically as (i) construction of a VMI spectrometer with investigation of its fundamental performance for achieving the high kinetic energy (KE) resolution on the photofragment images of fullerenes as well as (ii) simulation studies of C_{60} fragmentations. It is known that there are two possible photofragmentation processes of C_{60} , namely the stepwise C_2 -loss and direct fission with C_4 -loss. Several groups have tried to distinguish these two processes by measuring the total average KE release in the decomposition of C_{60} into C_{56}^+ and smaller fragments [1-3]. Such efforts, however, have met with failure. The portion of the kinetic energy release partitioned to the fragments was found to be a few tens of millielectronvolts, and is comparable to or smaller than the average thermal energies of neutral C_{60} molecules in an effusive beam. The two processes therefore give C_{56}^+ fragments with similar average kinetic energies in the laboratory frame. Obviously we must observe a precise 3D velocity distribution, speed and angular distributions, to gain helpful clue to decide on which of the C_2 - and C_4 -loss processes is more dominant. For this purpose we should develop a VMI spectrometer which is very sensitive to thermal ions with small translational energies.

We have developed the VMI spectrometer based on a time-of-flight (TOF) technique for fragment ions with thermal energies produced by irradiation of synchrotron radiation [4,5]. The basic performance of this VMI spectrometer has been tested by using five rare gases (i.e. He, Ne, Ar, Kr, and Xe) in the photon energy of $h\nu = 35$ eV at 300 K. The 3D velocity distributions were reconstructed by using the inverse Abel transformation (IAT) [6-8] from the measured 2D images projected on a PSD to the cross-sectional images in the

perpendicular plane of the spectrometer [9]. Using the speed distributions extracted from these cross-sectional images, we have evaluated the temperatures by the least-squares fit of the data points to the Maxwell-Boltzmann distribution. The best fitted curves of the lighter three rare gases (He, Ne and Ar) are in reasonable agreements with the Maxwell-Boltzmann distributions at the temperature $T = 300$ K. The temperatures obtained by the fittings are 282, 272 and 295 K for He, Ne and Ar, respectively. Small deviations from the expected value of 300 K can be accounted for by systematic errors peculiar to the numerical image processing in the IAT. For Kr and Xe the agreement is much worse mainly due to smaller signal-to-background ratios. Furthermore, the best fitted curve of Xe appears to shift by 60 K in the direction of lower speed as compared to the expected distribution at 300 K. This shift can be explained as that the raw image of Xe includes not only Xe^+ but also Xe^{2+} signal counts [5].

We have simulated the images of five rare gases at 300 K to compare with the experimentally obtained images. From the simulated projections on the PSD we have obtained the cross-sectional images and speed distributions. The temperature of He is evaluated to be 287 K from the least-squares fit of the data points of the simulated speed distribution to the Maxwell-Boltzmann distribution. Similar simulations were executed for Ne and Ar. All the temperatures were found to be in good agreement with those from the experimental images.

Moreover, a close inspection of the simulated images revealed that the defocusing effect due to a definite ionization volume can be well reproduced by introducing two Gaussian functions as (a) $2\sigma_x = 0.2$ and $2\sigma_y = 2.8$ mm in devoid of oven with thickness monitor inside the experimental vacuum chamber, (b) $2\sigma_x = 1.7$ and $2\sigma_y = 3.2$ mm when oven with thickness monitor was installed.

From the study of defocusing parameters and speed distributions of rare gases momentous features of our present VMI spectrometer having come to the front is its high sensitivity to thermal ions with relatively small translational energies and high velocity resolution realized by the PSD. These features were helpful in our achieving the 3D velocity distribution of the photoions from the rare gas ions at room temperature. It should also be noted that we have succeeded in determining the speed and angular distributions of C_{60}^{z+} ($z = 1, 2$) produced from C_{60} molecular beams by using the same experimental setup [5]. The simulation for the image of scattering distributions of C_{56}^+ produced through the C_{2-} and C_{4-} loss processes was performed to discuss the feasibility of the VMI experiments of C_{60} beams. We simulated the arrival positions of C_{56}^+ ions, the spatial density functions, and the calculated projections on the PSD. The 2D cross-sectional images were calculated from the projected images of C_{56}^+ ions produced through the stepwise C_{2-} loss and C_{4-} loss processes. At temperature of $T = 0$ K a marked difference in the image pattern could be seen between the two processes but it is almost smeared out under bulk conditions of C_{60} at $T = 273$ K owing to the convolution of the thermal velocity of nascent parent C_{60}^+ ions. In contrast, a remarkable difference at $T = 0$ K were found to remain even at $T = 785$ K for the C_{56}^+ in the C_{60} beam, because the transverse velocity of the beam is extremely low. The difference in the image pattern between the two processes permits us to provide conclusive evidence on which process dominates photofragmentation of C_{60} in the extreme UV region. We therefore consider that the present VMI spectrometer will be available for future studies of the excited-state dynamics of fullerene ions. Experimentally the image of C_{56}^+ ions dissociated from the parent C_{60}^+ ions might be contaminated by the background dark counts of the PSD due to impurities such as water, air, and organic compounds. We have tried to remove the background counts from the measured 2D image by means of deconvolution using the low-pass and Wiener filters.

References

- [1] K. Gluch, S. Matt-Leubner, O. Echt, B. Concina, P. Scheier, and T.D Märk, J. Chem. Phys. 121 (2004) 2137-2143.
- [2] H. Gaber. R. Hiss, H. G. Busmann, and I. V. Hertel, Z. Phys. D – Atoms, Molecules and Clusters 24 (1992) 307-309.
- [3] D. Muigg, G. Denifl, P. Scheier, K. Becker, and T. D. Märk, J. Chem. Phys. 108 (1998) 963-970.
- [4] B. P. Kafle, H. Katayanagi, and K. Mitsuke, in Synchrotron Radiation Instrumentation, CP879, edited by J. Y. Choi and S. Rah, American Institute of Physics, New York, 2007, 1809-1812.
- [5] H. Katayanagi, C. Q. Huang, H. Yagi, B. P. Kafle, M. S. I. Prodhan, K. Nakajima and K. Mitsuke, Rev Sci. Instrum. (2008) submitted.
- [6] D. W. Chandler and P. L. Houston, J. Chem. Phys. 87 (1987) 1445-1447.
- [7] S. M. Candel et al. Comput. Phys. Commun. 23 (4) 343 (1981).
- [8] Smith LM. and Keefer D. R., Sudharsanan S. I., J. Quant. Spectrosc. Radiat. Transfer 39 (5), 367 (1988).
- [9] A. T. J. B. Eppink and D. H. Parker, Rev. Sci. Instrum. 68 (9), 3477 (1997)

Future Prospect

Additional electrodes between the repeller and extractor will be very effective at decreasing σ_y and suppressing deformation of the projected images. These electrodes are also beneficial to the VMI experiments of fullerenes because we can reduce distortion of the electric field caused by sample cell and thickness monitor (see Figure 2.3b of chapter 2). The kinetic energy released in each fragmentation step of C_2^- and C_4^- -loss processes may have a broad distribution around 0.4 eV. This effect will blur experimental C_{56}^+ images to some extent. Nevertheless, the remarkable difference in the image pattern at $T = 785$ K proves the images of the 3D velocity distributions are very sensitive to the fragmentation processes. We therefore consider the present VMI spectrometer will be available for future studies of the excited-state dynamics of fullerene ions.

Appendixes

Appendix-1

Metropolis-Hasting algorithm

In mathematics and physics, the Metropolis-Hasting algorithm is a rejection sampling algorithm used to generate a sequence of samples from a probability distribution that is difficult to directly sample from. This sequence can be used in Markov chain Monte Carlo to approximate the distribution (as with a histogram), or to compute an integral (such as expected value). The algorithm was named in reference of Nicholas Metropolis, who published it in 1953 for the specific case of the Boltzmann distribution, and W. K. Hastings, who generalized it in 1970.

The Metropolis-Hastings algorithm can draw samples from any probability distribution $p(x)$, requiring only that the density can be calculated at x . The algorithm generates a Markov chain in which each state x^t depends only on the previous state x^{t-1} . The algorithm uses a proposal density $Q(x'; x^t)$, which depends on the current state x^t , to generate a new proposed sample x' . This proposal is 'accepted' as the next value ($x^{t+1} = x'$) if u drawn from $U(0, 1)$ is

$$u < \frac{P(x')Q(x^t|x')}{P(x^t)Q(x'|x^t)}$$

otherwise the current value is retained:

$$x^{t+1} = x^t.$$

For example, the proposal density could be a Gaussian function centred on the current state x^t

$$Q(x'; \mathcal{X}^t) \sim N(\mathcal{X}^t, \sigma^2 I)$$

reading $Q(x'; \mathcal{X}^t)$ as the probability density function for x' given the previous value \mathcal{X}^t . This proposal density would generate samples centred around the current state with variance $\sigma^2 I$. The original Metropolis algorithm calls for the proposal density to be symmetric ($Q(x; y) = Q(y; x)$); generalization by Hastings lifts this restriction. It is allowed for $Q(x'; \mathcal{X}^t)$ not to depend on x' at all, in which case the algorithm is called “Independence Chain Metropolis-Hastings” (as opposed to “Random Walk Metropolis-Hastings”). Independence chain M-H algorithm with suitable proposal density function can offer higher accuracy than random walk version, but it requires some a priori knowledge of the distribution.

Now, we draw a new proposal state x' with probability $Q(x'; \mathcal{X}^t)$ and then calculate a value

$$a = a_1 a_2$$

where

$$a_1 = \frac{P(x')}{P(\mathcal{X}^t)}$$

is the likelihood ratio between the proposed sample x' and the previous sample \mathcal{X}^t , and

$$a_2 = \frac{Q(\mathcal{X}^t; x')}{Q(x'; \mathcal{X}^t)}$$

is the ratio of the proposal density in two directions (from x^t to x' and vice-versa). This is equal to 1 if the proposal density is symmetric. Then the new state x^{t+1} is chosen with the rule

$$x^{t+1} = \begin{cases} x' & \text{if } a > 1 \\ x' \text{ with probability } a, & \text{if } a < 1 \end{cases}$$

The Markov chain is started from a random initial value x^0 and the algorithm is run for many iterations until this initial state is “forgotten”. These samples, which are discarded, are known as burn-in. The algorithm works best if the proposal density matches the shape of the target distribution $p(x)$, that is $Q(x'; x^t) \approx p(x')$, but in most cases this is to unknown. If a Gaussian proposal is used the variance parameter σ^2 has to be tuned during the burn-in period. This is usually done by calculating the acceptance rate, which is the fraction of proposed samples that is accepted in a window of the last N samples. This is usually set to be around 60%. If the proposal steps are too small the chain will mix slowly (i.e., it will move around the space slowly and coverge slowly to $p(x)$). If the proposal steps are too large the acceptance rate will be very low because the proposals are likely to land in regions of much lower probability density so a1 will be very small.

Appendix-2

(a) Inverse Abel Transformation (IAT)

L. Montgomery et al. *J. Quant. Spectrosc. Radial.*

Transfer Vol. 39, No. 5, pp. 367-373, 1988

The reconstruction of a circularly symmetric two-dimensional function from its projection onto an axis is known as Abel inversion or inverse Abel transformation of the projection. The measured intensity, $I(x)$, is given in terms of emission coefficients, $\varepsilon(r)$, through the Abel transform [1].

$$I(x) = 2 \int_x^\infty \frac{r \varepsilon(r) dr}{\sqrt{r^2 - x^2}}, \text{----- (2a)}$$

where x is the displacement of the intensity profile and r is the radial distance in the source. The measured intensity $I(x)$ is the one-dimensional projection of the two-dimensional, circularly symmetric function having $\varepsilon(r)$ as a radial slice. The inversion integral, or the inverse Abel transform, is given by

$$\varepsilon(r) = -\frac{1}{\pi} \int_r^\infty \frac{(dI/dx)}{\sqrt{x^2 - r^2}} dx \text{----- (2b)}$$

In practice, application of Equation 2(b) is made difficult because of the singularity in the integral at the lower limit and because the derivative of the projection tends to enhance greatly the noise-corrupting of the data. Furthermore, the intensity is usually not available as a continuous function and so is known only at discrete sample points. Several approaches, based upon geometrical techniques or numerical methods and using polynomial fits, have been employed to perform the inversion. Nestor and Olsen [2] transformed the variables according to $r^2 = v$ and $x^2 = u$ so that the inversion integral can be

approximated by a simpler sum. Bockasten [3] fitted third-degree polynomials to the data points and approximated the integral by a sum. However, these methods require prior smoothing of the data and are not considered complete in themselves.

Later, least-square curve-fitting methods were employed and were found to yield better results than the exact fit methods when applied to noisy data. Freeman and Katz [4] used a single polynomial curve to fit the data. Fourth-order polynomials were found to give the best results among trials using up to twelfth-order polynomials. Cremers and Birkebak [5] compared several inversion techniques and showed that the least-squares curve fitting techniques were more favorable than the exact fit methods. Short descriptions of several other techniques and comparisons of these various techniques can be found in Ref. 5. Shelby [6] divided the data into several intervals and used a least-square polynomial fit technique in each interval to smooth the scattered data. The inversion was then performed analytically and summed over the intervals to obtain emission coefficients. Malonado et al. [7] expanded $\varepsilon(r)$ in a series of orthogonal polynomials and derived a method to find the expansion coefficient from the intensity data.

All of these methods have drawbacks. The singularity in the lower limit of the integral causes problems for the numerical methods, but these are avoided by using the analytical methods. The smoothing techniques used are essentially a kind of low-pass filtering having undetermined filter characteristics. When the inversion is performed, the spectral characteristics of the noise, of the desired signal and of the smoothing algorithm are not considered. Therefore, the possible problems of loss of information and distortion are neglected. Use of the Abel integral implies an assumption that the input data will be symmetric, but the measured intensity data often exhibit some degree of asymmetry, and the exact axis of symmetry is not usually known a priori. Determination of the axis of symmetry is often chosen using ad hoc methods. The smoothing techniques

consume a large amount of computer time and the error-propagation calculations are tedious [6].

We present method a method based on integral transforms that removes many of the difficulties and uncertainties associated with these earlier techniques and, by using the fast Fourier transform (FFT) algorithm to implement the procedure, greatly reduces the computation time. This technique is substantially different from earlier methods in the use of transform techniques and frequency-domain analysis. Several principles of digital signal processing and spectral analysis are employed to solve the problems associated with the processing of actual, noise-corrupted, asymmetric data. In the following paragraph, the Abel inversion integral is reformulated in term of the Fourier and Hankel transform.

Reformulation of the Abel inversion:

The mathematical basis for the Abel inversion technique presented here is the reformulation of the Abel transform equations (2a) and (2b) in terms of the Fourier and Hankel integral transforms. This formulation is discussed in Bracewell [8] and can also be derived as a special case of the projection-slice theorem, a fundamental relation in the field of computed tomography. For completeness, a brief derivation is presented here.

If the substitution $r = \sqrt{x^2 + y^2}$ is made in equation (2a), the projection can be written

$$I(x) = \int_{-\infty}^{\infty} \varepsilon(\sqrt{x^2 + y^2}) dy \text{ ----- (2c)}$$

The one-dimensional Fourier transform of equation (2c) is

$$F\{I(x)\} = \int_{-\infty}^{\infty} \int_{-\infty}^{\infty} \varepsilon(\sqrt{x^2 + y^2}) \exp(-i2\pi xq) dx dy \text{ ----- (2d)}$$

If the variable of the integration are now changed from Cartesian to polar coordinates, it can be shown that

$$F \{ I(x) \} = 2\pi \int_0^\infty r \varepsilon(r) J_0(2\pi r q) dr \text{ ----- (2e)}$$

where $J_0(\cdot)$ is the zero-order Bessel function of the first kind. The right-hand side of the equation (2e) is the zero-order Hankel transform of $\varepsilon(r)$, whose inverse transform is identical in form to the forward transform. The emission distribution of the plasma can thus be recovered by taking the inverse Hankel transform of the Fourier transform of the projected intensity as follows:

$$\varepsilon(r) = 2\pi \int_0^\infty q J_0(2\pi r q) \int_{-\infty}^\infty I(x) \exp(-i2\pi x q) dx dq \text{ ---- (2f)}$$

From a computational point of view, the inversion formula given in equation (2f) has several advantages over the Abel inversion integral of equation (2b). First, we avoid the difficulty associated with the singularity at the lower limit of integration. Second, following the Fourier transform of $I(x)$, filters may be applied directly in the frequency domain to reduce the noise and thus smooth the data in a known, systematic manner. Finally, equation (2f) can be numerically approximated with discrete fast transform algorithms available in software or vector-array processing hardware to decrease computation time over techniques used previously.

Equation (2f) shows an important property of the transform-based formulation of the Abel inversion. If $I(x)$ is an error-free projection of a real radially symmetric function that has an axis of symmetry that projects onto the origin of the x-coordinate axis, as was implicitly assumed in the derivation, then $I(x)$ is real and even. Its Fourier transform is thus also real and even, and so the inverse Hankel transform yields a real $\varepsilon(r)$. If, however, the projection is such that the axis of the symmetry is shifted from the x-axis origin and corrupted with some uncertainty called noise, as is the case in any experimental data-acquisition system, then the resulting inversion will have an imaginary component, which is a physical impossibility. It is thus necessary to process any experimentally-acquired data in such a manner so as to ensure that it is

symmetric about the x-axis origin when employing equation (2f) to perform the Abel inversion. This procedure involves determining the axis of symmetry in the presence of noise and eliminating the odd component of the noise from the data.

The computational technique employed for equation (2f) was to use a fast Fourier transform algorithm to approximate the inner integral by rectangular rule integration. The inverse Hankel transform was then performed by the method of Candel, [9] modified by S. I. Sudharsanan [10] to increase computational efficiency further by eliminating redundant additions in the algorithm. Numerical experience has been shown that this method is quite fast, and results in close agreement between known closed-form Abel inversions and numerically calculated inverted functions.

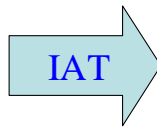
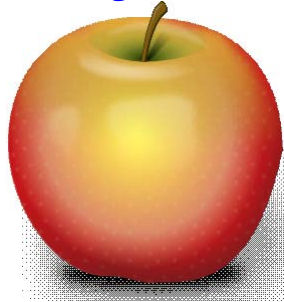
References

- [1] H. R. Griem, *Plasma Spectroscopy*, McGraw-Hill, New York, NY (1964).
- [2] O. H. Nestor and H. N. Olsen, *SIAM Rev.* 22 (1960) 200.
- [3] K. Bockasten, *JOSA* 51, (1961) 943.
- [4] M. J. Freemann and D. Katz, *JOSA* 53 (1963) 1172
- [5] C. J. Cremers and R. C. Barkibak, *Appl. Opt.* 5 (1966) 1057
- [6] R. T. Shelby, Masters thesis, Department of Mathematics, University of Tennessee, Knoxville, TN (1976)
- [7] C. D. Maldonado, A. P. Caron, and H. N. Olsen, *JOSA* 55 (1965) 1247
- [8] R. N. Bracewell, *The Fourier Transform and Its Application*, McGraw-Hill, New York, NY (1965).
- [6] S. M. Candel, *Comp. Phys. Commun.* 23 (1981) 343.
- [10] S. I. Sudharsanan, Masters Thesis, Department of Electrical Engineering, University of Tennessee, Knoxville, TN (1986).

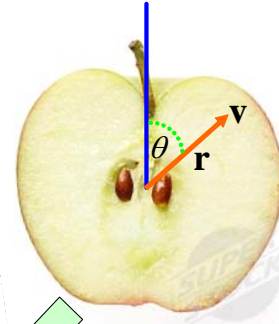
(b)

Basic concept of the Inverse Abel Transform (IAT)

(a) Projected 2D image at PSD



(b) 2D cross-sectional image



$$r \propto \left\{ \begin{array}{l} v \\ KE^{\frac{1}{2}} \end{array} \right\} \times \text{TOF}_{\text{ion}}$$

- (i) Radial distributions.
- (ii) Velocity distributions (i.e. speed and angular distributions).
- (iii) Center-of-mass KE release.

θ = Angle of ejection,
 v = Speed (velocity magnitude),
 r = Radial distance.

Appendix-3

Maxwell-Boltzmann distribution function

The relevant microscopic information is not knowledge of the position and velocity of every molecule at every instant of time, but just the distribution function, that is to say, what percentage of the molecules are in the certain part of the container, and what percentage have velocities within a certain range, at each instant of time. For a gas in thermal equilibrium, the distribution function is independent of time. Ignoring tiny corrections for gravity, the gas will be distributed uniformly in the container, so the only unknown is the velocity distribution function.

We would like to extend the arguments which led to the one-dimensional (1D) Maxwell distribution to three dimensions (3D). We need to determine the probability that the particles have components of velocity in the narrow range v_x to $v_x + dv_x$, v_y to $v_y + dv_y$, and v_z to $v_z + dv_z$. We know the answer for each direction independently. Now, because of the randomizing effects of the collision, these distributions are statistically independent and so the joint probability of find the particle with velocity in the range v_x to $v_x + dv_x$, v_y to $v_y + dv_y$, and v_z to $v_z + dv_z$ is

$$\begin{aligned} f(v_x, v_y, v_z) dv_x dv_y dv_z &= f_1(v_x) f_1(v_y) f_1(v_z) dv_x dv_y dv_z \\ &\propto \exp(-mv_x^2 / 2KT) dv_x \\ &\times \exp(-mv_y^2 / 2KT) dv_y \\ &\times \exp(-mv_z^2 / 2KT) dv_z \text{ ----- (3a)} \end{aligned}$$

$$= \exp[-m(v_x^2 + v_y^2 + v_z^2) / 2KT] dv_x dv_y dv_z \text{ ----- (3b)}$$

Therefore,

$$f(v) dv_x dv_y dv_z \propto \exp(-mv^2 / 2KT) dv_x dv_y dv_z \text{ ----- (3c)}$$

since $v^2 = v_x^2 + v_y^2 + v_z^2$. The combination $dv_x dv_y dv_z$ defines an element of volume in velocity space.

We have only one final step to determine the complete one- and three-dimensional probability distributions. We need to ensure that the total probability of finding the particle with some velocity in one or three dimensions is unity. Taking the one-dimensional distribution first, this means that

$$\int_{-\infty}^{\infty} df_1(v_x) = A \int_{-\infty}^{\infty} \exp(-mv_x^2/2KT) dv_x = 1 \text{ ----- (3d)}$$

To find the normalisation constant A, we use the standard integral

$$\int_{-\infty}^{\infty} e^{-x^2} dx = \sqrt{\pi}.$$

We require

$$A \int_{-\infty}^{\infty} e^{-mv_x^2/2KT} dv_x = 1$$

We transform the integral to standard form by substituting

$$x = v_x \sqrt{m/2KT}.$$

Then, remembering to substitute for the dv_x as well, we obtain

$$A (2kT/m) \int_{-\infty}^{\infty} e^{-x^2} dx = 1, \text{ and solving gives}$$

$$A = \sqrt{m/2\pi KT}.$$

Hence, the one-dimensional velocity distribution function is as follows:

$$f_1(v_x) = \sqrt{m/2\pi KT} e^{-mv_x^2/2KT} \text{ ----- (3e)}$$

and obviously,

$$f_1(v_x) dv_x = \sqrt{m/2\pi KT} e^{-mv_x^2/2KT} dv_x \text{ ----- (3f)}$$

The expression (3e) is called the Maxwell distribution of one-component velocity and is shown in Figure 3(i) using He sample at 300 K. The equation (3f) is known as the one-dimensional Maxwell distribution

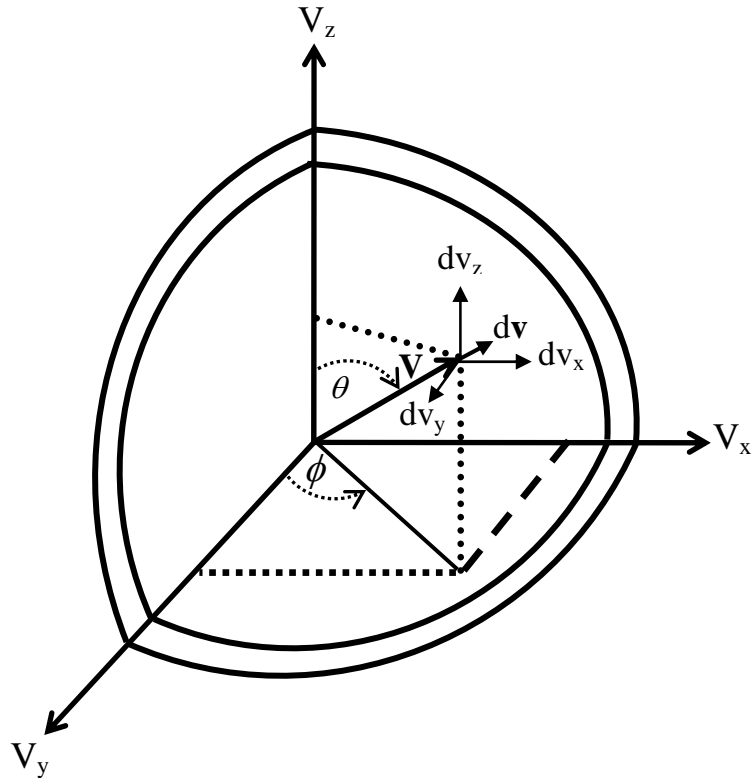


Figure 3 Summing over all the vectors with magnitude v to $v + dv$.

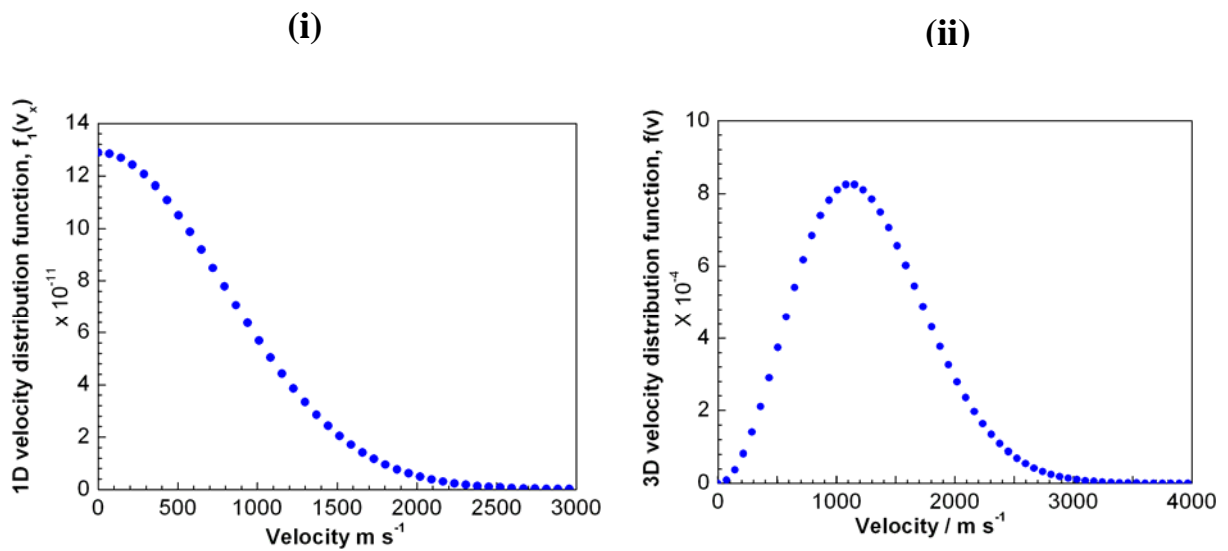


Figure 3 (i) 1D Maxwell-Boltzmann velocity distributions, and
(ii) 3D Maxwell-Boltzmann velocity distributions.

We have argued that the answer should only depend on the speed and so, to complete our analysis, we need to re-write our result for the normalised three-dimensional velocity distribution in terms of speed v alone.

$$f(v) dv_x dv_y dv_z = \left(\frac{m}{2\pi KT}\right)^{3/2} e^{-mv^2/2KT} dv_x dv_y dv_z \text{ ----- (3g)}$$

To find the distribution function in terms of v we note that there are many different combinations of velocity which give the same speed v . In the language of statistical physics, there is a degeneracy $g(v) dv$. To find the probability of a given speed irrespective of the direction of the velocity, we must sum the volumes $dv_x dv_y dv_z$ in velocity space which all have the same speed; these form the region of velocity space in a narrow spherical shell between v and $v + dv$ where $v^2 = v_x^2 + v_y^2 + v_z^2$ -one octant of this spherical shell is shown in Figure 3. The complete shell has a volume $4\pi v^2 dv$ and so the corresponding distribution function is $f_1(v_x) f_1(v_y) f_1(v_z) 4\pi v^2 dv$. Therefore,

$$f(v) dv = \left(\frac{m}{2\pi KT}\right)^{3/2} 4\pi v^2 e^{-mv^2/2KT} dv \text{ ----- (3h)}$$

$$= \left(\frac{m}{2\pi KT}\right)^{3/2} e^{-mv^2/2KT} 4\pi v^2 dv \text{ ----- (3i)}$$

$\underbrace{\hspace{10em}}_{\text{Normalisation Constant}} \quad \underbrace{\hspace{10em}}_{\text{Boltzmann factor}} \quad \underbrace{\hspace{10em}}_{\text{Volume of velocity space}}$

The expression of Equation (3h) is Maxwell-Boltzmann distribution for the speeds of the particles and shown in Figure 3(ii) by using the He sample at 300 K.

Appendix-4

(i) Frequency domain filter in FFT calculations

A data signal normally has a mixture of different frequency components in it. The frequency contents of the signal and their powers can be obtained through operations such as the Fast Fourier Transform (FFT). A low-pass filter passes relatively low frequency components in the signal but stops the high frequency components. The so-called cutoff frequency divides the pass band and the stop band. In other words, the frequency components higher than the cutoff frequency will be stopped by a low-pass filter. This type of filter is especially useful since the random errors involved in the raw position data obtained through reconstruction are characterized by relatively high frequency contents.

The effect of FFT on the signal without noise and with noise is shown in the following block diagrams.

Frequency domain filter to utilize the Fast Fourier Transform (FFT)

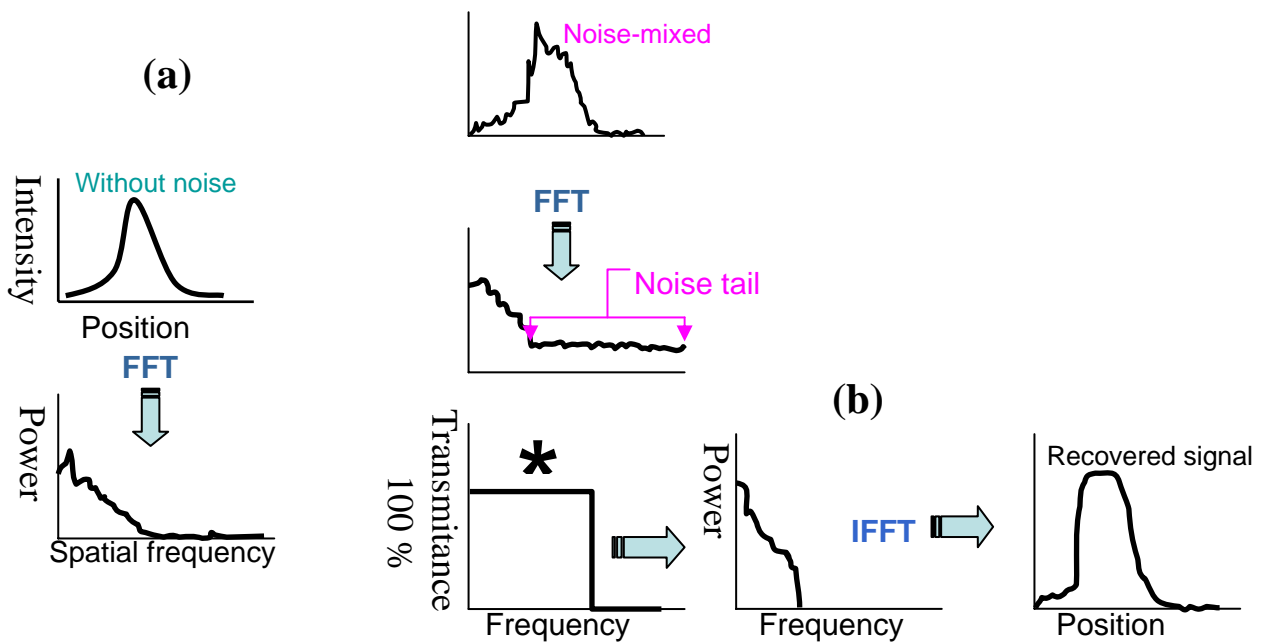


Figure 4

Panel (a) signal without noise and FFT is applied in it. Panel (b) noise-mixed signal and using frequency domain filter to recover the original signal.

(ii) Convolution Theorem

Let f and g be two functions with convolution $f * g$. (Here the asterisk denotes convolution in this context, and not multiplication. The symbol \otimes is sometimes used instead.) Let F denote the Fourier transform operator, so $F[f]$ and $F[g]$ are the Fourier transform of f and g , respectively. Then

$$F[f * g] = \sqrt{2\pi} (F[f]) \cdot (F[g]) \text{ ----- (4a)}$$

Where \cdot denotes point-wise multiplication. The Fourier transform of the convolution of two functions is equal to the product of their individual Fourier transforms. It also works the other way around:

$$F[f \cdot g] = \frac{F[f] * F[g]}{\sqrt{2\pi}} \text{ ----- (4b)}$$

By applying the inverse Fourier transform F^{-1} , we can write:

$$f * g = \sqrt{2\pi} F^{-1}[F[f] \cdot F[g]] \text{ ----- (4c)}$$

The theorem says that the convolution of two functions is equal to the inverse Fourier transform of the product of their individual Fourier transforms.

The formulation of equation (4c) is especially useful for implementing a numerical convolution on a computer: The standard convolution algorithm has quadratic computational complexity. With the help of the convolution theorem and the fast Fourier transform, the complexity of the convolution can be reduced to $O(n \log n)$. This can be exploited to construct fast multiplication algorithms.

Appendix-5

(a) Developed program codes to simulate the images

(i) Rare gas image simulation

```

from pylab import *
from numarray import *
import random as rnd
#physical constants (universal)
KB=1.38e-23 #Boltzmann const.
NAK=6.02e26 #Avogadro const. in kg
EC=1.602e-19 #Elementary charge
#function definitions
# random number generator following Sine function
# v1: angle in radian
def mtRndSin(v1):
    delta=pi*0.1
    v2=v1+delta*(2*rnd.random()-1.0)
    f1=sin(v1)
    f2=sin(v2)
    if (f2/f1) >= rnd.random():
        f1=f2
        v1=v2
    return v1
# random number generator following 1-beta*P2(cos q) distribution
# v1: angle in radian
# beta: anisotropy parameter
def mtRndAP(v1, beta):
    delta=pi*0.3
    f1=1+beta*(1.5*cos(v1)**2 - 0.5)
    v2=v1+delta*(2*rnd.random()-1.0)
    if v2<0 or v2>pi:
        f2=0
    else:
        f2=1+beta*(1.5*cos(v2)**2 - 0.5)
    if 0 < v1 < pi and f1 != 0:
        if (f2/f1) >= rnd.random():

```

```

        f1=f2
        v1=v2
    return v1
# random number generator following Maxwell-Boltzmann distribution
#v1: last value
#t: temperature / K
#mw: molecular weight / au
def mtRndMB(v1, t, mw):
    delta=1000.0
    m=mw/NAK;
    v2=v1+delta*(2*rnd.random()-1.0)
    f1= v1**2 * exp((-0.5*m*v1**2)/(KB*t))
    if v2 > 0:
        f2= v2**2 * exp((-0.5*m*v2**2)/(KB*t))
    else:
        f2=0.0
    if (f2/f1) >= rnd.random():
        f1=f2
        v1=v2
    return v1
def RndMB(t, mw):
    r1=rnd.random()
    r2=rnd.random()
    return sqrt(-2.0*KB*t/mw*log(r1))*cos(2.0*pi*r2)
# random number generator following Gaussian distribution
#x0: center
#w: width
def mtRndGaus(v1, x0, w):
    #old: delta=0.1
    delta=0.001
    v2=v1+delta*(2*rnd.random()-1.0)
    f1=exp(-2*((v1-x0)/w)**2)
    f2=exp(-2*((v2-x0)/w)**2)
    if (f2/f1) >= rnd.random():
        f1=f2
        v1=v2
    return v1
#writing binary image data 256*256
#16 bit unsigned little endian

```



```

#input data MUST be set to UInt16
def wrtBinImg(name, c):
    f=open(name, 'wb')
    for i in range(256):
        for j in range(256):
            a=c[i,j] & 255 #lower 8 bit
            b=c[i,j] >> 8 #higher 8 bit
            if 0 <= a <= 255 and 0 <= b <= 255:
                f.write(chr(a))
                f.write(chr(b))
            else:
                print 'out of range'
                f.write(chr(0))
                f.write(chr(0))
        f.close()
#main program
#experimental conditions
ISZ=256 #Number of pixels in the PSD
SP=0.112e-3 #Pixel size / m
rMCP=12.5e-3 #radius of MCP in m
TOF=2.034e-6 #flight time
beta=0.0 #anisotropy parameter
# x, y, z: position of fragment
# vx, vy, vz: velocity componens of fragment
# r, v: radius and velocity
# q, f: angles of ejection
# PSD is parallel to xy plane
#preparation of PSD
img=zeros((ISZ,ISZ)) #Int type in default
#initialization of lastValues for rnd generators
#lvMB=200
lvMB=1000 # modified value: see program "ckmtmb.py" in folder
Simu_Rare_Paper_Write-2008
lvS1=pi/2
lvE1=0.1
lvAP=pi/2+0.01
lvDx=0.0
lvDy=0.0
#initialization of number of ions in / out of PSD

```

```

inMCP=0
inPSD=0
outPSD=0
zeroPxPy=0
filename='He--x17y32'
#fck=open('mbck1000.dat', 'w')
# Main iteration loop
for m in range(10):
    print 'calculation in progress... ', m+1
    for n in range(10000):
        #x=mtRndGaus(lvDx, 0.0, 1.7e-3)
        #lvDx=x
        #y=mtRndGaus(lvDy, 0.0, 3.2e-3)
        #lvDy=y
        x=0.0
        y=0.0
        z=0.0
        #motion of parent molecules
        #thermal velocity
        v=mtRndMB(lvMB, 300, 4.0)
        lvMB=v
        #fck.write('%d %e\n'%(n, v))
        #ejection angles
        q=mtRndSin(lvS1)
        lvS1=q
        f=2*pi*rnd.random()
        #velocity components
        vx=v*sin(q)*cos(f)
        vy=v*sin(q)*sin(f)
        vz=v*cos(q)
        #expansion
        x=x+vx*TOF
        y=y+vy*TOF
        z=z+vz*TOF
        #positions on the PSD
        px=int(x/SP + ISZ/2.0 + 0.5)
        py=int(y/SP + ISZ/2.0 + 0.5)
        try:
            r=sqrt( x**2 + y**2 )

```

```

except ValueError:
    r=0
if px==0 or py==0:
    zeroPxPy=zeroPxPy+1
#projection on the PSD
if 0 < px < (ISZ-1) and 0 < py < (ISZ-1):
    if r < rMCP:
        inMCP=inMCP+1
        img[px,py]=img[px,py]+1
    else:
        inPSD=inPSD+1
else:
    outPSD=outPSD+1
total=inMCP + inPSD + outPSD
print 'inMCP:%d, inPSD:%d, outPSD:%d, total:%d\n'%(inMCP, inPSD, outPSD,
total)
#fck.close()
#making X projection
px=zeros((ISZ), Float64)
for i in range(ISZ):
    for j in range(ISZ):
        px[i]+=img[i,j]
apx=px.sum()
pxn=px/apx
#making Y projection
py=zeros((ISZ), Float64)
for i in range(ISZ):
    for j in range(ISZ):
        py[i]+=img[j,i]
apy=py.sum()
pyn=py/apy
#making radial distribution
rd=zeros((ISZ), Float64) #radial distribution
pn=zeros((ISZ), Float64) #number of pixels counted at r
rdn=zeros((ISZ), Float64) #normalized intensity
cX=ISZ/2.0+0.5
cY=ISZ/2.0+0.5
rmax=0
for i in range(0, 256):

```

```

for j in range(0, 256):
    r=int(sqrt((i-cX)**2 + (j-cY)**2))
    if r>rmax:
        rmax=r
    rd[r]+=img[j,i]
    pn[r]+=1
for i in range(rmax+1):
    if pn[i] != 0:
        rd[i]/=pn[i]
    else:
        rd[i]=0
ard=rd.sum()
rdn=rd/ard
imshow(img)
show()
wrtBinImg(filename + '.mca', img)
#writing image data file
fimg=open(filename + '_img.txt', 'w')
for i in range(0,ISZ):
    for j in range(0,ISZ):
        fimg.write('%d'%(img[j,i]))
        fimg.write('\n')
fimg.close()
#writing 1D data file
fld=open(filename + '.1dd', 'w')
fld.write('i px pxn py pyn rd rdn\n')
for i in range(ISZ):
    fld.write('%d %e %e %e %e %e %e\n'%(i, px[i], pxn[i], py[i],
pyn[i], rd[i], rdn[i]))
fld.close()

```

(ii) Photodissociation of fullerene, C₆₀ with thermal parent beam

```

from numpy import *
import random as rnd
from time import clock
#physical constants (universal)
KB=1.38e-23 #Boltzmann const.
NAK=6.02e26 #Avogadro const. in kg

```

```

EC=1.602e-19 #Elementary charge
#function definitions
# Sine random number generator
# using transformation method
# (calculating inverse of integral of sin)
# with lower and upper bounds
def RndSin(lb,ub):
    tLb=-cos(lb)+1
    tUb=-cos(ub)+1

    ur= (tUb-tLb)*rnd.random() + tLb
    return arccos(1-ur)
# Maxwell-Boltzmann random number generator
def RndMB(t, mw):
    r1=rnd.random()
    r2=rnd.random()
    r3=rnd.random()
    r4=rnd.random()
    r5=rnd.random()
    r6=rnd.random()
    vx = sqrt(-2.0*KB*t/(mw/NAK)*log(r1))*cos(2.0*pi*r2)
    vy = sqrt(-2.0*KB*t/(mw/NAK)*log(r3))*cos(2.0*pi*r4)
    vz = sqrt(-2.0*KB*t/(mw/NAK)*log(r5))*cos(2.0*pi*r6)
    return sqrt( vx**2 + vy**2 + vz**2 )
#writing binary image data 256*256
#16 bit unsigned little endian
#input data MUST be set to UInt16
def wrtBinImg(name, c):
    f=open(name, 'wb')
    for i in range(256):
        for j in range(256):
            a=c[i,j] & 255 #lower 8 bit
            b=c[i,j] >> 8 #higher 8 bit
            if 0 <= a <= 255 and 0 <= b <= 255:
                f.write(chr(a))
                f.write(chr(b))
            else:
                print 'out of range'
                f.write(chr(0))

```

```
f.write(chr(0))

f.close()

# random number generator following Gaussian distribution
#x0: center
#w: width
def mtRndGaus(v1, x0, w):
    if w==0.0:
        return 0.0
    else:
        delta=w/2.0 # width dependent delta
        v2=v1+delta*(2*rnd.random()-1.0)
        f1=exp(-2*((v1-x0)/w)**2)
        f2=exp(-2*((v2-x0)/w)**2)

        if (f2/f1) >= rnd.random():
            f1=f2
            v1=v2
        return v1

#main program
# size2.py Input Parameter Section
#experimental conditions
ISZ=256 #Number of pixels in the PSD
SP=0.156e-3 # Pixel size / m > previous value: SP=0.1e-3
rMCP=25.0e-3 #radius of MCP in m

swDF='OFF' # switch of defocusing with Gaussian > Previously ON
dfX=0.2e-3 # sample beam path
dfY=2.8e-3 # SR path
mP=720 #mass of the molecule in the beam
swBT='ON' # switch to convolute beam temperature
tP=785 #beam temperature in K
# limit of elevation angle
bL=0
bU=7*(pi/180.0)
TOF=50e-6 #flight time
sw='C2' #switch to change dissociation mechanism
nSec=80 #accumulation time > setting value:
nCps=10000 #counts per second
#filename='an0810d6' #output binary/text image data file name
```

```

filename='C2'# Initially used file name: sim4
psdShiftX=64 # PSD shift in vertical
# You may need to adjust parameters out of this Input Parameter Section
# end of Input Parameter Section
# variables in the Main program
# x, y, z: position of fragment
# vx, vy, vz: velocity componens of fragment
# r, v: radius and velocity
# q, f: angles of ejection
# PSD is parallel to xy plane
# Electric field vector of the light is parallel to the TOF axis (z)
#preparation of PSD
img=zeros((ISZ,ISZ), UInt16) #Int type in default
#initialization of number of ions in / out of PSD
inMCP=0
inPSD=0
outPSD=0
zeroPxPy=0
lvAP1=pi/4
lvAP2=pi/4
lvDx=0.0
lvDy=0.0
# main iteration loop
t0=clock()
for m in range(nSec):
    print 'calculation in progress... acc. ', m+1, ' sec.'
    for n in range(nCps):
        #initial position (defocusing size)
        if swDF=='ON':
            x=mtRndGaus(lvDx, 0.0, dfX)
            lvDx=x
            y=mtRndGaus(lvDy, 0.0, dfY)
            lvDy=y
            z=0.0
        else:
            x=0.0
            y=0.0
            z=0.0
    #motion of parent molecules

```

```

#thermal velocity
if swBT=='ON':
    v=RndMB(tP, mP)
    lvMB=v
    #ejection angles
    q=RndSin(bL, bU)
    f=2*pi*rnd.random()
    #velocity components
    #for fullerene beam simulation
    vx=v*cos(q)
    vy=v*sin(q)*sin(f)
    vz=v*sin(q)*cos(f)
else:
    vx=0
    vy=0
    vz=0
#C2 loss
if sw=='C2':
    # first step
    v=sqrt(2.0*(0.4*EC)/(720.0/NAK)*(2.0/58.0));
    #ejection angles
    q=RndSin(0,pi)
    lvAP1=q
    f=2*pi*rnd.random()

    #velocity components
    vx=vx+v*sin(q)*cos(f)
    vy=vy+v*sin(q)*sin(f)
    vz=vz+v*cos(q)
    # second step
    v=sqrt(2.0*(0.4*EC)/(696.0/NAK)*(2.0/56.0));
    #ejection angles
    q=RndSin(0,pi)
    lvAP2=q
    f=2*pi*rnd.random()
    #velocity components
    vx=vx+v*sin(q)*cos(f)
    vy=vy+v*sin(q)*sin(f)
    vz=vz+v*cos(q)

```



```

#C4 loss
elif sw=='C4':
    v=sqrt(2.0*(0.4*EC)/(720.0/NAK)*(4.0/56.0));
    #ejection angles
    q=RndSin(0,pi)
    lvAP2=q
    f=2*pi*rnd.random()
    #velocity components
    vx=vx+v*sin(q)*cos(f)
    vy=vy+v*sin(q)*sin(f)
    vz=vz+v*cos(q)
    #expansion during TOF
    x=x+vx*TOF
    y=y+vy*TOF
    z=z+vz*TOF
    #calculating positions on the PSD
    px=int(x/SP + ISZ/2.0 + 0.5 - psdShiftX)
    py=int(y/SP + ISZ/2.0 + 0.5)
    try:
        r=sqrt( x**2 + y**2 )
    except ValueError:
        r=0
    if px==0 or py==0:
        zeroPxPy=zeroPxPy+1
    #accumulating projection on the PSD
    if 0 < px < (ISZ-1) and 0 < py < (ISZ-1):
        if r < rMCP:
            inMCP=inMCP+1
            img[px,py]=img[px,py]+1
        else:
            inPSD=inPSD+1
    else:
        outPSD=outPSD+1
total=inMCP + inPSD + outPSD
print 'inMCP:%d, inPSD:%d, outPSD:%d, total:%d counts\n'%(inMCP, inPSD,
outPSD, total)
print 'time = ', clock()-t0
#writing text image data file
fimg=open(filename + '_img.txt', 'w')

```

```

for i in range(0,ISZ):
    for j in range(0,ISZ):
        fimg.write('%d'%(img[j,i]))
    fimg.write('\n')
fimg.close()
#writing binary image data file
wrtBinImg(filename + '.mca', img)
# making projected 1D data
#making X projection
px=zeros((ISZ), Float64)
for i in range(ISZ):
    for j in range(ISZ):
        px[i]+=img[i,j]
apx=px.sum()
pxn=px/apx
#making Y projection
py=zeros((ISZ), Float64)
for i in range(ISZ):
    for j in range(ISZ):
        py[i]+=img[j,i]
apy=py.sum()
pyn=py/apy
#making radial distribution
rd=zeros((ISZ), Float64) #radial distribution
pn=zeros((ISZ), Float64) #number of pixels counted at r
rdn=zeros((ISZ), Float64) #normalized intensity
cX=ISZ/2.0+0.5
cY=ISZ/2.0+0.5
rmax=0
for i in range(0, 256):
    for j in range(0, 256):
        r=int(sqrt((i-cX)**2 + (j-cY)**2))
        if r>rmax:
            rmax=r
        rd[r]+=img[j,i]
        pn[r]+=1
for i in range(rmax+1):
    if pn[i] != 0:
        rd[i]/=pn[i]

```

```

        else:
            rd[i]=0
ard=rd.sum()
rdn=rd/ard
#writing 1D data file
fld=open(filename + '.1dd', 'w')
fld.write('i px pxn py pyn rd rdn\n')
for i in range(ISZ):
    fld.write('%d %e %e %e %e %e %e\n'%(i, px[i], pxn[i], py[i],
pyn[i], rd[i], rdn[i]))
fld.close()

```

(b) Developed program tools to analyze experimental and simulated image

(i)

```

import os
dfns=['He-02']
ofnm='a' # for simulated image
for dfn in dfns:
    x=128
    y=128
    ofnm='x'+str(x)+'y'+str(y)
    rslt=os.system('ssimg_arg_one-He.py ' + dfn + '.mca ' + dfn + ofnm
+ '.raw ' + str(x) + ' ' + str(y))
    print rslt
    rslt=os.system('iat_arg ' + dfn + ofnm + '.raw ' + dfn + ofnm +
'.iat')
    print rslt
    rslt=os.system('arrd_arg-one-He.py ' + dfn + ofnm + '.iat ' + dfn
+ ofnm + '.dat')
    print rslt

```

(ii)

```

import sys
from numarray import *
from pylab import grid, arange, plot, subplot, show, imshow, title
# Functions

#reading binary image data 256*256
#16 bit unsigned little endian
def rdBinImg(name, nh, c):

```

```

f=open(name, 'rb')
#header
# a=f.read(nh)
for i in range(0,256):
    for j in range(0,256):
        a=f.read(1)
        b=f.read(1)
        c[i,j] = ord(a) + 256*ord(b)
f.close()
#reading binary image data 256*256
#with TRANSPOSED manner
#16 bit unsigned little endian
def rdBinImgT(name, c):
    f=open(name, 'rb')
    # header
    #a=f.read(814)
    for i in range(0,256):
        for j in range(0,256):
            a=f.read(1)
            b=f.read(1)
            c[j,i] = ord(a) + 256*ord(b)
    f.close()
#writing binary image data 256*256
#16 bit unsigned little endian
#input data MUST be set to UInt16
def wrtBinImg(name, c):
    f=open(name, 'wb')
    for i in range(256):
        for j in range(256):
            a=c[i,j] & 255 #lower 8 bit
            b=c[i,j] >> 8 #higher 8 bit
            if 0 <= a <= 255 and 0 <= b <= 255:
                f.write(chr(a))
                f.write(chr(b))
            else:
                print 'out of range'
                f.write(chr(0))
                f.write(chr(0))
    f.close()

```

```

# Main Program
# ssimg_arg.py Input Parameter Section
#header size in byte
nh=814
#nh=0
#shift values in pixel (origin at upperleft)
xSft= 128 - int(sys.argv[3]) #positive value to come right> character
string to number conversion
ySft= 128 - int(sys.argv[4]) #positive value to come down
print 'x, y =', xSft, ySft
fzs=1 #flag for zero suppression
fzf=0 #flag for zero fill
zo=60 #zerofill radius
fww=0 # flag for Welch windowing
# end of Input Parameter Section
img=zeros((256, 256), UInt16)
imgSft=zeros((256, 256), UInt16)
imgSym=zeros((256, 256), UInt16)
imgtick=zeros((256,256),UInt16)
#reading original image
rdBinImg(sys.argv[1], nh, img)
#rdBinImgT('c196g.mca', img)
subplot(221)
title('Original')
imshow(img)
#shifting the image
for i in range(256):
    for j in range(256):
        if 0 <= i-ySft <= 255 and 0 <= j-xSft <= 255:
            imgSft[i,j]=img[i-ySft, j-xSft]
        else:
            imgSft[i,j]=0
for i in range(256):
    imgtick[i,127]=50
    imgtick[127,i]=50
imgtick+=imgSft
subplot(222)
title('Shifted')
imshow(imgtick)

```

```

#symmetrizing the shifted image
for i in range(256):
    for j in range(128):
        imgSym[i,j]=(imgSft[i,j]+imgSft[i,255-j])/2.0
        imgSym[i,255-j]=(imgSft[i,j]+imgSft[i,255-j])/2.0
subplot(223)
title('Symmetrized')
imshow(imgSym)
#zero suppression (negative value to zero)
if fzs:
    for i in range(256):
        for j in range(256):
            if imgSym[i,j] < 0:
                imgSym[i,j] =0.0
#zero filling
if fzf:
    for i in range(256):
        for j in range(256):
            r=sqrt((i-127.5)**2 + (j-127.5)**2)
            if r > zo:
                imgSym[i,j]=0.0
#Welch window
if fww:
    for i in range(256):
        for j in range(256):
            r=sqrt((i-127.5)**2 + (j-127.5)**2)
            ww=1-(r/128.5)**2
            imgSym[i,j]*=ww
wrtBinImg(sys.argv[2], imgSym)
subplot(224)
title('Output')
imshow(imgSym)
show()

(iii)
import sys
from numarray import *
from pylab import plot, axis, show, subplot, imshow, title
# Functions

```

```

#reading binary data
#16 bit unsigned little endian
def rdBinImg(name, c):
    f=open(name, 'rb')
    #header
    #a=f.read(814)
    for i in range(0,256):
        for j in range(0,256):
            a=f.read(1)
            b=f.read(1)
            c[i,j] = ord(a) + 256*ord(b)
    f.close()
# Main Program
# rdsn_arg.py Input Parameter Section
#center of distribution:
#e. g. focusing center of rare gases
cX=128.0
cY=128.0
#cX=127.5  previous values: Adjust the center, cX and cY
#cY=127.5
#TOF in sec
#He+:
tof=2.034e-6
# m / pixel
ps=0.112e-3
#angle range (0 - 180 deg)
ab=0  #angle begin
ae=45 #angle end (Initially this value was: ae = 60)
#angle range (180 - 360 deg)
alb1=135  #angle begin
ale1=180  #angle end
#centerline noize reduction (plus minus cn in X)
cn=0
# end of Input Parameter Section
#ps=1 #to test
abCos=cos(ab*(pi/180.0))
aeCos=cos(ae*(pi/180.0))
alb1Cos=cos(alb1*(pi/180.0))
ale1Cos=cos(ale1*(pi/180.0))

```

```

#input data file names
data=[sys.argv[1]]
print 'Start !'
ndf=0
for name in data:
    print 'processing image ', name
    img=zeros((256, 256), Float64)
    r1d=zeros((400), Float64)
    r2d=zeros((400), Float64)
    pn=ones((400), Float64) #number of pixels counted at r
    r1dn=zeros((400), Float64) #normalized intensity
    r2dn=zeros((400), Float64) #normalized intensity
    r1ng=zeros((256, 256)) # to indicate the angle range
    r2ng=zeros((256, 256)) # to indicate the angle range
    rdn=zeros((400), Float64) #normalized intensity
    rdBinImg(name, img)
    fr=open(sys.argv[2], 'w')
    rmax=0
    r1max=0
    for i in range(0, 256):
        for j in range(0, 256):
            if not ((127-cn) < i < (127+cn)):
                r1r1=sqrt((i-cX)**2 + (j-cY)**2)
                try:
                    aCos=-(j-cX)/r1r1
                except ZeroDivisionError:
                    aCos=0
                if aeCos <= aCos <= abCos:
                    r1=int(r1r1)
                    if r1>r1max:
                        r1max=r1
                    r1d[r1]+=img[j,i]*abs(i-cX)
                    pn[r1]+=1
                    r1ng[j,i]=1
    ard1=r1d.sum()
    r2max=0
    for i in range(0, 256):
        for j in range(0, 256):
            if not ((127-cn) < i < (127+cn)):

```



```

r2r2=sqrt((i-cX)**2 + (j-cY)**2)
try:
    a1Cos=-(j-cX)/r2r2
except ZeroDivisionError:
    a1Cos=0
if a1e1Cos <= a1Cos <= a1b1Cos:
    r2=int(r2r2)
    if r2>r2max:
        r2max=r2
    r2d[r2]+=img[j,i]*abs(i-cX)
    pn[r2]+=1
    r2ng[j,i]=1

ard2=r2d.sum()
ard = ardl + ard2
rdn = (r1d + r2d)/ard
#print ' rdn = ', rdn
for i in range(0,400):
    fr.write('%d %f %f %f %f\n'%(i, i*ps/tof, r1d[i], r2d[i],
rdn[i]))
fr.close()
ndf+=1
subplot(2,2,1)
title('Input image')
imshow(img)
subplot(2,2,2)
title('Integ. region-1')
imshow(r1ng)
subplot(2,2,3)
title('Integ. region-2')
imshow(r2ng)
subplot(2,2,4)
title('Radial dist.')
plot(rdn)
del img, r1d, r2d, rdn, r1ng, r2ng
print 'Done ! %d files.'%(ndf)
show()

```

“List of Publications”

Journal articles:

1. “Velocity map imaging apparatus applicable to a study of multiple photofragmentation of C_{60} ”, **Md. Serajul Islam Prodhhan**, Hideki Katayanagi, Chaoqun Huang, Hajime Yagi, Bhim Prasad Kafle, Koichiro Mitsuke, Chem. Phys. Lett., 469 (2009) 19-25.
2. “Absolute Total Photoionization Cross Section of C_{60} in the range of 25 to 120 eV”, Bhim. P. KAFLE, Hideki KATAYANAGI, **Md. Serajul. I. PRODHAN**, Hajime YAGI, Chaoqun HUANG, and Koichiro. MITSUKE, J. Phys. Soc. Jpn. 77(1) (2008) 014302
3. “Photoabsorption cross section of C_{60} thin films from the visible to vacuum ultraviolet”, H. Yagi, K. Nakajima, K. R. Koswattage, K. Nakagawa, C. Huang, **Md. S. I. Prodhhan**, B. P. Kafle, H. Katayanagi and K. Mitsuke, CARBON, 47 (2009) 1152-1157.
4. “Relative Partial Cross Sections for Single, Double, and Triple Photoionization of C_{60} and C_{70} ”, K. Mitsuke, H. Katayanagi, B. P. Kafle, C. Huang, H. Yagi, **Md. S. I. Prodhhan**, and Y. Kubozono, J. Phys. Chem. A, 111 (2007) 8336.
5. “Velocity map imaging of C_{60} molecular beams”, Hideki Katayanagi, Chaoqun Huang, Hajime Yagi, Bhim P. Kafle, **Md. Serajul I. Prodhhan**, Koichi Nakajima, and Koichiro Mitsuke, Rev. Sci. Instrum. (Submitted, 2008).

Other articles:

- (i) “Momentum Imaging of the Photofragments from C_{60} and Data Analysis of the Image”, **Md. Serajul Islam PRODHAN**, Hideki KATAYANAGI, Bhim Prasad KAFLE, Chaoqun HUANG, Hajime YAGI, Koichiro MITSUKE, The UVSOR Activity Report – 2008, Okazaki, Japan, June, 2008.

(ii) “Scattering Distributions of the Photofragments from C_{60} in the Extreme Ultraviolet”, PRODHAN Md. Serajul Islam; KAFLE, Bhim Prashad; YAGI, Hajime; KATAYANAGI, Hideki; MITSUKE, Koichiro, Annual Review-2006, Pg. no: 112-113, Institute for Molecular Science (IMS), Okazaki, Japan. 2006, (Sept. 2005~Aug. 2006).

(iii) “Construction of a Velocity Map Imaging Spectrometer and Its Performance Test Using Rare Gases”; Md. S. I. Prodhhan, H. Katayanagi, C. Huang, H. Yagi, B. P. Kafle, K. Nakajima, K. Mitsuke; The UVSOR Activity Report – 2009, Okazaki, Japan (submitted).

“List of Conference/ Symposium/Workshop”

International conference:

1. Md. Serajul Islam PRODHAN; Hideki KATAYANAGI; Bhim Prashad KAFLE, Chaogun HUANG; Hajime YAGI; Koichiro MITSUKE, “Momentum imaging of the photofragments from C₆₀ and data analysis of the image”, The Winter School of Sokendai / Asian CORE Program; Frontiers of Materials, Photo-, and Theoretical Molecular Sciences, Pg. no: P42, Okazaki, Conference Center, Japan. January 24-26, 2008.
2. PRODHAN, Md. Serajul Islam; KAFLE, Bhim Prashad; Huang Chaogun; YAGI, Hajime; KATAYANAGI, Hideki; MITSUKE, Koichiro; “Photofragmentation of C₆₀ in the Extreme Ultraviolet”, The 1st Winter School of JSPS ASIA CORE Program in Beijing-Frontiers of Materials, Photo-, and Theoretical Molecular Sciences, Pg. no: 30, Institute of Chemistry, Chinese Academy of Sciences (ICCAS, China), Beijing, China. Dec. 5-9, 2006.

Domestic conference:

1. **Md. Serajul Islam PRODHAN**, Hideki KATAYANAGI, Chaoqun HUANG, Hajime YAGI, Koichiro MITSUKE “Momentum Imaging Spectroscopy of Rare Gases and Fullerenes by using Synchrotron Radiation” Annual Meeting of Japan Society for Molecular Science conference, CD No: 3P067, International Conf. Center, Fukuoda, Hakata, Japan. Sept 24-27, 2008.
2. Md. S. I. PRODHAN, H. KATAYANAGI, C. HUANG, H. YAGI, K. MITSUKE, “Influence of the Initial Beam Temperature on the Scattering Distribution of the Photofragments from Fullerene Ions”, 24th Symposium on Chemical Kinetics and Dynamics (SCKD)”, Hokaido Univ, Sapporo, Japan, June 2-4, 2008.

3. PRODHAN Md. Serajul Islam; Hideki KATAYANAGI; KAFLE, Bhim Prashad; Chaoqun Huang; Hajime YAGI; Koichiro MITSUKE “Momentum imaging of the photofragments from fullerenes” The 1st SOKENDAI Workshop, Pg. no: Oral 4-4, CD no: Oral 4-4, ISAS (The Institute of Space and Astronautical Science), Sagamihara, Kanagawa, Japan. Nov. 8-9, 2007.
4. PRODHAN, Md. Serajul Islam, Hideki KATAYANAGI; KAFLE, Bhim Prashad; Chaoqun Huang; Hajime YAGI; Koichiro MITSUKE “Momentum imaging of the photofragments from fullererenes”, Molecular Science conference, CD no: 3C17 (Oral), Tohoku Univ., Sendai, Japan. Sept. 17-20, 2007.
5. Md. S. I. Prodhan, B. P. Kafle, C. Huang, H. Yagi, H. Katayanagi, and K. Mitsuke, “New end station developed for momentum imaging spectroscopy of the fragments from fullerenes ions”, 23rd Symposium on Chemical Kinetics and Dynamics. Pg. no: 75, Kobe Univ., Japan, June 13-15, 2007.
6. Prodhan, Md. Serajul Islam, Katayanagi, Hideki, Huang, Chaoqun, Yagi, Hajime, Kafle, Bhim Prasad, Nakajima, Koichi, Mitsike, Koichiro; “Construction of a velocity map imaging spectrometer and image simulations of the fragment ions from C₆₀” 25th Symposium on Chemical Kinetics and Dynamics (SCKD)”, Omiya Sonic City, Omiya, Japan; June 1–3, 2009 (Submitted)